(NASA-CR-180248) SPECTRORADIOMETRIC N87-18911
CALIBRATION OF THE THEMATIC MAPPER AND
MULTISPECTRAL SCANNER SYSTEM Final Report,
1 Nov. 1982 - 30 Apr. 1986 (Arizona Univ., Unclas
Tucson.) 228 p CSCL 14B G3/43 43793

FINAL REPORT

ON

"SPECTRORADIOMETRIC CALIBRATION OF THE THEMATIC MAPPER AND MULTISPECTRAL SCANNER SYSTEM"

Contract Number NAS5-27382

Fore the Period: 1 November 1982 - 30 April 1986

NASA/Goddard Space Flight Center
Greenbelt, Maryland 20771

James M. Palmer, Co-Investigator

Philip N. Slater, Principal Investigator

Optical Sciences Center
University of Arizona
Tucson, Arizona 85721

December 1986

Abstract

This is the final report on NAS5-27382 covering the period November 1982 to April 1986. It is divided into four sections as follows:

The first section provides a list of personnel who have contributed to the program, identifying three students who have received PhD degrees as a result of their work on the program and two who have received MS degrees. Sixteen publications and presentations are also listed.

The second section is a preprint summarizing five in-flight absolute radiometric calibrations, made in the period from July 1984 to November 1985, at White Sands, New Mexico, of the solar reflective bands of the Landsat-5 Thematic Mapper (TM). The 23 band-calibrations made on the five dates show a 2.5% RMS variation from the mean as a percentage of the mean.

The third section is a preprint that discusses the reflectance-based results of section two in considerable detail. It proceeds to analyze and present results of a second, independent calibration method based on radiance measurements from a helicopter.

The fourth section consists of Chapters 3-6 of Carol Kastner's dissertation that discuss radiative transfer through the atmosphere, model atmopsheres, the calibration methodology used at White Sands and the results of a sensitivity analysis of the reflectance-based approach.

SECTION I

INTRODUCTION

I. INTRODUCTION

This is the final report on Contract NAS5-27382 titled "Spectroradiometric Calibration of the Thematic Mapper," covering the period November 1, 1982 to April 30, 1986. It is divided into the following sections:

1. This introduction continues with a list of personnel who have contributed to this program, noting in particular those students who have received higher degrees as a result. This is followed by a list of publications and presentations.
2. The second section is a preprint summarizing five in-flight absolute radiometric calibrations, made in the period of July 1984 to November 1985, at White Sands, New Mexico, of the solar reflective bands of the Landsat-5 Thematic Mapper (TM). The 23 band-calibrations made on the five dates show a 2.5% RMS variation from the mean as a percentage of the mean.
3. The third section is a preprint that discusses the reflectance-based results of section two in considerable detail. It proceeds to analyze and present results of a second, independent calibration method based on radiance measurements from a helicopter.
4. The fourth section consists of Chapters 3-6 of Carol Kastner's dissertation that discuss radiative transfer through the atmosphere, model atmopsheres, the calibration methodology used at White Sands and the results of a sensitivity analysis of the reflectance-based approach.

Personnel

The following have contributed to the program:

Harumi Aoki -- one-year visiting scientist from PENTAX, Japan.

Stuart Biggar -- pursuing PhD

Kenneth Castle -- PhD, 1985 "Absolute radiometric calibration of a spectropolarimeter."

Barbara Capron -- changed dissertation topics.

Nianzeng Che -- two-year visiting scientist from Beijing Institute of Technology, Peoples Republic of China.

Magdeleine Dinguirard -- 18-month visiting scientist from CERT, France.

Elaine Ezra -- Agricultural Research Service, Phoenix (now at EG&G).

Gunnar Fedosejevs -- Canada Centre for Remote Sensing.

Ronald Holm -- PhD, 1986 "The absolute radiometric calibration of space-based sensors."

Carol Kastner -- PhD, 1985 "Absolute radiometric calibration of the Landsat Thematic Mapper."

Ray Jackson -- Agricultural Research Service, Phoenix.

Linda Lingg -- changed dissertation topics.

Yalan Mao -- pursuing PhD.

Susan Moran -- Agricultural Research Service, Phoenix.

James Palmer -- co-principal investigator.

Amy Phillips -- MS, 1985, "Absolute calibration of, and atmospheric measurements, using a multiband radiometer."

Philip Slater -- principal investigator.

Phillip Teillet -- Canada Centre for Remote Sensing.

Sandra Witman -- MS, 1986 "Radiometric calibration of the Thematic Mapper 48-inch diameter spherical integrating source using two different calibration methods.

Benfan Yuan -- 15-month visiting scientist from the Institute of Spacecraft System Engineering, Peoples Republic of China.

In addition we have been greatly helped at White Sands by D. Ferralez, D. Ream and R. K. Savage of the Atmospheric Sciences Laboratory at White Sands Missile Range.

Publications

The following publications and presentations were supported by this contract:

C. J. Kastner and P. N. Slater, "In-flight radiometric calibration of advanced remote sensing systems," presented at the Society of Photo-optical Instrumentation Engineers Meeting, Conference 356, San Diego, California, 1982.

K. R. Castle, M. Dinguirard, C. E. Ezra, R. G. Holm, R. D. Jackson, C. J. Kastner, J. M. Palmer, R. Savage, and P. N. Slater, "In-progress absolute radiometric inflight calibration of the Landsat-4 sensors," Post-symposium proceedings presented at the NASA Goddard Landsat-4 Early Results Symposium, February 22-24, 1983.

K. R. Castle, C. E. Dinguirard, C. E. Ezra, R. G. Holm, R. D. Jackson, C. J. Kastner, J. M. Palmer, R. Savage, and P. N. Slater, "Preliminary results for the in-flight absolute calibration of the thematic mapper," invited paper at the Society of Photo-Optical Instrumentation Engineers meeting on Techniques for Extraction of Information from Remotely Sensed Images, SPIE meeting, Rochester, NY, August, 1983.

P. N. Slater, "A review of radiometric calibration problems," invited paper at the International Colloquium on Spectral Signatures of Objects in Remote Sensing, Bordeaux, France, September 1983.

K. R. Castle, R. G. Holm, C. J. Kastner, J. M. Palmer, P. N. Slater, M. Dinguirard, C. E. Ezra, R. D. Jackson, and R. K. Savage, "In-flight absolute calibration of the Thematic Mapper," IEEE Geosciences and Remote Sensing special issue on Landsat-4, V. V. Salomonson, ed., pp. 251-257, May 1984.

J. M. Palmer, "Effective bandwidths for Landsat-4 and Landsat-D' Multispectral Scanner and Thematic Mapper Subsystems," IEEE Geosciences and Remote Sensing special issue on Landsat-4, V. V. Salomonson, ed., pp. 336-338, May 1984.

P. N. Slater, "Importance and attainment of accurate absolute radiometric calibration," Proc. SPIE 475, pp. 34-40, 1984.

N-Z Che, R. D. Jackson, A. L. Phillips, and P. N. Slater, "Field radiometer methods for reflectance and atmospheric measurements," Proc. SPIE 499, pp. 24-33, 1984.

P. N. Slater, "Absolute radiometric calibration of space remote sensing systems," invited paper at the Optical Society of America meeting in San Diego, California, November, 1984.

P. N. Slater, "Survey of multispectral imaging systems for earth observations," Remote Sensing of the Environment, 17:85-102, 1985.

P. N. Slater, "Radiometric considerations in remote sensing," invited paper in the Proceedings of the IEEE Vol. 73, No. 6, pp. 997-1011, 1985.

S. F. Biggar, C. J. Bruegge, B. A. Capron, K. R. Castle, M. C. Dinguirard, R. G. Holm, R. D. Jackson, L. J. Lingg, Y. Mao, M. S. Moran, J. M. Palmer, A. L. Phillips, R. K. Savage, P. N. Slater, S. L. Witman and B. Yuan, "Absolute calibration of remote sensing instruments," invited paper at the International Society for Photogrammetry and Remote Sensing, Third International Colloquium on Spectral Signatures of Objects in Remote Sensing, Les Arcs, France, December 1985, ESA SP-247, pp. 309-314.

P. N. Slater, "Variations in in-flight absolute radiometric calibration," invited paper at the ISLSCP Conference in Rome, Italy, December 1985, ESA SP-248, May 1986, pp. 357-363.

Ray D. Jackson and Philip N. Slater, "Absolute calibration of field reflectance radiometers," Photogrammetric Engineering and Remote Sensing, Vol 52, No. 2, February 1986, pp 189-196.

P. N. Slater, S. F. Biggar, R. G. Holm, R. D. Jackson, Y. Mao, M. S. Moran, J. M. Palmer and B. Yuan, "Absolute radiometric calibration of the Thematic Mapper," Proc. SPIE 660, 1986.

P. N. Slater, S. F. Biggar, R. G. Holm, R. D. Jackson, Y. Mao, M. S. Moran, J. M. Palmer and B. Yuan, "Reflectance- and radiance- based methods for the in-flight absolute calibration of multispectral sensors," accepted for publication Rem. Sens. of Environ., 1987.

SECTION II

SUMMARY OF CALIBRATION RESULTS

Absolute Radiometric Calibration of the Thematic Mapper

P. N. Slater, S. F. Biggar, R. G. Holm, R. D. Jackson†, Y. Mao,
M. S. Moran†, J. M. Palmer, and B. Yuan

Optical Sciences Center, University of Arizona, Tucson, Arizona 85721; the authors whose names are marked with a † are with the U. S. Department of Agriculture, Agricultural Research Service, U. S. Water Conservation Laboratory, Phoenix, Arizona 85040.

Abstract

The results are presented of five in-flight absolute radiometric calibrations, made in the period July 1984 to November 1985, at White Sands, New Mexico, of the solar reflective bands of the Landsat-5 Thematic Mapper (TM). The 23 band-calibrations made on the five dates show a ± 2.8% RMS variation from the mean as a percentage of the mean.

Introduction

On July 8, and October 28, 1984 and on May 24, August 28, and November 16, 1985, ground reflectance and atmospheric data were collected at White Sands, New Mexico at the time of TM image acquisitions of the White Sands area. These data were used in a radiative transfer code[1] to predict the spectral radiance at the entrance pupil of the TM. The site of known spectral reflectance was located on unprocessed TM digital images that had not been radiometrically corrected. The site had 16 pixels in the in-track direction and 4 pixels in the across-track direction (1 pixel = 30 x 30 m). The average number of digital counts in each TM band was determined for the site. The calibration of each of the TM solar reflective bands was then calculated in terms of the average digital counts per unit spectral radiance for each band.

These results constitute the body of this brief communication. Further details and discussion of the results have been provided in a special issue of Remote Sensing of Environment[2] devoted to in-flight satellite radiometric calibration. A detailed account of the calibration of the SPOT-1 HRVs, which used the same methodology as employed here for TM, can be found elsewhere[3] in these proceedings.

Results

The results of the five calibrations at White Sands are listed in Tables 1-5. For comparison purposes data for a hypothetical Rayleigh atmosphere and no atmosphere are included at the bottoms of the tables.

Symbols and abbreviations are defined in the tables, with the exception of:

E_O	-	exo-atmospheric spectral irradiance on a surface perpendicular to the sun's rays and at a distance of one astronomical unit (AU).
L	-	radiance (in all cases spectral).
IC	-	internal calibrator on the TM.
Pre	-	pre-flight calibration.
Code	-	spectral radiance values derived from the radiative transfer code.

Table 1. CALIBRATION OF THE THEMATIC MAPPER AT WHITE SANDS ON JULY 8, 1984.

Solar zenith angle Z: 29.2158
Solar distance in AU: 1.0167
Junge size distribution: 2.65
Aerosol size range: 0.02 to 5.02 um
Refractive index: 1.54 - 0.01i
Time of sensor overpass:10:07.5 MST
Calculated visibility: 200 km

Latitude: 32 deg 55 min
Longitude: 106 deg 22 min
Elevation: 1196 m
Pressure: 662 mm (883 mbar)
Temperature: 31.3 deg C
Relative humidity:36%
Nadir viewing angle: 5 deg.

Thematic Mapper bands	1	2	3	4
Central wavelength um	0.4863	0.5706	0.6607	0.8382
Tau Mie	0.0864	0.0777	0.0706	0.0605
Tau Rayleigh	0.1421	0.0735	0.0406	0.0156
Tau ozone	0.0055	0.0232	0.0114	0.0013
Tau water vapor	0.0000	0.0000	0.0000	0.0568
Tau carbon dioxide	0.0000	0.0000	0.0000	0.0000
Spectral reflectance	0.4944	0.5613	0.6051	0.6423
Eo across band in W/m2.um	1955.5	1826.9	1545.0	1042.8
Average image digital counts	>255.00	192.62	234.00	189.18
Preflight cal gains	15.553	7.860	10.203	10.821
Preflight cal offsets	1.8331	1.6896	1.8850	2.2373
IC cal gains for July 8, 84	14.36	7.293	9.638	10.537
IC cal offsets for July 8, 84	2.2790	2.2530	2.3450	2.4590
Normalized code radiance	0.1357	0.1469	0.1623	0.1548
Code TM L in W/m2.sr.um		259.59	242.61	156.17
Spectral L from preflight cal		242.91	227.50	172.76
Spectral L from IC cal		261.03	240.36	177.21
% (Code-Pre)/Pre		6.9	6.6	-9.6
% (Code-IC)/IC		-0.5	0.9	-11.9
Counts per unit radiance		0.742	0.964	1.211

****

CASE FOR RAYLEIGH ATMOSPHERE

Normalized code radiance	0.1400	0.1569	0.1684	0.1782
Code TM L in W/m2.sr.um	264.80	277.30	251.69	179.76
Counts per unit radiance		0.695	0.930	1.052

****

CASE FOR NO ATMOSPHERE

Normalized radiance	0.1374	0.1559	0.1681	0.1784
TM L in W/m2.sr.um	259.84	275.60	251.26	180.02
Counts per unit radiance		0.699	0.931	1.051

****

Table 2. CALIBRATION OF THE THEMATIC MAPPER AT WHITE SANDS ON OCTOBER 28, 1984.

Solar zenith angle Z: 52.068
Solar distance in AU: 0.9932
Junge size distribution: 4.09
Aerosol size range: 0.02 to 5.02 um
Refractive index: 1.54 - 0.01i
Time of overpass: 10:09.1 MST
Calculated visibility: 120 km

Latitude: 32 deg 55 min
Longitude: 106 deg 22 min
Elevation: 1196 m
Pressure: 663.7 mm of Hg
Temperature: 12.4 deg C
Relative humidity: 75%
Nadir viewing angle: 5 deg.

Thematic Mapper bands	1	2	3	4	5	7
Central wavelength um	0.4863	0.5706	0.6607	0.8382	1.6770	2.2230
Tau Mie	0.1360	0.1027	0.0750	0.0401	0.0028	0.0007
Tau Rayleigh	0.1420	0.0739	0.0407	0.0156	0.0010	0.0003
Tau ozone	0.0047	0.0198	0.0098	0.0011	0.0000	0.0000
Tau water vapor	0.0000	0.0000	0.0000	0.0454	0.1241	0.0805
Tau carbon dioxide	0.0000	0.0000	0.0000	0.0000	0.0094	0.0035
Spectral reflectance	0.4380	0.5006	0.5407	0.5850	0.3592	0.1261
Eo across band in W/m2.um	1955.5	1826.9	1545.0	1042.8	220.19	74.78
Average image digital counts	222.69	117.19	140.38	119.69	102.50	26.44
Preflight cal gains	15.553	7.860	10.203	10.821	78.751	147.719
Preflight cal offsets	1.8331	1.6896	1.8850	2.2373	3.2905	3.2117
IC cal gains for 28 Oct 84	14.211	7.264	9.551	10.427	76.87	145.004
IC cal offsets for 28 Oct 84	2.2570	2.2160	2.3700	2.3640	3.1400	3.4440
Normalized code radiance	0.0805	0.0870	0.0973	0.0970	0.0491	0.0197
Code TM L in W/m2.sr.um	159.60	161.21	152.32	102.56	10.96	1.49
Spectral L from preflight cal	142.00	146.95	135.74	108.54	12.60	1.57
Spectral L from IC cal	155.11	158.28	144.50	112.52	12.93	1.59
% (Code-Pre)/Pre	12.4	9.7	12.2	-5.5	-13.0	-5.0
% (Code-IC)/IC	2.9	1.9	5.4	-8.9	-15.2	-5.8
Counts per unit radiance	1.395	0.727	0.922	1.167	9.351	17.699

****

CASE FOR RAYLEIGH ATMOSPHERE

Normalized code radiance	0.0870	0.0979	0.1055	0.1141	0.0701	0.0246
Code TM L in W/m2.sr.um	172.45	181.33	165.20	120.59	15.64	1.87
Counts per unit radiance	1.291	0.646	0.850	0.992	6.553	14.173

****

CASE FOR NO ATMOSPHERE

Normalized radiance	0.0857	0.0980	0.1058	0.1145	0.0703	0.0247
TM L in W/m2.sr.um	169.90	181.41	165.71	121.01	15.69	1.87
Counts per unit radiance	1.311	0.646	0.847	0.989	6.533	14.135

****

Table 3. CALIBRATION OF THE THEMATIC MAPPER AT WHITE SANDS ON MAY 24, 1985.

Solar zenith angle Z: 27.81
Solar distance in AU: 1.0127
Junge size distribution nu: 3.39
Aerosol size range: 0.02 to 5.02 um
Refractive index: 1.54 - 0.01i
Time of overpass: 10:09.2 MST
Calculated visibility 130 km

Latitude:.32 deg 55 min
Longitude: 106 deg 22 min
Elevation: 1196 m
Pressure: 661.0 mm
Temperature: 26.7 deg C
Relative humidity: 35%
Nadir viewing angle: 5 deg.

Thematic Mapper bands	1	2	3	4
Central wavelength um	0.4863	0.5706	0.6607	0.8382
Tau Mie	0.1392	0.0959	0.0775	0.0708
Tau Rayleigh	0.1418	0.0734	0.0405	0.0155
Tau ozone	0.0090	0.0380	0.0186	0.0022
Tau water vapor	0.0000	0.0000	0.0000	0.0454
Spectral reflectance	0.4695	0.5345	0.5778	0.6143
Eo across band in W/m2.um	1955.5	1826.9	1545.0	1042.8
Average image digital counts	>255.00	182.53	218.97	181.77
Preflight cal gains	15.553	7.860	10.203	10.821
Preflight cal offsets	1.8331	1.6896	1.8850	2.2373
IC cal gains for 28 Oct 84	14.2110	7.2640	9.5510	10.4270
IC cal offsets for 28 Oct 84	2.2570	2.2160	2.3700	2.3640
Normalized code radiance	0.1285	0.1365	0.1539	0.1535
Code TM L in W/m2.sr.um	244.94	243.21	231.87	156.07
Spectral L from preflight cal		230.08	212.77	165.91
Spectral L from IC cal		248.23	226.78	172.06
% (Code-Pre)/Pre		5.7	9.0	-5.9
% (Code-IC)/IC		-2.0	2.2	-9.3
Counts per unit radiance		0.751	0.944	1.165

****

CASE FOR RAYLEIGH ATMOSPHERE

Normalized code radiance	0.1353	0.1517	0.1631	0.1728
Code TM L in W/m2.sr.um	257.95	270.21	245.76	175.74
Counts per unit radiance		0.676	0.891	1.034

****

CASE FOR NO ATMOSPHERE

Normalized radiance	0.1322	0.1505	0.1627	0.1730
TM L in W/m2.sr.um	252.04	268.07	245.07	175.87
Counts per unit radiance		0.681	0.894	1.034

****

Table 4. CALIBRATION OF THE THEMATIC MAPPER AT WHITE SANDS ON AUGUST 28, 1985.

Solar zenith angle Z: 35.954
Solar distance in AU: 1.0098
Junge size distribution: 3.77
Aerosol size range: 0.02 to 5.02 um
Refractive index: 1.54 - 0.01i
Time of overpass: 10:08.4 MST
Calculated visibility 200 km

Latitude: 32 deg 55 min
Longitude: 106 deg 22 min
Elevation: 1196 m
Pressure:658.1 mm Hg or 877.42 mbars
Temperature: 29.5 deg C
Relative humidity: 21%
Nadir viewing angle: 5 deg.

Thematic Mapper bands	1	2	3	4	5	7
Central wavelength um	0.4863	0.5706	0.6607	0.8382	1.6770	2.2230
Tau Mie	0.1016	0.0763	0.0588	0.0386	0.0112	0.0069
Tau Rayleigh	0.1412	0.0731	0.0403	0.0155	0.0009	0.0003
Tau ozone	0.0068	0.0287	0.0141	0.0016	0.0000	0.0000
Tau water vapor	0.0000	0.0000	0.0000	0.0341	0.0931	0.0604
Tau carbon dioxide	0.0000	0.0000	0.0000	0.0000	0.0094	0.0035
Single scattering albedo	0.8498	0.8311	0.8133	0.7824	0.6795	0.6324
Spectral reflectance	0.4973	0.5624	0.6018	0.6422	0.4260	0.1600
Eo across band in W/m2.um	1955.5	1826.9	1545.0	1042.8	220.19	74.78
Average image digital counts	>255.00	170.50	203.31	166.14	161.00	44.00
Preflight cal gains	15.553	7.860	10.203	10.821	78.751	147.719
Preflight cal offsets	1.8331	1.6896	1.8850	2.2373	3.2905	3.2117
IC cal gains for 28 Aug 1985	13.822	7.124	9.25	10.299	76.387	143.754
IC cal offsets for 28 Aug 1985	2.7930	3.0620	3.1170	2.7320	3.3040	4.0520
Normalized code radiance	0.1241	0.1327	0.1471	0.1496	0.0864	0.0358
Code TM L in W/m2.sr.um	237.90	237.77	222.84	153.02	18.65	2.63
Spectral L from preflight cal		214.77	197.42	151.47	20.03	2.76
Spectral L from IC cal		235.03	216.42	158.66	20.64	2.78
% (Code-Pre)/Pre		10.7	12.9	1.0	-6.9	-4.9
% (Code-IC)/IC		1.2	3.0	-3.6	-9.6	-5.5
Counts per unit radiance		0.717	0.912	1.086	8.631	16.754

****

CASE FOR RAYLEIGH ATMOSPHERE

Normalized code radiance	0.1304	0.1458	0.1555	0.1655	0.1096	0.0412
Code TM L in W/m2.sr.um	250.08	261.24	235.57	169.28	23.67	3.02
Counts per unit radiance		0.653	0.863	0.981	6.801	14.568

****

CASE FOR NO ATMOSPHERE

Normalized radiance 35.954	0.1281	0.1449	0.1551	0.1655	0.1098	0.0412
TM L in W/m2.sr.um	245.69	259.58	234.90	169.20	23.70	3.02
Counts per unit radiance		0.657	0.866	0.982	6.794	14.556

****

Table 5. CALIBRATION OF THE THEMATIC MAPPER AT WHITE SANDS ON NOVEMBER 16, 1985.

Solar zenith angle Z: 57.209
Solar distance in AU: 0.9886
Junge size distribution: 3.265
Aerosol size range: 0.02 to 5.02 um
Refractive index: 1.54 - 0.01i
Time of overpass: 10:07.4 MST
Calculated visibility: >200 km

Latitude: 32 deg 55 min
Longitude: 106 deg 22 min
Elevation: 1196 m
Pressure: 665 mm (886.7 mbars)
Temperature: 4.7 deg C
Relative humidity:45%
Nadir viewing angle: 5 deg.

Thematic Mapper bands	1	2	3	4	5	7
Central wavelength um	0.4863	0.5706	0.6607	0.8382	1.6770	2.2230
Tau Mie	0.0260	0.0212	0.0176	0.0131	0.0054	0.0000
Tau Rayleigh	0.1418	0.0738	0.0407	0.0156	0.0010	0.0003
Tau ozone	0.0054	0.0227	0.0112	0.0013	0.0000	0.0000
Tau water vapor	0.0000	0.0000	0.0000	0.0182	0.0496	0.0322
Tau carbon dioxide	0.0000	0.0000	0.0000	0.0000	0.0051	0.0019
Single scattering albedo	0.8894	0.8843	0.8801	0.8732	0.8550	0.8471
Spectral reflectance	0.4131	0.4805	0.5189	0.5629	0.3422	0.1116
Eo across band in W/m2.um	1955.5	1826.9	1545.0	1042.8	220.19	74.78
Average image digital counts	195.53	103.20	125.05	108.88	95.38	23.05
Preflight cal gains	15.553	7.860	10.203	10.821	78.751	147.719
Preflight cal offsets	1.8331	1.6896	1.8850	2.2373	3.2905	3.2117
IC cal gains for 16 Nov 85	13.889	7.204	9.402	10.354	77.19	145.191
IC cal offsets for 16 Nov 85	2.7120	2.5610	2.6000	2.3580	3.1380	3.8230
Normalized code radiance	0.0708	0.0769	0.0857	0.0908	0.0502	0.0174
Code TM L in W/m2.sr.um	141.72	143.70	135.43	96.90	11.31	1.33
Spectral L from preflight cal	124.54	129.15	120.71	98.55	11.69	1.34
Spectral L from IC cal	138.83	139.70	130.24	102.88	11.95	1.32
% (Code-Pre)/Pre	13.8	11.3	12.2	-1.7	-3.3	-0.7
% (Code-IC)/IC	2.1	2.9	4.0	-5.8	-5.4	0.7
Counts per unit radiance	1.380	0.718	0.923	1.124	8.433	17.293

****

CASE FOR RAYLEIGH ATMOSPHERE

Normalized code radiance	0.0725	0.0827	0.0891	0.0967	0.0589	0.0192
Code TM L in W/m2.sr.um	145.13	154.65	140.86	103.16	13.26	1.47
Counts per unit radiance	1.347	0.667	0.888	1.055	7.194	15.690

****

CASE FOR NO ATMOSPHERE

Normalized radiance	0.0712	0.0828	0.0895	0.0970	0.0590	0.0192
TM L in W/m2.sr.um	142.46	154.81	141.38	103.52	13.29	1.47
Counts per unit radiance	1.373	0.667	0.884	1.052	7.178	15.662

****

Conclusions

For the 12 reflectance-based measurements we have made in the TM visible bands, over a 16-month period, the RMS variation from the mean as a percentage of the mean is ±1.9%. For 11 measurements in the ir bands it is ±3.4% and the RMS variation for all 23 measurements is ±2.8%. These results are discussed in detail elsewhere.[2]

Acknowledgements

We wish to thank the following for their contributions to the satellite calibration program at White Sands while graduate students at the Optical Sciences Center, University of Arizona: C. J. Bruegge (nee Kastner), B. A. Capron, K. R. Castle, L. J. Lingg, A. L. Phillips, and S. L. Witman. We also wish to thank E. Ezra and several foreign scientists for their collaboration: H. Aoki, Che Nianzeng, M. C. Dinguirard, G. Fedosejevs, and P. M. Teillet. The assistance of D. Ferralez, D. Ream and R. K. Savage at the Atmospheric Sciences Laboratory at White Sands Missile Range is also gratefully acknowledged.

We wish to thank B. M. Herman for the use of his radiative transfer code, J. A. Reagan for the use of his solar radiometer, and both for useful discussions. Finally we wish to thank J. L. Barker and V. V. Salomonson for their encouragement and support under NASA contract NAS5-27382.

References

1. Herman, B. M. and S. R. Browning, "The effect of aerosols on the Earth-atmosphere albedo," J. Atmos. Sci. 32, 158-165, 1975.

2. Slater, P. N., S. F. Biggar, R. G. Holm, R. D. Jackson, Y. Mao, M. S. Moran, J. M. Palmer, and B. Yuan, "Reflectance and radiance-based methods for the in-flight absolute calibration of multispectral sensors," Remote Sensing of Environment, 1987, in press.

3. Begni, G., M. C. Dinguirard, R. D. Jackson, and P. N. Slater, "Absolute calibration of the SPOT-1 HRV cameras," Proc. SPIE 660, 1986, this issue.

SECTION III

DISCUSSION OF CALIBRATION RESULTS

Accepted for publication,
Remote Sensing of Environment
1987. (December 1986)

REFLECTANCE- AND RADIANCE-BASED METHODS FOR THE INFLIGHT ABSOLUTE CALIBRATION OF MULTISPECTRAL SENSORS

P. N. Slater, S. F. Biggar, R. G. Holm, R. D. Jackson†, Y. Mao,
M. S. Moran†, J. M. Palmer, and B. Yuan

Optical Sciences Center, University of Arizona, Tucson, Arizona 85721, and the †U. S. Water Conservation Laboratory, Agricultural Research Service, USDA, Phoenix, Arizona 85040.

Abstract

Variations reported in the in-flight absolute radiometric calibration of the Coastal Zone Color Scanner (CZCS) and the Thematic Mapper (TM) on Landsat 4 are reviewed. At short wavelengths these sensors exhibited a gradual reduction in response, while in the mid-infrared the TM showed oscillatory variations.

The methodology and results are presented for five reflectance-based calibrations of the Landsat 5 TM at White Sands, New Mexico, in the period July 1984 to November 1985. These show a ±2.8% standard deviation (one sigma) for the six solar-reflective bands.

Analysis and preliminary results of a second, independent calibration method based on radiance measurements from a helicopter at White Sands indicate that this is potentially an accurate method for corroborating the results from the reflectance-based method.

Introduction

With the advent of programs designed to monitor long-term changes in land processes, in the environment and in the global energy balance, the importance of absolute radiometric calibration of satellite-multispectral sensors has come to the fore. The on-board absolute-calibration methods now in use and the precision and accuracy requirements suggested for absolute calibration have been described elsewhere (Slater, 1984, 1985). To summarize, the requirements are that we know the stability of the calibration to a precision of within ± 0.5% of the saturation radiance, consistent with the noise-equivalent reflectance difference provided by high-performance sensors, and that the uncertainty in the knowledge of the absolute calibration should be in the range ±1% to ±5% depending on the requirements of the scientific investigation for which the calibration is to be used.

In this paper, we review the variations in the in-flight calibration of the Coastal Zone Color Scanner (CZCS) and the Thematic Mapper (TM) on Landsat 4. We then describe the improvements we have made to a reflectance-based method at White Sands, New Mexico, for the in-flight calibration of the TM on Landsat 5. We present results for five absolute calibrations of the solar-reflective bands of TM, and then compare these results with the preflight calibration and with values derived from the TM internal calibrator. We present results of an analysis of a second independent calibration method based on downward-looking ground-radiance measurements from a helicopter. In conclusion we mention future refinements to the reflectance-based technique, including attempts to characterize aerosols more accurately and to account for the adjacency effect and for some of the systematic errors introduced by the sensor's electronics.

Variations in Radiometric Calibration

We briefly describe here the variations noted in the calibration of the Nimbus 7 CZCS and the Landsat 4 TM.

With respect to the CZCS, it is worth noting that Gordon (1981), showed that a 5% error in sensor calibration and a 10% uncertainty in the exoatmospheric solar irradiance can combine to give rise to errors exceeding 200% in the retrieval of water reflectance values. Although 10% appears too high for the uncertainty in exoatmospheric irradiance (according to Frohlich, 1983, it should perhaps be 1% to 2%), and although water-reflectances are low and therefore relatively hard to measure accurately, the point remains that sensor calibration errors can cause large errors in reflectance measurements. Gordon showed that, by measuring aerosol optical thicknesses and water radiance simultaneously with the satellite measurement of total radiance, one can reduceé by an order of magnitude the error in determining water reflectance.

In the summer of 1979, Viollier (1982) compared CZCS-derived water-reflectance values with measurements made near the surface. He found that the satellite value was less than the surface value by 3.5% at 443 nm and greater than the surface value by 6.3% and 12% at 520 and 550 nm respectively. Viollier comments that, at the Fifteenth CZCS NET Meeting, Gordon reported corresponding values of -2%, +2%, and 7% but that Gordon had used a different set of calibration constants and exoatmospheric irradiance values.

Gordon et al. (1983a) have described a method for the atmospheric-correction of CZCS data that can, in conjunction with ocean reflectance measurements, provide a calibration of the sensor. Their method uses a Monte Carlo atmospheric radiative transfer model and an algorithm that includes a ratio of the aerosol optical depth at wavelengths of 520 nm and 550 nm to that at 670 nm, where the ocean reflectance is assumed zero. As Aranuvachapun (1983) points out, the accuracy of the algorithm depends mainly on the accuracy of this ratio, which is not currently measured by satellite remote sensing. The uncertainty of the method in determining pigment concentration is stated to be 30% to 40% over the concentration range 0.08 to 1.5 mg m^{-3}. In three direct comparisons between ship-measured and satellite-determined values of water-radiance, Gordon and associates claim that the atmospheric-correction algorithm had an average error of 10% to 15%.

By computing the radiance at the satellite from known water-radiance values, Gordon et al. (1983b) proceeded to force agreement between the sensor-recorded radiance and the computed radiance by adjusting the sensor calibration. Their results are shown in Figure 1 for band 1 of CZCS. The error bars represent the error induced by the uncertainty in the pigment concentration of the water. Elsewhere in this issue Gordon (1987) addresses the fundamental problems of calibrating CZCS observations.

Hovis et al. (1985) used the second on-board calibration lamp, which is used only occasionally, to check the calibration of CZCS after it had been in orbit for 5 1/2 years. They found no measurable change in the calibration, but it is important to note that the calibration lamp checks only the calibration of the focal plane detectors and associated electronics, as is also the case for the Multispectral Scanner System and the TM. In comparing CZCS data with data from a calibrated radiometer in a high altitude aircraft, Hovis and associates found a 25% degradation in the blue band, centered at 443 nm, after CZCS had been in orbit for four years and seven months. The longer wavelength bands exhibited progressively smaller degradations as shown in Figure 2. Because of the calibration-lamp results, the degradation is attributed to a reduction in the reflectances of the telescope optics and the scanning mirror.

Mueller (1985) has reported on the change in the calibration gains of the first three channels of the CZCS during its first four years of operation. Figure 3 shows the gains for the three channels centered at 443, 520, and 550 nm plotted against year and orbit number. The solid lines are linear regression models and represent the average fits over 20 replications with independent samples of Gaussian random noise. The circles represent decay coefficients calculated for pixels in the central water masses of the northeast Pacific subtropical gyre. The squares are data points generated using the radiometric-sensitivity decay correction models of Gordon et al. (1983b) with random noise, and the dashed lines are their models. Again the tendencies are as noted by the authors cited earlier, although it is interesting to note the linear fit used by Mueller compared to the quadratic fit used by Gordon et al.

Frequently recorded values for the internal-calibrator (IC) gains and offsets for the solar-reflective bands of TM on Landsat 4 have been summarized by Barker (1985a). Figure 4 compares the preflight calibrations with the values from the IC. Again the results, as for the CZCS lamp-based calibration, apply only to changes in the focal-plane filters and detectors and the associated electronics. The graphs in Figure 4 are divided into three sections. The left section shows the preflight calibration conducted under thermal-vacuum conditions. The middle section shows the results of in-orbit IC calibrations during the so-called Scrounge image-processing era. The third section shows the results during the Thematic mapper Image Processing System (TIPS) era. The gains, G, are band averages of 16 detectors derived from the regression equation P = (G x E) + O where P is the observed IC pulse, E is the preflight value of the IC "effective" spectral irradiance, and O is the offset.

The results in Figure 4 show decreases in the apparent gains for band 1 amounting to 7% and 13% after 500 and 600 days from launch, respectively. Bands 2 and 3 show a similar pattern but with a smaller loss in gain. Band 4 departs from the trend exhibited by bands 1, 2, and 3 in showing a gain increase for the last calibration. Bands 5 and 7 show oscillatory changes in gain. The amplitude of phase the oscillations is about 7%. Except for the cyclic pattern in bands 5 and 7, which are of unknown orgin, Barker (1986a) considers most of the changes to be IC- temperature dependent effects and estimates that their magnitude can range between zero and 15% depending on the detector band and IC-flag temperatures at the time of data acquisition. We repeat that, at best, IC-based results are indicative only of changes in the filter-detector-electronics part of the system and that superimposed on them should be the changes that occur in the reflectances of the optical components of the telescope and scan mirror.

Reflectance-based calibration of Meteosat

In addition to the work described earlier on the in-flight calibration of the CZCS by reference to known water reflectances, the work of Koepke (1982) on the reflectance-based calibration of Meteosat is noteworthy. He used a radiative transfer program that accounts for multiple scattering in conjunction with ground reflectance data and atmospheric data, to predict the radiance at the entrance pupil of Meteosat I. Atmospheric water vapor was calculated using data from the nearest radiosonde, and the climatological values of ozone and oxygen were assumed. Ground level barometric pressure defined the Rayleigh optical depth, and aerosol optical depths were derived from visibility data. Four test sites were used: rough ocean, the savanna in Namibia, pastureland in northern Germany, and freshly fallen snow. Bidirectional-reflectance data were collected for these sites over a period of several months. Histograms of digital-image counts of these areas typically filled less than three columns, and often one column contained 60% of the pixels. We note, however, that Meteosat quantizes data to 6 bits, so for low reflectances a three-column spread represents a large variation in reflectance. Nevertheless, by using four targets and pointing the sensor into deep space, which fixed the offset point on the counts-versus-radiance curve, Koepke estimated the uncertainty to be on the order of 6%. This resourceful use of colateral data provided a valuable calibration of Meteosat 1. Koepke's estimate of a 6% uncertainty probably represents a lower limit on the uncertainty of the method because of its dependence on reflectance data that were not collected simultaneously with the Meteosat imagery and because of the use of visibility estimates that provide only approximate values for optical depths.

Reflectance-based calibration at White Sands

On January 3, 1983, we made our first reflectance-based measurements at White Sands, New Mexico, to determine the absolute calibration of the Thematic Mapper on Landsat 4 (Castle et al. 1984, Kastner 1985). Since then we have made five more sets of measurements for the TM on Landsat 5. During this period we have made improvements with respect to (1) site location, (2) instrumentation, (3) measurement methodology, particularly the measurement of absolute spectral reflectance factor, and (4) data reduction and presentation. These and related topics will be discussed below.

Site Location

The alkali flats region at White Sands Missile Range was chosen for reflectance-based calibration purposes because it is a flat, extended area and, in the visible and near infrared, is of high, uniform reflectance. In addition, it is close to being a lambertian reflector, and it is at an elevation of about 1200 m in a region where the atmospheric aerosol loading is low and the expectancy of clear weather is high.

We require a flat surface to avoid topographically-induced variations in radiance across the site. Its being situated near the middle of a high reflectance area about 30 x 30 km in extent results in the atmospheric adjacency effect (Pearce, 1977) being negligible except in band 1. Santer (1986), using the "5-S" atmospheric program of Tanré et al (1985) estmates that the adjacency effect causes our predicted radiance values to be about 1% too high in TM band one; the percentage decreases as the wavelength increases. High reflectance and site elevation as well as low aerosol loading reduce the uncertainty in the calibration associated with characterizing the aerosols present (see the later discussion of results). A near-lambertian surface minimizes the errors introduced by the change in the solar zenith and azimuth angles during the roughly 45 minutes required to measure the reflectance of our 640 x 120 m site.

The location for our first measurements on January 3, 1983 was Cherry Site near the southern end of the Northrup strip. We subsequently moved two miles east to Chuck Site where we occupy a building serviced by telephone and electricity. It is near a 90^{o} turn in a compacted gypsum road that is detectable on a contrast-stretched TM image, this greatly facilitates the location of our measurement area on the image. Another advantage of Chuck Site is that it is 2 - 3 m higher in elevation than Cherry

Site and many other areas of the alkali flats region of White Sands. We have noticed that these lower lying areas are flooded after heavy rains, sometimes to a depth of 20 - 30 cm, while the area around Chuck Site is not.

New Instrumentation

In this section we briefly describe the design and operation of a new spectropolarimeter, two models of which exist, one can be mounted on a helicopter and the other is attached to an auto-tracking mount, also described. Both instruments provide polarization data within spectral intervals of 10 nm or 20 nm. They can cover a 1^{o}, 2^{o} or 5^{o} field of view and have a dynamic range of 10^{4} by use of neutral density filters. A lap-top computer is used for data collection and storage purposes. The spectropolarimeter attached to the auto-tracking mount in principally used as a solar radiometer, although the tracking mount can also be programmed to provide sky scans. The solar radiometer has the capability, using a Si and a PbS detector, of making measurements from 0.42 to 2.5 μm. The automatic- tracking capability provides more accurately timed data than can be obtained using a manually operated instrument. The helicopter instrument at present operates only over the range 0.44 μm to 1.04 μm; in other respects the spectropolarimeters are identical.

Each instrument weighs 11 kg, measures 19 x 26 x 28 cm, and requires 10 - 12 watts to operate. A field stop at the focus of the objective lens of each instrument defines its angular field of view and a field lens forms an image of the aperture of the objective lens onto the detector. The position of the filter and aperture wheels, polarizer, wave plate, and detector assembly are computer controlled with precision placement and monitoring performed by a combination of stepper motors and encoders.

A silicon photodiode detector, model UV444-B from EG&G, was chosen for the visible and near ir (0.4 - 1.1 μm) because of its ruggedness and linearity over a large dynamic range. A PbS detector model #2309 from IR Industries was chosen for the range 1 to 2.5 μm. The detectors are mounted in a machined slide allowing both detectors to use the same optics. The detector slide is heated to a stable temperature of about 50^{o}C. The thermal drift is low enough to give a useful signal-to-noise ratio in the ir. However, the ground radiance is too low for the use of an uncooled ir detector in the helicopter instrument.

In the solar instrument, 10 narrowband filters were selected to assist in the characterization of atmospheric constituents in the 0.4 to 1.04 μm range. Five narrowband filters with central wavelengths in atmospheric windows are used to determine the aerosol optical depth. Three filters in the Chappuis band and one in the water-vapor band are used to determine the extinction due to ozone and water vapor. Three additional filters are provided to cover the ir, two at the band centers of TM bands 5 and 7 and one narrowband filter centered at 2.25 μm.

The portable spectropolarimeter used in the helicopter for measurements of the site from 3000 m above mean sea level (MSL) contains filters that closely match those in the first four TM bands. In addition there are eight narrowband filters identical to those used in the solar instrument.

Figure 5 is a schematic of the optical, mechanical and electronic components of the spectropolarimeter. Light enters the instrument through a protective window, then through neutral density and spectral filters, and then through the objective lens, quarterwave plate, field lens, field stop, polarizer, to the detector. The instrument cycles through the spectral filters, taking two polarization measurements for each filter (the measurements are simply averaged when the spectropolarimeter is used as a solar radiometer). When cycling through the ir filters, the PbS detector is moved into position and the Si detector is moved out. The detector signal is amplified and then digitized by a 12-bit A/D converter. If the signal is out of range of the A/D converter, the appropriate neutral density filter is moved into position and a new reading is taken. The data are stored on a Radio Shack, TRS 80 model-100 portable computer for later analysis.

The computer controls the operation of the instrument and acquires and stores the data. The positioning of each component is controlled by stepper motors. The positions of the components are continually monitored through a set of 2-, 3- or 4-bit encoders. The time is accurately recorded for each data point by reference to the internal clock of the model 100.

When the instrument is used as a solar radiometer, pointing accuracy and temporal resolution of the data are maintained by an automated elevation-azimuth tracking mount. The mount consists of a tripod, a control box, and two turntables and a yoke. The control box contains power supplies and control interface electronics for the spectropolarimeter and the tracking turntables. The radiometer is moved in azimuth and elevation by two stepper-motor-powered precision turntables. The position of each turntable is monitored by two 12-bit, absolute-position rotary encoders. The computer calculates the sun's position and sends appropriate commands to correct the positions of the turntables. The solar tracking is updated every 30 seconds and, typically, a complete data set of 12 spectral bands is taken every three minutes.

As expected, the maximum elevation error for the tracker (0.35^{o}) occurs when there is maximum solar change in elevation. Similarly, the maximum error for azimuth, (0.5^{o}) occurs close to noon when there is a maximum change in azimuth angle.

The results of a laboratory experiment have shown that a pointing error of $\pm 0.8^{o}$ for a 2^{o} field of view and $\pm 2^{o}$ for a 5^{o} field of view do not introduce a significant change in the output of the spectropolarimeter. The accuracy of the tracker program is then adequate for our purposes.

The solar instrument, although attached to a heavy tripod and control box, is portable and can be set up easily in nearly all remote field sites so long as 115 V AC power is available. The helicopter instrument is battery operated and is more portable, requiring only a 5 kg battery-interface box and a lap-top computer. It can be attached to a mount on a helicopter, or to a yoke for field measurements.

Ground-based, Reflectance-Factor Measurements

Reflectance-factor measurements of the gypsum sand at White Sands, New Mexico were made using two commercially available radiometers specifically designed for ground-based reflectance measurements in support of satellite experiments. The first, a Barnes Modular Multispectral 8-channel Radiometer[1] (Robinson et al., 1981), nominally duplicates the six TM solar reflective bands. An MMR band without a counterpart on the TM (1.15 to 1.3 μm) will not be discussed here. The second instrument, an Exotech model 100-AX, nominally duplicates the first four TM bands. We devised a backpack transport system to suspend a radiometer about 1 m to the right side and slightly above the operator's shoulder level. This system (known as "yoke" or "wings") allows numerous measurements to be made rapidly over an extensive ground area without the need for vehicles. Data were recorded with portable acquisition systems mounted on the front of the backpack system within easy sight and reach.

The absolute reflectances of the gypsum sand targets were estimated by reference to $BaSO_4$ panels. The panels used were constructed by Che Nianzeng at the Optical Sciences Center and calibrated using the field method of Jackson et al. (1987).

Four 16-pixel areas (each pixel representing 30m x 30m) were aligned parallel to the track of Landsat 5 at the Chuck Site. The layout of the sampled area is shown in Figure 6. The measurement sequence for the MMR began at the southeast pixel (nearest the block house at the Chuck Site). First, a set of 12 readings was made over the $BaSO_4$ reference panel, then 12 readings about 2 m apart were made on each of the four southernmost pixels, returning to the east on the four pixels immediately adjacent to the north, returning west on the next set of four, and again east on the fourth set of four.

---

[1] Trade names and company names are included for the convenience of the reader and imply no endorsement of the product or company by the University of Arizona or the United States Department of Agriculture.

The path was north-south centered on each pixel (the MMR readings are diagramed as open circles in Figure 6). Following the first 16-pixel set, another 12 readings were taken on the $BaSO_4$ reference panel, and the next 16-pixel set was taken. Panel readings were taken after each 16-pixel set.

The Exotech measurement path was north-south, east-west, centered on the pixels (depicted as dots in Figure 6). As with the MMR, 12 reference-panel readings were taken first, then the southwesternmost pixel, proceeding four pixels north, then back south in the four pixels immediately east. The 16-pixel set was completed on the southeasternmost pixel. Panel readings were made after each 16-pixel set. Approximately 45 minutes were required to record 64 pixels with 24 readings per pixel. The time was centered on the satellite overpass time.

The above described measurement sequence was followed for August 28, 1985 and November 16, 1985. For May 24, 1985, only the MMR was used (open circles in Figure 6). On July 8, 1984, and October 28, 1984, only the first 16-pixel set was measured, and only with the MMR.

Reflectance-factor calculations

Reflectance factors were obtained by ratioing the voltage measured over a target to the voltage measured over a $BaSO_4$ reference panel, multiplied by the reflectance factor for the reference panel at the particular solar zenith angle. Although fewer than 10 minutes elapsed between reference panel readings, the voltages were interpolated to the time of target measurement. Details of the reduction of the field measurements to provide reflectance-factor data appropriate for satellite calibration are described in Jackson et al. (1986).

The 12 measurements for each pixel and for each instrument were averaged to produce a single estimate of the reflectance factor for each pixel (typical standard error = ±0.005). Next, 16-pixel averages were calculated for each of the four 120 x 120 m areas. Combining the results from the two instruments yielded 384 measurements for each area, for a total of 1536 measurements over the 120 x 480 m area for the first four TM bands. Results of this procedure for two dates are given in Table 1. The data in Table 1 show good agreement between the two radiometers, and indicate the small reflectance differences between the four 16-pixel areas.

Nonlambertian properties of gypsum sands

Because 40 to 45 minutes were required for the reflectance-factor measurements, it was necessary to evaluate the nonlambertian properties of the gypsum sands to determine whether changes in sun angle during the course of the measurements caused differences in the reflectance factors. On two occasions, reflectance-factor measurements were made of the same target at several sun angles. Data for one day are presented in Table 2. For sun zenith changes from 73.4^{o} to 34.5^{o}, reflectance factors for the first four TM bands changed very little, well within the error of measurement. We conclude that the gypsum sands are essentially lambertian for nadir measurement and for this range of solar zenith angles. Departure from lambertian characteristics have been observed with nonnadir angles (Begni et al. 1986).

Comparison of radiometer and TM spectral responses

Band response functions for the two radiometers differ slightly from each other and from those of the TM. Since the purpose of making the measurements was to estimate the reflectance factor pertinent to the TM, it was necessary to examine whether the difference in response functions was significant.

Reflectance spectra were measured at Chuck Site on March 8, 1986 by Teillet and Fedosejevs (1986). Reflectance factors for the various bands of the TM, MMR, and Exotech were determined by summing the product of the spectra and the response function for each band of each instrument, and dividing by the integral of the response function over each band. Ratios of the reflectance factors for the TM in relation to the MMR and Exotech are shown in Table 3. The differences are less than 1%.

Numerical procedure for locating site on TM imagery

Reflectance-factor values for the 64 pixels were used in a simple BASIC program to identify the site in the TM data. Reflectance-factor values were converted to approximate digital counts to reduce the effect of rounding errors. A window of TM digital counts (DCs) covering an area encompassing the site was compared, pixel by pixel, to the array of reflectance-factor-based DCs. The standard deviation of the differences between the TM-pixel DCs and the reflectance-factor-based DCs was calculated for the first 64 pixels of the array. Next, the set was moved one column and the new deviation was calculated. The 64-pixel overlay was moved over all columns, then lowered a row, and over all columns again until all pixels in the array had been compared with the reflectance-factor-based DCs. The site was indicated by the position of the overlay having the lowest standard deviation. This procedure quantified the otherwise subjective visual location of subtle differences on the generally uniform white gypsum.

Description of data summary tables

Table 4 lists the results of the TM-5 calibrations at White Sands on October 18, 1984. Tabular summaries for July 8, 1984, May 24, 1985, August 28, 1985, and November 16, 1985, can be found elsewhere (Slater et al, 1986).

The determination of the quantities listed in Table 4 is briefly as follows. The Rayleigh optical depth was determined from a knowledge of the barometric pressure and wavelength. The total optical depths were determined from the slopes of Langley plots in which the log voltages from the solar radiometers were plotted against air masses. In spectral regions unaffected by absorption, the Mie optical depth at any wavelength was determined by subtracting the Rayleigh from the total optical depth at that wavelength. An optical depth versus wavelength curve was fitted through the points that spanned the absorption region due to ozone. The difference between the values on this curve at a given wavelength and the total minus Rayleigh value at the same wavelength gave the ozone optical depth at that wavelength. A Junge radial size distribution (Junge, 1963) was assumed for the aerosols. The Junge ν parameter is defined in the equation

$$\frac{dN}{dr} = Cr^{-(\nu+1)}$$

where N is the number of particles, r is their radius, and C is a constant. The value of ν, needed to find the aerosol phase function, was determined from the slope of the log τ_{MIE} versus log λ curve.

A computer program by Dave (1969) was used to determine the scattering phase function and the single scattering albedo. This program in included as one of the subroutines within the Herman code.

The LOWTRAN 6 program by Kneizys et al. (1983) was run to determine the transmittances of water vapor and carbon dioxide in the solar-reflective bands. Average optical depths for water vapor and carbon dioxide (τ_{H_2O} and τ_{CO_2}) were determined for TM bands 4, 5, and 7 by integrating the LOWTRAN transmittance spectra between the spectral response limits of the TM bands as defined by Palmer (1984). The τ_{H_2O} values were found to be 0.035, 0.0915, and 0.0594, and the τ_{CO_2} values were 0.0, 0.0094, and 0.0035 respectively. The range of predicted τ_{H_2O} values for White Sands was determined by scaling these τ_{H_2O} values by the ratio ρ_{H_2O} (O, RH, T)/0.59, where ρ_{H_2O} (O, RH. T) can vary, at White Sands, between 0.01 and 1g $cm^{-2}km^{-1}$. The relative humidity and temperature were measured at Chuck Site at the time of overpass. The amount of atmospheric water vapor was then determined from a family of curves of different constant relative humidities that are on a graph of water vapor concentration plotted against temperature (McClatchey et al., 1972).

The normalized code radiances refer to the results of calculations using a radiative transfer code described by Herman and Browning (1975). The radiances are at the entrance pupil of the TM for unity exoatmospheric spectral irradiance. For use in the code, the atmosphere is divided into a sufficient number of plane-parallel layers such that changes within each layer are due only to single-scattering processes. The Gauss-Seidel iterative technique is used to solve the equation of radiative transfer. Upon convergence, all multiple scattering effects have been taken into account. Values of 5.02, 0.02, and 0.04 μm were used for the maximum and minimum radii and incremental step size, respectively, for the aerosols. The aerosols were given a refractive index of 1.54-0.01i, an average value for the region as measured by Jennings et al. (1978). A vertical aerosol distribution as measured by Elterman (1966) was assumed.

The exoatmospheric spectral irradiance data are those recommended by Fröhlich and published by Iqbal (1983). They represent a carefully edited combination of results published by Neckel and Labs, Thekaekara, Arvesen and others. The values were adjusted to yield an integrated value of 1367 Wm^{-2}, the solar constant as proposed by the World Radiation Center.

The code TM spectral radiance is the product of the exoatmospheric irradiance and the normalized radiance determined from the Herman code.

The average number of image digital counts was determined for the TM image of the site. For the first measurement the site comprised two areas each 4 x 4 pixels in size on opposite sides of a compacted-gypsum road. For the second measurement the site was 8 x 4 pixels on the north side of the road, and in the last three cases it was 16 x 4 pixels, also north of the road. For our calibration of the Landsat 4 TM (Castle et al., 1984), we had to identify the particular detectors crossing the 4 x 4 pixel area. This is not so important for the Landsat 5 TM because the detector response uniformity is much better. Nevertheless we did decide to measure the reflectance of an area 16 pixels long in the track direction so as to be taking all detectors into account in the average value used for calibration.

We used data supplied by Barker (1985b and 1986b) to compare our calibration to those obtained preflight and in-flight from the internal calibrator (IC). The relation between average spectral radiance, L_T, and digital counts, DC, is $L_T = (DC - O)/G$, where G and O are gain and offset. The average values for the gains and offsets of the 16 detectors in each band are listed in Table 4 for all the bands. The absolute calibration is given in counts per unit spectral radiance to provide a value that appropriately decreases with a decrease in the transmittance of the optics or with a reduction in the responsivity of the detectors. A single value is an adequate description of the calibration of the TM because the preflight calibration and IC show the system is extremely linear in its response. Only for low radiance cases, corresponding to less than about 30 DCs, does the system depart from linearity.

The lower two sections of Table 4 are included to compare our results with those computed for a Rayleigh atmosphere and no-atmosphere.

Discussion of reflectance-based calibration results

The spectral radiance results in Table 4 for TM bands 1 to 4 are graphed in Figure 7. The abbreviations beneath the figure apply to spectral radiance values as follows: PRE, the values corresponding to the preflight calibration gains and offsets and the digital counts for the image of the site; IC, the values corresponding to the internal calibrator gains and offsets for that day and the digital counts for the image of the site; CODE, the values as determined from the ground and atmospheric measurements, a knowlege of the exoatmospheric irradiance, and use of Herman's radiative transfer code; HELI, the radiance values measured by the helicopter, where the additional lines at the top of these bars show the helicopter values as corrected by reference to the percentage differences in Figure 12; and RAY, the values using the same spectral reflectances and exoatmospheric radiances as used in the CODE but assuming a Rayleigh atmosphere

Several points are noteworthy. First, the CODE and corrected HELI values agree closer with the IC values in bands 1, 2 and 3 than with the PRE values. Second, the PRE values are always less than the IC and corrected HELI values; band 4 provides the single exception of the PRE exceeding any other value. This indicates that, on this date, TM had less responsivity than preflight, and, because the IC values generally tend to be lower than the CODE and corrected HELI values, the decrease in response is likely to be due to both a decrease in transmittance of the telescope and a decrease in response of the filter/detector/electronics. Third, the corrected HELI values agree well with the CODE values. This is particularly true for TM bands 1, 2 and 3. The difference between the CODE and HELI values in band 4 may be due to a systematic error in the calibration of the helicopter radiometer and/or an error in the assumptions used in the code, eg., the Junge ν value or the complex index of refraction of the aerosols, which has been assumed to be wavelength independent. Finally, in earlier presentations of these data, for example, Biggar et al. (1985), substantial differences were reported between PRE and IC and the CODE, HELI, and RAY values. Recently, these differences have been found to be due to the inadvertent use of an image extraction program that rescaled the image to set the maximum pixel digital count in the image to 255. This gave rise to errors that varied from band to band and that were tentatively explained as being due to luminescence effects in the thin atmosphere that surrounds the spacecraft following an adjustment of the orbit. Fortunately, the present consistent results do not require such an imaginative explanation.

Figure 8 compares the counts per unit radiance for our five measurement dates. It is evident that there is a general tendency for the counts per unit radiance, ie., the system response, to decrease over the 16-month measurement period. In contrast to the results reported earlier for the CZCS, the results do not show a noticeable wavelength dependence.

Figure 9 compares the average values for counts per unit radiance for the five measurements with the average IC-derived values for four dates (no IC data are available for May 24, 1985). There is excellent agreement between the CODE and IC values in the visible and less, but still good agreement in the ir. The band 5 and 7 comparisons, it should be remembered, are inadequate because only three data sets are involved, and Barker (1986a) has noted that the IC response for the TM-5 may be oscillatory as it was for TM-4 (see Figure 4).

The results in Table 4 for October 28, 1984 and those for the other four dates (Slater et al., 1986), include results for a Rayleigh atmosphere and no atmosphere. It is interesting that for TM bands 1 through 5 and band 7 the full-atmosphere radiances are 93%, 89%, 92%, 85%, 70%, and 80% of the radiances for the Rayleigh case respectively. The small differences between the spectral radiances for the Rayleigh and full atmosphere cases are due to aerosol scattering and absorption. The latter cannot be so accurately determined as the surface spectral reflectance and barometric pressure, which are all that are required as input to a radiative transfer code to determine the spectral radiance at the top of a Rayleigh atmosphere. Thus the major component of the spectral radiance can be determined accurately at White Sands because of its high surface reflectance and elevation and atmospheric visibility. Fortunately, the uncertainties introduced into the final result by the more difficult quantities to determine, for example, aerosol scattering and absorption, have a secondary effect on the final result. Also interesting is the extremely close agreement between the Rayleigh and no-atmosphere results in Table 4. These show that the attenuation by scattering in the Rayleigh case is almost exactly offset by the path-radiance component incident at the satellite.

Radiance-Based Methods

Figure 7 shows that the radiances as measured at 3000 m MSL at White Sands are about the same as those measured by the TM. This result prompted a more detailed examination of the variation of radiance with altitude as a function of wavelength, reflectance, and visibility.

Starting with the atmospheric conditions of October 28, 1984, at White Sands and with a solar zenith angle of 35^0 we calculated radiance values for altitudes between ground level (1196 m at White Sands) and 21,000 m (the operational altitude MSL of the

NASA U-2 or ER-2 aircraft) and for above the atmosphere. Graphs were then plotted of the percentage difference (the differences between the radiance above the atmosphere and at an intermediate altitude divided by the radiance above the atmosphere, the whole quantity expressed as a percentage) against MSL. These are shown in Figure 10 for the first four solar reflective TM bands. As anticipated, the results for reflectances less than 0.1 show large percentage differences, but what is intriguing is the sign change in the percentage difference for reflectances between 0.25 and 1.0 for bands 1, 2, and 3 and between 0.1 and 0.25 for band 4. These results show that, for a reflectance of 0.5 and an altitude of 3000 m MSL, the percentage differences are +2.5, -1.0, -1.0, and -2.0 for bands 1, 2, 3, and 4 respectively. This verifies the experimental observation that for the White Sands conditions of October 28, 1984, helicopter radiance values at an altitude of 3000 m MSL are close to those for space and require only a small correction, which can be made accurately.

With this promising result, the investigation was extended to determine how general this condition might be. Visibilities of 10 and 23 km were considered for a reflectance of 0.5 at all wavelengths. The input values are listed in Table 5, the refractive index was 1.54-0.01i in all cases, and Junge ν values of 2.9 and 2.6 were used for the visibilities of 10 and 23 km respectively.

The output plots of percentage difference, as defined earlier, against altitude above MSL are shown as Figures 11 and 12 together with the Rayleigh atmosphere curve for a wavelength of 0.49 μm. The positive difference for $\lambda = 0.49$ μm is due to the fact that the large path-radiance term contributed more to the total radiance than is lost by the attenuation of the ground-reflected term. The other curves show increasing negative differences for altitudes approaching ground level, owing to the heavy aerosol loading in the lower atmosphere. The bowing of the $\lambda = 0.57$ μm and 0.66 μm curves at intermediate altitudes is due to reduced path-radiance from Rayleigh scattering and the presence of ozone absorption at those altitudes. Note that for an altitude of 3000 m and a visibility of 23 km the percentage differences are +3.0, -1.4, -0.9, -0.8, -2.3, and -1.6 for wavelengths of 0.49, 0.57, 0.66, 0.84, 1.67, and 2.22 μm respectively. Furthermore, the percentage differences are less than twice these values for a visibility of 10 km, as can be seen from the remarkable similarity between Figures 11 and 12.

Conclusion

Satellite multispectral sensors typically exhibit reduced sensitivities in flight compared to preflight. In the case of the CZCS, an exponential degradation has been noted that is greater in the short wavelength bands than in the long wavelength bands. The results presented here for the TM visible bands demonstrate the same lower sensitivity in flight than preflight and suggest that there is a tendency for this to be wavelength dependent but to a lesser degree than for the CZCS. Also the observation by Hovis et al. (1985) that the decrease in the CZCS response is due entirely to a reduction in the transmittance of the telescope may not hold for the TM. For the TM visible bands, our reflectance-based and radiance-based measurements, taken in conjunction with the internal calibrator results, indicate that the reduction in sensitivity may be due partly to a loss in telescope transmittance and partly to a loss in sensitivity of the filters, detectors, and associated electronics.

For the 12 reflectance-based measurements we have made in the TM visible bands, the RMS variation from the mean as a percentage of the mean is ±1.9% over a 16-month period. For 11 measurements in the ir bands it is ±3.4%. The RMS variation for all 23 measurements is ±2.8%. (All RMS variations are one sigma.) Whether the higher RMS variation in the ir is because the system response is less stable in the ir than in the visible or because there are inaccuracies in our determination of the effect of water-vapor absorption, or a combination of the two, is hard to ascertain. Sensitivity analyses, (Kastner and Slater, 1982; Kastner, 1985) have shown that a large uncertainty (30%) in water-vapor content for mean conditions at White Sands of 0.1 g $cm^{-2}km^{-1}$ changes the radiance in TM band 5 by only 2%. It seems probable therefore that the observed variations are due mainly to changes in the system's response. Incidentally, we are at a disadvantage with respect to bands 5 and 7 because an inadequate-signal-to-noise ratio prevents our making ground-radiance measurements with the spectropolarimeter from a helicopter in these bands.

A comparison between the counts per unit spectral radiance as determined by our measurements (CODE), the preflight calibration (PRE), and the internal calibrator (IC) in-flight shows excellent agreement between CODE and IC values in the visible but consistently high values for the PRE, and good agreement between the PRE and IC values in the ir but consistently high values for CODE. As pointed out by Markham and Barker (1986) there are significant changes in the output of the IC with temperature of the IC flag in bands 5 and 7. The IC on TM-4 showed a ±7% oscillatory variation in bands 5 and 7. This probably also occurs in TM-5 but there are insufficient data to prove this (Barker, 1986a). Thus, although the evidence is not conclusive, there are independent indications that the IC calibrations are less reliable in bands 5 and 7, and perhaps in band 4, than in bands 1, 2, and 3.

The measurement of reflected spectral radiance by a helicopter at 3000 m MSL has been shown experimentally and theoretically to offer a precise alternative procedure to reflectance-based calibration for bands in the visible and near ir. However, when a given calibration method, such as the reflectance-based method described here, is said to provide results that agree to within ±2.8%, this is an uncertainty in precision and not necessarily in absolute accuracy. The value of a precise, independent second method, which can be used simultaneously with the first, is that when the two agree to within their error budgets, we can become more confident that their precision represents an absolute accuracy. This then is one important reason for making the helicopter radiance-based measurements and the reason we hope others will continue their independent calibration studies at White Sands.

Having achieved an uncertainty in precision of ±2.8% for our calibrations at White Sands, we plan to refine the measurements and modify the digital counts obtained at White Sands. We expect the most important improvements will be achieved by making sky polarization measurements and reflected- radiance measurements from a helicopter at the time of sensor overflight. The results of the polarization measurements should improve our knowledge of the aerosol size distribution and the real part of the aerosol refractive index. The use of helicopter radiance data with ground reflectance and optical-depth data will permit a comparison of actual and predicted spectral radiances at the helicopter altitude. We anticipate that a change in the imaginary part of the aerosol refractive index, which is used in the radiative-transfer code, will allow the results to be equalized. This seems to be a promising method to determine the effective imaginary part of the refractive index in the vertical air column above the ground site — a quantity that is difficult to measure by other methods and that probably represents the greatest uncertainty in the calibration. We also plan to determine the effect of the low-reflectance area surrounding White Sands on the code-predicted radiance values at the sensor, which assume an infinite surface of uniform reflectance. Finally, there are several TM detector-electronic effects that must be taken into account now that the 3% level of precision has been reached. These include the memory effect, the unequal quantization bin sizes, and other small radiometric errors that may amount, at the most, to three digital counts or about 2% of the radiance level for TM bands 1 to 4 at White Sands. Further information on these effects can be found in other papers in this issue and in a special issue of Photogrammetric Engineering and Remote Sensing devoted to the Landsat Image Data Quality Assessment program (Markham and Barker, 1985).

Acknowledgements

We wish to thank the following for their contributions to the satellite calibration program at White Sands while they were graduate students at the Optical Sciences Center, University of Arizona: C. J. Bruegge (nee Kastner), B. A. Capron, K. R. Castle,

L. J. Lingg, A. L. Phillips, and S. L. Witman. We also wish to thank C. E. Ezra and several foreign scientists for their collaboration: H. Aoki, Che Nianzeng, M. C. Dinguirard, G. Fedosejevs, and P. M. Teillet. The assistance of D. Ferralez, D. Ream and R. K. Savage at the Atmospheric Sciences Laboratory at White Sands Missile Range is also gratefully acknowledged.

We wish to thank B. M. Herman for the use of his radiative transfer code, J. A. Reagan for the use of his solar radiometer, and both for useful discussions. Finally we wish to thank J. L. Barker and V. V. Salomonson for their encouragement and support under NASA contract NAS5-27382.

References

Aranuvachapun, S. (1983), Variation of atmospheric optical depth for remote sensing radiance calculations, Remote Sens. Environ. 13, 131-147.

Barker, J. L. (1985a), Relative radiometric calibration of Landsat TM reflective bands. Landsat-4 Science Characterization Early Results. Vol. 3, part 2. NASA Conf. Pub. 2355, 1-219.

Barker, J. L. (1985b and 1986b), Thematic mapper radiometric and algorithm performance program (TRAPP), communication to the authors.

Barker, J. L. (1986a) NASA Goddard Space Flight Center, communication to the authors.

Begni, G., Dinguirard, M. C., Jackson, R. D., and Slater, P. N. (1986), Absolute calibration of the SPOT-1 HRV cameras, SPIE, 660, in press.

Biggar, S. F., Bruegge, C. J., Capron, B. A., Castle, K. R., Dinguirard, M. C., Holm, R. G., Lingg, L. J., Mao, Y., Palmer, J. M., Phillips, A. L., Slater, P. N., Witman, S. L., Yuan, B., Jacson, R. D., Moran, M. S., and Savage, R. K. (1985) Absolute calibration of remote sensing instruments, *Proc. 3rd Int. Colloq. on Spectral Signatures of Objects in Remote Sensing*, Les Arcs France, ESA SP-127.

Castle, K. R., Holm, R. G., Kastner, C. J., Palmer, J. M., Slater, P. N., Dinguirard, M., Ezra, C. E., Jackson, R. D., and Savage, R. K. (1984), Inflight absolute radiometric calibration of the Thematic Mapper, IEEE Trans. Geosci. Remote Sensing GE-22, 251-255.

Castle, K. R., (1985), Absolute radiometric calibration of a spectropolarimeter, PhD Dissertation, University of Arizona, 129 pp.

Dave, J. B. (1969) Scattering of electromagnetic radiation by a large, absorbing sphere, *IBM J. Res. Rev.*, May, 302-313.

Elterman, L. (1966) Aerosol measurements in the troposphere and stratosphere. Appl. Opt. 5, 1769-1776.

Fröhlich, C. (1983), Data on total and spectral irradiance: comments, Appl. Opt. 22, 3928.

Gordon, H. R. (1987) Calibration requirements and methodology for remote sensors viewing the ocean in the visible, *Remote Sensing Environ.* this issue.

Gordon, H. R. (1981) Reduction of error introduced in the processing of coastal zone color scanner-type imagery resulting from sensor calibration and solar irradiance uncertainty, *Appl. Opt.* 20, 207-210.

Gordon, H. R., Clark, D. K., Brown, J. W., Brown, O. B., Evans, R. H., and Broenkow, W. W. (1983a), Phytoplankton pigment concentrations in the Middle Atlantic Bight: Comparison of ship determinations and CZCS estimates, *Appl. Opt.* 22, 20-36.

Gordon, H. R., Brown, J. W., Brown, O. B., Evans, R. H., and Clark, D. K., (1983b), Nimbus 7 CZCS: reduction of its radiometric sensitivity with time, *Appl. Opt.* 22, 3929-3930.

Herman, B. M., and Browning, S. R. (1975), The effect of aerosols on the earth-atmosphere albedo, *J. Atmos. Sci.* 32, 158-165.

Hovis, W. A., Knoll, J. S., and Smith, G. R. (1985), Aircraft measurement for calibration of an orbiting spacecraft sensor, *Appl. Opt.* 24, 407-410.

Iqbal, M. (1983) *An Introduction to Solar Radiation*, Academic Press, New York.

Jackson, R. D., Moran, M. S., Slater, P. N., and Biggar, S. F. (1987), Field calibration of reference reflectance panels. *Remote Sens. Environ.*, this issue.

Jennings, S. G. Pinnick, R. G. and Auvermann, H. J. (1978), Effects of particulate complex refractive index and particle size distribution variations on atmospheric extinction and absorption for visible through middle ir wavelengths. *Appl. Opt.* 17, 3922-3929.

Junge, C. E. (1963) Air Chemistry and Radioactivity, Academic Press, New York.

Kastner, C. J. (1985) Absolute radiometric calibration of the Landsat Thematic Mapper. PhD. dissertation, University of Arizona, 195 pp.

Kastner, C. J., and Slater, P. N. (1982), In-flight radiometric calibration of advanced remote sensing systems, *Proc. SPIE* 356, 158-165.

Kneizys, F. X., Shettle, E. P. Gallery, W. O., Chetwynd, Jr., J. H., Abreu, L. W., Selby, J. E. A., Clough, S. A., and Fenn, R. W. (1983) Atmospheric transmittance/radiance: computer code LOWTRAN 6, Report AFGL-TR-83-0187, AFCRL, Bedford, Massachusetts.

Koepke, P. (1982), Vicarious satellite calibration in the solar spectral range by means of calculated radiances and its application to Meteosat, *Appl. Opt.* 21, 2845-2854.

Markham, B. L., and Barker, J. L. (1985) editors, Landsat Image Data Quality Analysis, *Photogram. Eng. and Remote Sensing*, 51, Special LIDQA issue.

Markham, B. L., and Barker, J. L. (1986), *Remote Sensing of Environ.*, this issue.

McClatchey, R. A., Fenn, R. W., Selby, J. E. A., Volz, F. E., and Garing, J. S. (1972) Optical properties of the atmosphere, Report AFCRL-72-0497, Environmental Res. Papers, No. 411, AFCRL, Bedford, Massachusetts.

Mueller, J. L. (1985) Nimbus-7 CZCS: confirmation of its radiometric sensitivity decay through 1982. *Appl. Opt.* 24, 1043-1047.

Palmer, J. M. (1984), Effective bandwidths for Landsat-4 and Landsat D' Multispectral Scanner and Thematic Mapper subsystem, *IEEE Trans. Geosci. Remote Sensing* GE-22, 336-338.

Pearce, W. A. (1977) A study of the effects of the atmosphere on Thematic Mapper observations, Final Report under NASA contract NAS5-23639.

Robinson, B. F., Bauer, M. E., Dewitt, D. P., Silva, L. F., and Vanderbilt, V. C. (1979), Multiband radiometer for field research. *SPIE* 1968-15.

Santer, R. P. (1986), Communication to the authors.

Shaw, G. E. Reagan, J. A. and Herman, B. M. (1973) Investigation of atmospheric extinction using direct solar radiation measurements made with a multiple wavelength radiometer. *J. Appl. Met.* 12, 374.

Slater, P. N. (1984), The importance and attainment of absolute radiometric calibration, in *Proc. SPIE Critical Review of Remote Sensing* 475, 34-40.

Slater, P. N. (1985), Radiometric considerations in remote sensing, *Proc. IEEE* 73(6), 997-1011.

Slater, P. N., Biggar, S. F., Holm, R. G., Jackson, R. D., Mao, Y., Moran, M. S., Palmer, J. M., and Yuan, B. (1986) Absolute radiometric calibration of the Thematic Mapper, *SPIE* 660, in press.

Sokal, R. R., and Rohlf, F. J., (1969), *Biometry*, W. H. Freeman & Co., San Francisco.

Tanré, D., Deroo, C., Dahaut, P., Herman, M., Morcrette, J. J., Perbos, J., and Deschamps, P. Y. (1985) Effets atmospheriques en teledetection-logiciel de simulation du signal satellitaire dans le spectre solaire, Proceedings Third International Colloquium on Spectral Signatures of Objects in Remote Sensing. ESA SP-247, 315-319.

Teillet, P. M. and Fedosejevs G.,(1986), Canada Centre for Remote Sensing, Communication to the authors.

Viollier, M. (1982) Radiometric calibration of the Coastal Zone Color Scanner on Nimbus 7: a proposed adjustment. Appl. Opt. 21, 1142-1145.

Table 1. Reflectance factors for the four 16-pixel areas. A, southernmost; D, northernmost. Measurements with the MMR were taken in the east-west direction, and measurements with the Exotech were taken in the north-south direction.

August 28, 1985

Equivalent TM band from MMR

	1	2	3	4	5	7
D	0.503	0.567	0.610	0.634	0.420	0.155
C	0.503	0.565	0.607	0.627	0.421	0.159
B	0.484	0.543	0.582	0.605	0.407	0.157
A	0.479	0.539	0.580	0.599	0.408	0.163
Average	0.492	0.553	0.595	0.616	0.414	0.159

Equivalent TM band from Exotech

	1	2	3	4
D	0.507	0.577	0.616	0.649
C	0.501	0.567	0.605	0.637
B	0.487	0.548	0.585	0.616
A	0.478	0.540	0.578	0.607
Average	0.493	0.558	0.596	0.627

November 16, 1985

Equivalent TM band from MMR

	1	2	3	4	5	7
D	0.432	0.499	0.539	0.566	0.359	0.128
C	0.398	0.460	0.498	0.527	0.324	0.107
B	0.390	0.450	0.487	0.514	0.306	0.096
A	0.403	0.465	0.502	0.530	0.328	0.107
Average	0.406	0.468	0.507	0.534	0.329	0.109

Equivalent TM band from Exotech

	1	2	3	4
D	0.430	0.501	0.541	0.575
C	0.400	0.468	0.507	0.544
B	0.386	0.451	0.487	0.522
A	0.394	0.461	0.496	0.530
Average	0.402	0.470	0.508	0.543

Table 2. Reflectance factor data over gypsum sand at five solar zenith angles, measured with an Exotech radiometer over one target area.

Zenith angle	Equivalent TM band			
	1	2	3	4
73.4	0.393	0.463	0.497	0.538
63.1	0.397	0.464	0.501	0.542
55.0	0.396	0.464	0.499	0.542
47.0	0.392	0.461	0.497	0.541
45.1	0.393	0.461	0.499	0.541
34.5	0.388	0.454	0.490	0.528

Table 3. Ratios of the reflectance factors for the TM, MMR and Exotech.

TM Band	TM/MMR	TM/Exotech
1	0.9938	0.9960
2	1.0096	1.0062
3	0.9987	0.999
4	1.0035	1.008
5	1.0080	-
7	1.0053	-

Table 4. CALIBRATION OF THE THEMATIC MAPPER AT WHITE SANDS ON OCTOBER 28, 1984.

Solar zenith angle Z: 52.068
Solar distance in AU: 0.9932
Junge size distribution: 4.09
Aerosol size range: 0.02 to 5.02 um
Refractive index: 1.54 - 0.01i
Time of overpass: 10:09.1 MST
Calculated visibility: 120 km

Latitude: 32 deg 55 min
Longitude: 106 deg 22 min
Elevation: 1196 m
Pressure: 663.7 mm of Hg
Temperature: 12.4 deg C
Relative humidity: 75%
Nadir viewing angle: 5 deg.

Thematic Mapper bands	1	2	3	4	5	7
Central wavelength um	0.4863	0.5706	0.6607	0.8382	1.6770	2.2230
Tau Mie	0.1360	0.1027	0.0750	0.0401	0.0028	0.0007
Tau Rayleigh	0.1420	0.0739	0.0407	0.0156	0.0010	0.0003
Tau ozone	0.0047	0.0198	0.0098	0.0011	0.0000	0.0000
Tau water vapor	0.0000	0.0000	0.0000	0.0454	0.1241	0.0805
Tau carbon dioxide	0.0000	0.0000	0.0000	0.0000	0.0094	0.0035
Spectral reflectance	0.4380	0.5006	0.5407	0.5850	0.3592	0.1261
Eo across band in W/m2.um	1955.5	1826.9	1545.0	1042.8	220.19	74.78
Average image digital counts	222.69	117.19	140.38	119.69	102.50	26.44
Preflight cal gains	15.553	7.860	10.203	10.821	78.751	147.719
Preflight cal offsets	1.8331	1.6896	1.8850	2.2373	3.2905	3.2117
IC cal gains for 28 Oct 84	14.211	7.264	9.551	10.427	76.87	145.004
IC cal offsets for 28 Oct 84	2.2570	2.2160	2.3700	2.3640	3.1400	3.4440
Normalized code radiance	0.0805	0.0870	0.0973	0.0970	0.0491	0.0197
Code TM L in W/m2.sr.um	159.60	161.21	152.32	102.56	10.96	1.49
Spectral L from preflight cal	142.00	146.95	135.74	108.54	12.60	1.57
Spectral L from IC cal	155.11	158.28	144.50	112.52	12.93	1.59
% (Code-Pre)/Pre	12.4	9.7	12.2	-5.5	-13.0	-5.0
% (Code-IC)/IC	2.9	1.9	5.4	-8.9	-15.2	-5.8
Counts per unit radiance	1.395	0.727	0.922	1.167	9.351	17.699

****

CASE FOR RAYLEIGH ATMOSPHERE

Normalized code radiance	0.0870	0.0979	0.1055	0.1141	0.0701	0.0246
Code TM L in W/m2.sr.um	172.45	181.33	165.20	120.59	15.64	1.87
Counts per unit radiance	1.291	0.646	0.850	0.992	6.553	14.173

****

CASE FOR NO ATMOSPHERE

Normalized radiance	0.0857	0.0980	0.1058	0.1145	0.0703	0.0247
TM L in W/m2.sr.um	169.90	181.41	165.71	121.01	15.69	1.87
Counts per unit radiance	1.311	0.646	0.847	0.989	6.533	14.135

****

TABLE 5 Input Values for Radiative Transfer Calculations

Wave-Length μm	τ_{RAY}	τ_{O_3}	τ_{H_2O}	τ_{CO_2}	V=10 km τ_{MIE}	V=23 km τ_{MIE}
0.49	0.1630	0.0066	0.0	0.0	0.5393	0.2927
0.57	0.0844	0.0277	0.0	0.0	0.4665	0.2657
0.66	0.0466	0.0136	0.0	0.0	0.4089	0.2434
0.84	0.0178	0.0016	0.0335	0.0	0.3303	0.2111
1.64	0.0011	0.0	0.0915	0.0094	0.1766	0.1391
2.22	0.0004	0.0	0.0594	0.0035	0.1374	0.1176

Figure Captions

Figure 1.	The decay factor with orbit number for the first band of the CZCS (Gordon et al., 1983b).
Figure 2.	The percentage degradation in the response of the CZCS with time for the first four spectral bands (Hovis et al., 1985).
Figure 3.	Corrections for the radiometric sensitivity of the CZCS with time for the first three spectral bands (Mueller, 1985).
Figure 4.	The apparent gain change with time for the solar-reflective bands of the TM on Landsat 4. The gain values are in digital counts per mWcm^{-2}sr$^{-1}\mu$m^{-1} (Barker, 1985a).
Figure 5.	Schematic of the optical, mechanical, and electronic components of the spectropolarimeter (Castle, 1985).
Figure 6.	The layout of the 16 x 4 pixel measurement area near Chuck Site on White Sands Missile Range.
Figure 7.	The results of the TM calibration of October 28, 1984; see text.
Figure 8.	The results of TM calibrations at White Sands on five dates over the period July 1985 to November 1985.
Figure 9.	The averages of the results in Figure 8 compared with the average IC values and the preflight calibration.
Figure 10.	Percentage differences between the radiances at the top of the atmosphere and at intermediate altitudes for the White Sands conditions of October 28, 1984; see Table 4.
Figure 11.	Percentage differences between the radiances at the top of the atmosphere and at intermediate altitudes for $\rho = 0.5$ and a visibility of 10 km.
Figure 12.	Percentage differences between the radiances at the top of the atmosphere and at intermediate altitudes for $\rho = 0.5$ and a visibility of 23 km.

ORIGINAL PAGE IS
OF POOR QUALITY

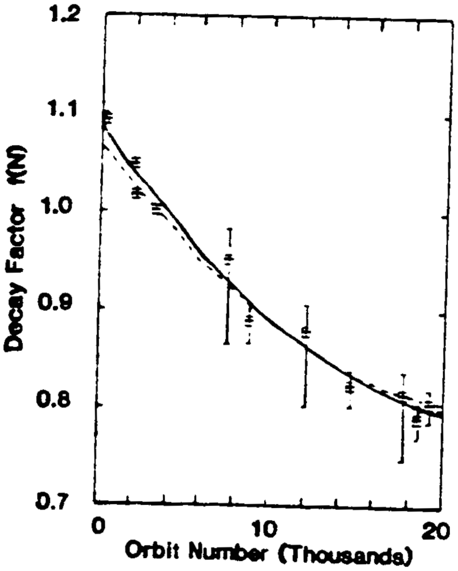

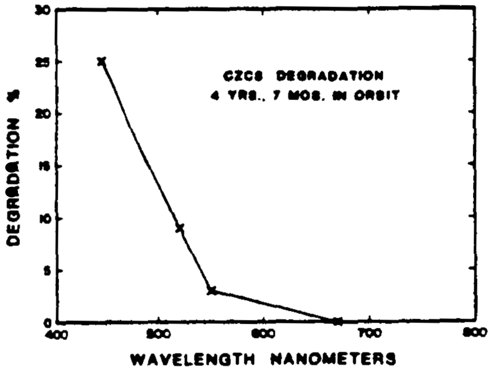
CZCS DEGRADATION
4 YRS., 7 MOS. IN ORBIT
DEGRADATION %
30
25
20
15
10
5
0
400
500
600
700
800
WAVELENGTH NANOMETERS

Fi

ORIGINAL PAGE IS
OF POOR QUALITY

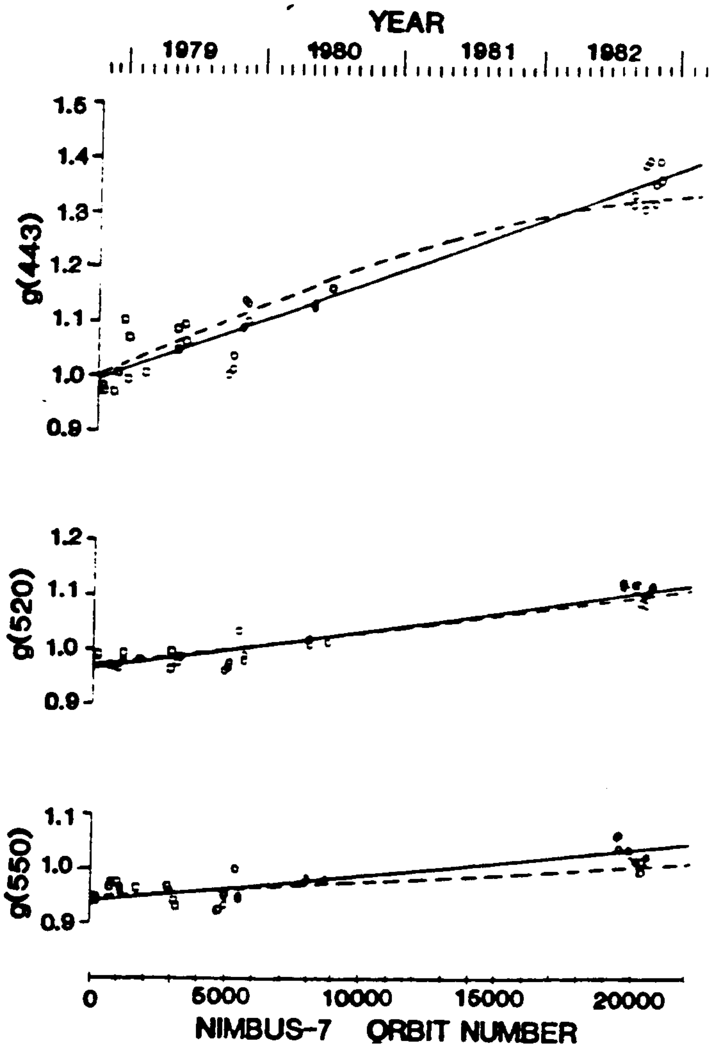

FIG 3

ORIGINAL PAGE IS
OF POOR QUALITY

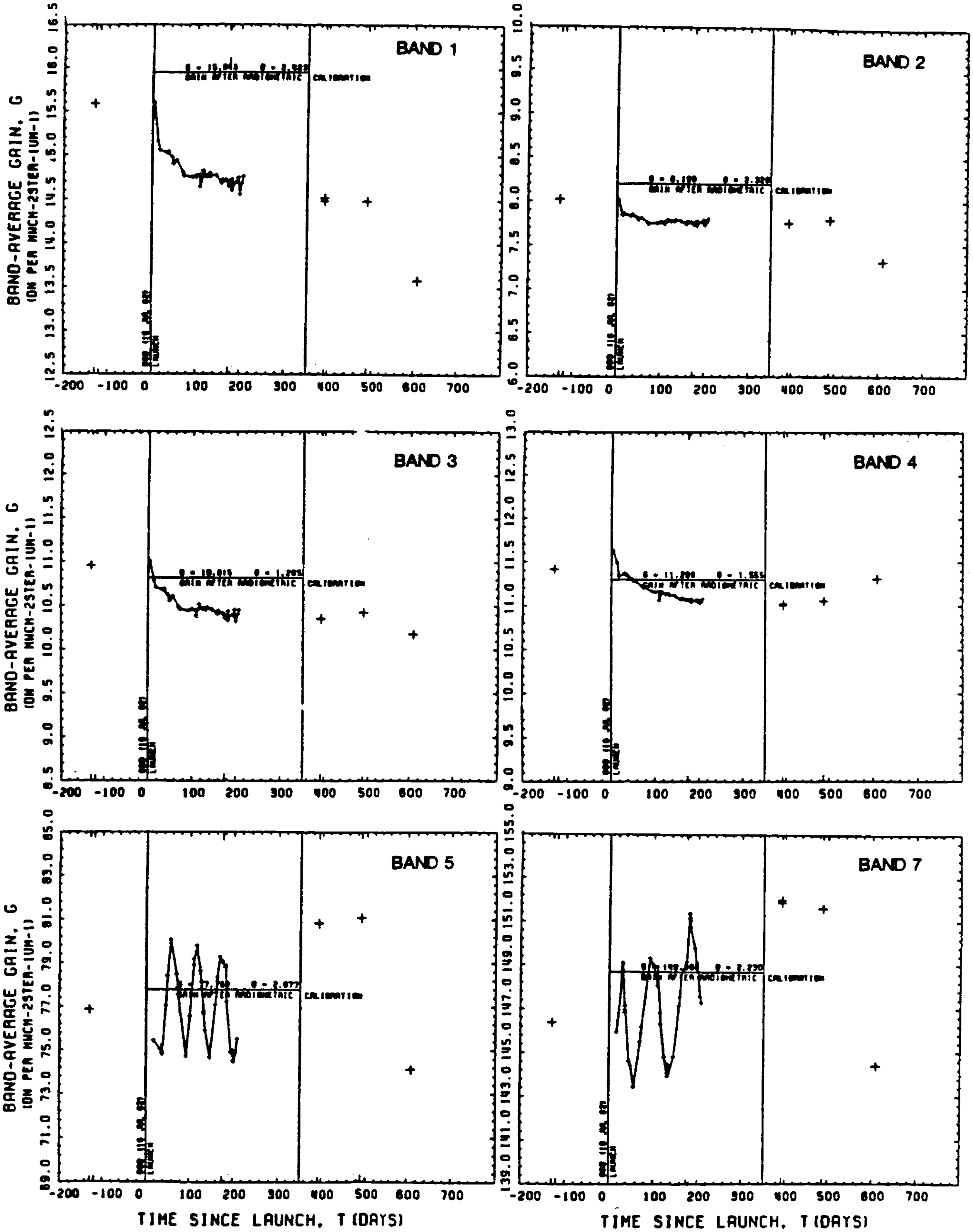

F16

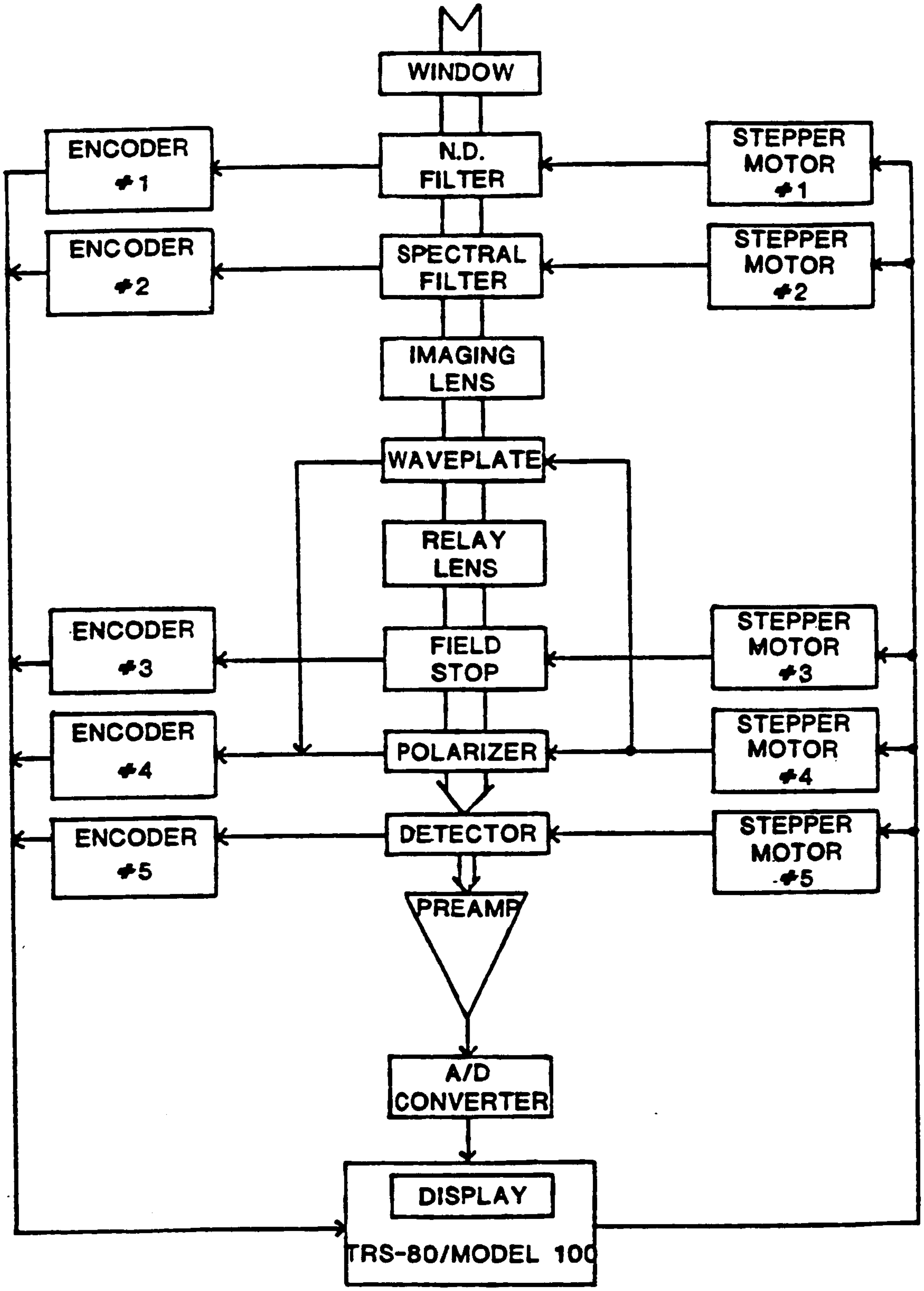
WINDOW
N.D. FILTER
SPECTRAL FILTER
IMAGING LENS
WAVEPLATE
RELAY LENS
FIELD STOP
POLARIZER
DETECTOR
PREAMP
A/D CONVERTER
DISPLAY
TRS-80/MODEL 10
ENCODER #1
ENCODER #2
ENCODER #3
ENCODER #4
ENCODER #5
STEPPER MOTOR #1
STEPPER MOTOR #2
STEPPER MOTOR #3
STEPPER MOTOR #4
STEPPER MOTOR #5

FIG 5

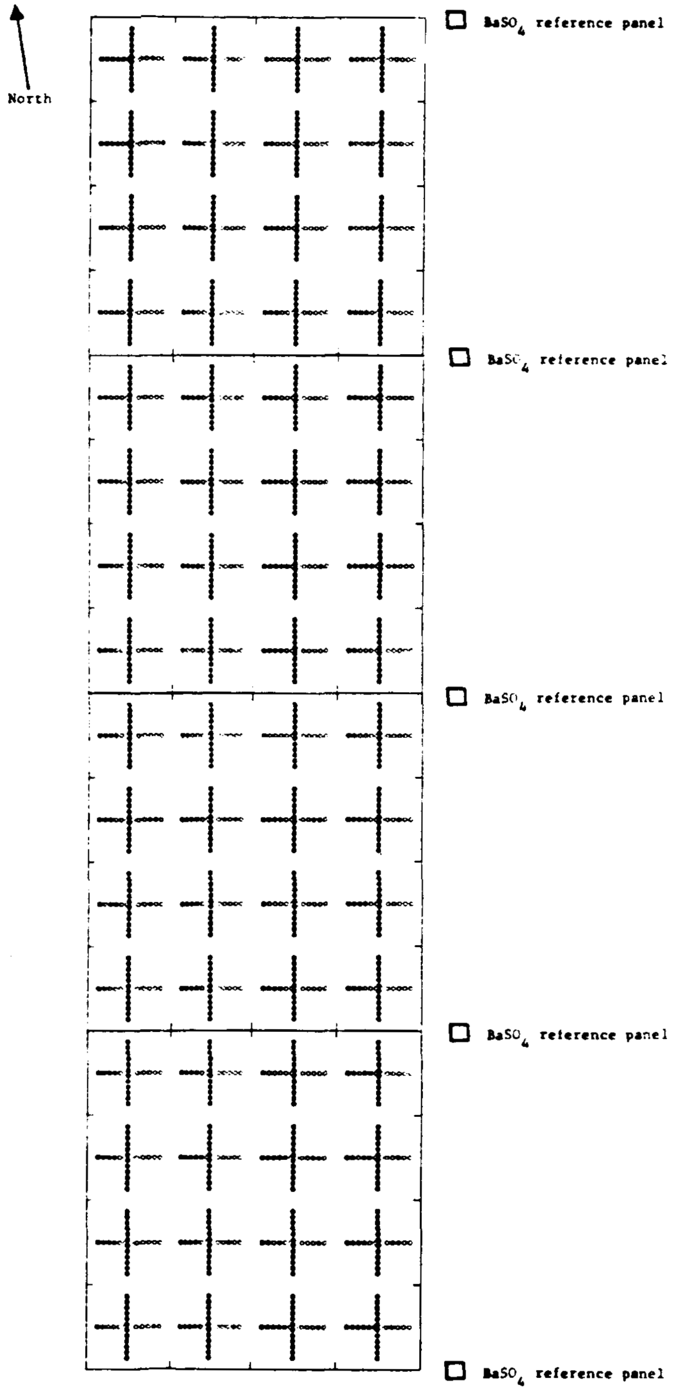
North
☐ BaSO$_4$ reference panel
☐ BaSO$_4$ reference panel
☐ BaSO$_4$ reference panel
☐ BaSO$_4$ reference panel
☐ BaSO$_4$ reference panel

Fig 6

ORIGINAL PAGE IS
OF POOR QUALITY

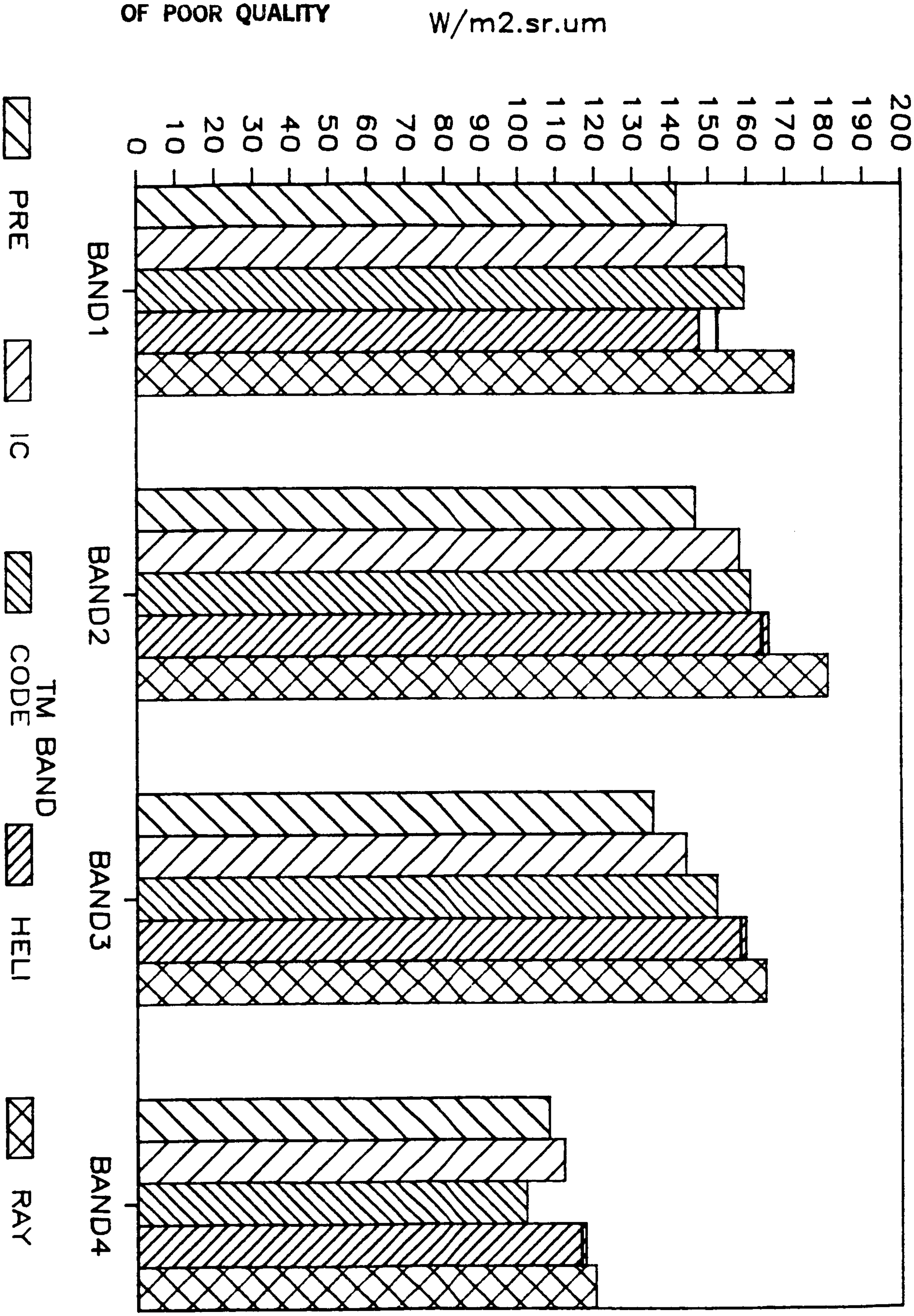

FIG 7

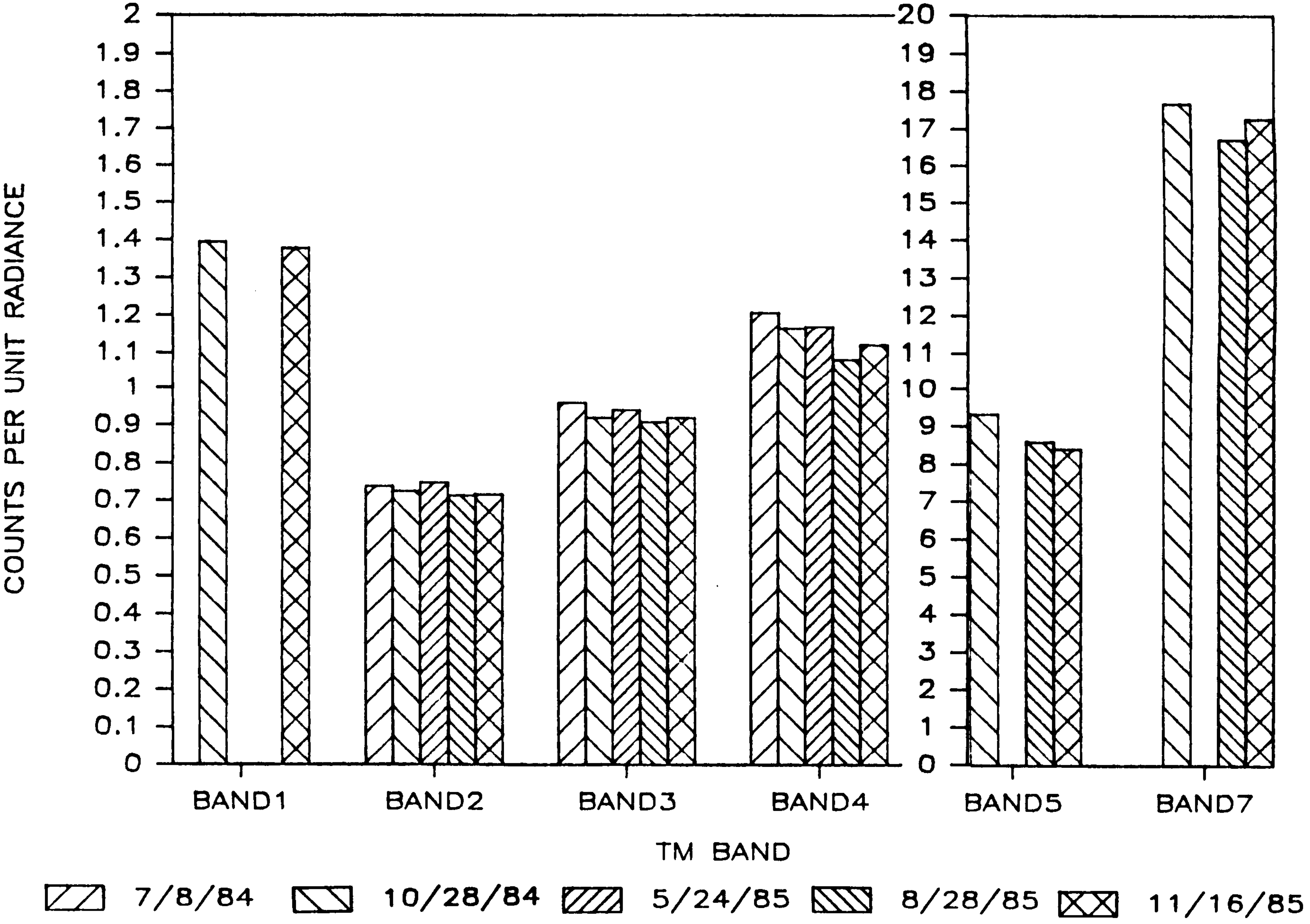
COUNTS PER UNIT RADIANCE
2
1.9
1.8
1.7
1.6
1.5
1.4
1.3
1.2
1.1
1
0.9
0.8
0.7
0.6
0.5
0.4
0.3
0.2
0.1
0
20
19
18
17
16
15
14
13
12
11
10
9
8
7
6
5
4
3
2
1
0
BAND1
BAND2
BAND3
BAND4
BAND5
BAND7
TM BAND
7/8/84
10/28/84
5/24/85
8/28/85
11/16/85

FIG 8

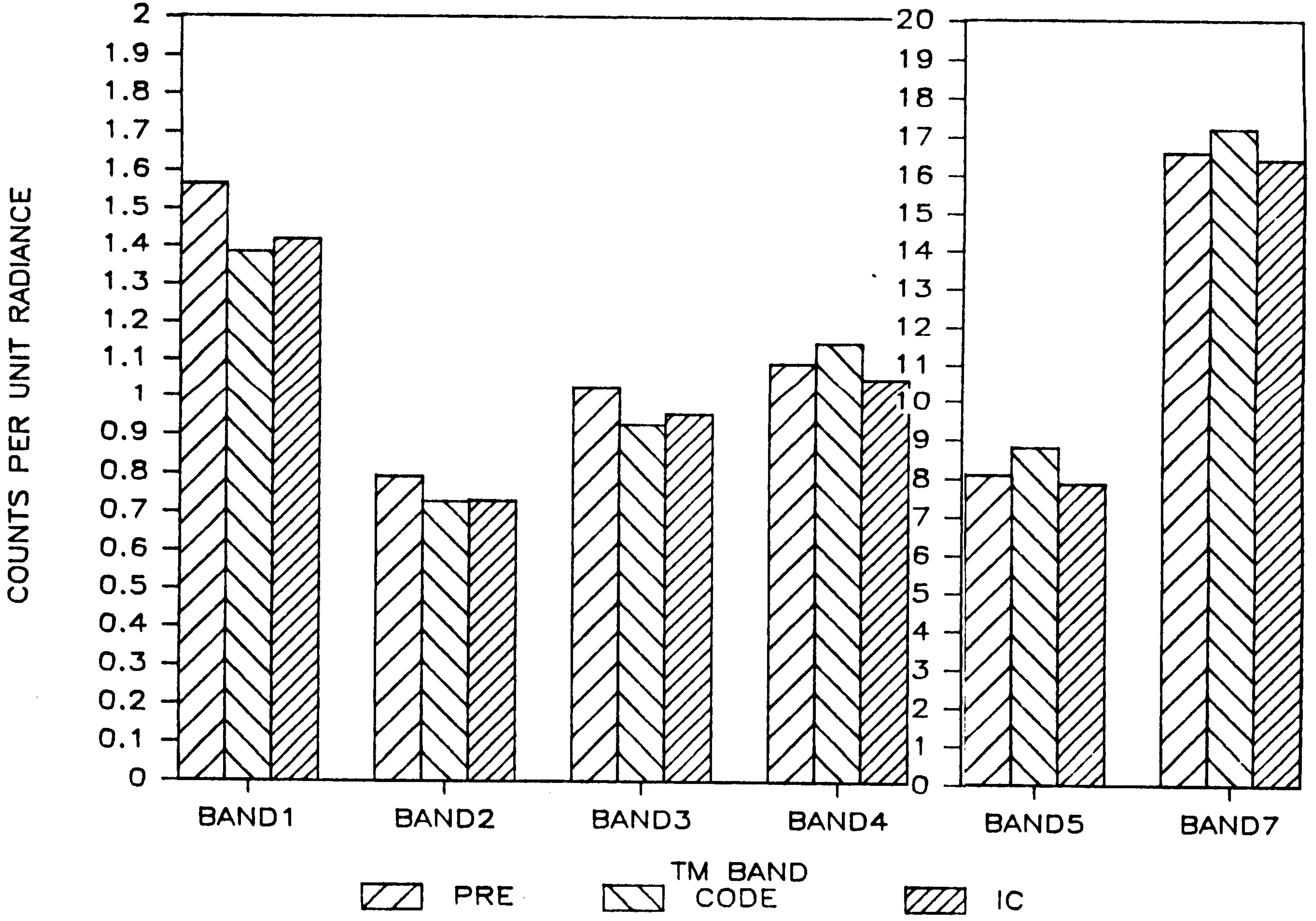
COUNTS PER UNIT RADIANCE
2
1.9
1.8
1.7
1.6
1.5
1.4
1.3
1.2
1.1
1
0.9
0.8
0.7
0.6
0.5
0.4
0.3
0.2
0.1
0
20
19
18
17
16
15
14
13
12
11
10
9
8
7
6
5
4
3
2
1
0
BAND1
BAND2
BAND3
BAND4
BAND5
BAND7
TM BAND
CODE
PRE
IC

FIG

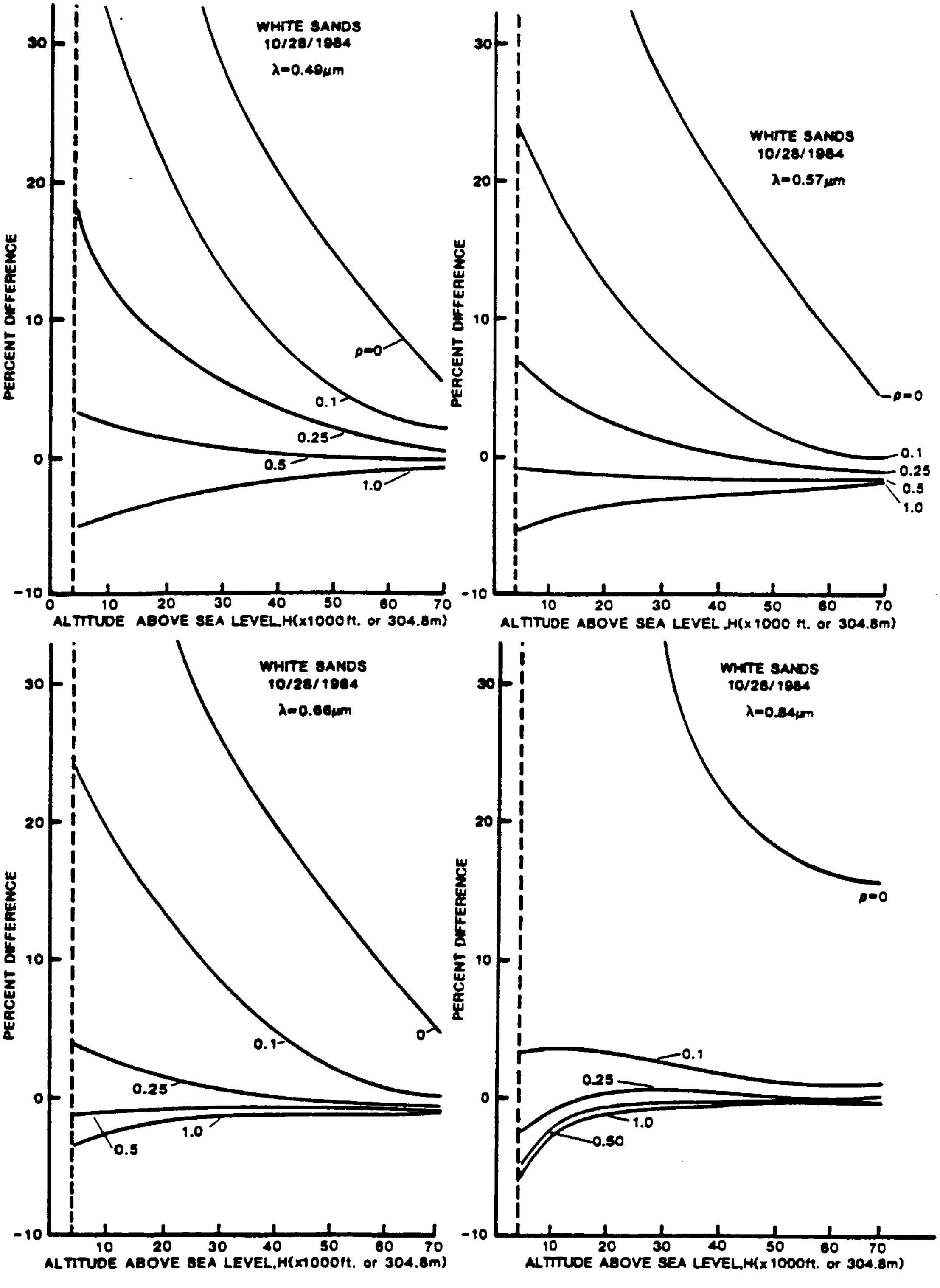WHITE SANDS
10/28/1984
λ=0.49μm
PERCENT DIFFERENCE
30
20
10
0
-10
ρ=0
0.1
0.25
0.5
1.0
0
10
20
30
40
50
60
70
ALTITUDE ABOVE SEA LEVEL,H(x1000ft. or 304.8m)
WHITE SANDS
10/28/1984
λ=0.57μm
PERCENT DIFFERENCE
ρ=0
0.1
0.25
0.5
1.0
ALTITUDE ABOVE SEA LEVEL,H(x1000 ft. or 304.8m)
WHITE SANDS
10/28/1984
λ=0.66μm
PERCENT DIFFERENCE
0
0.1
0.25
0.5
1.0
ALTITUDE ABOVE SEA LEVEL,H(x1000ft. or 304.8m)
WHITE SANDS
10/28/1984
λ=0.84μm
PERCENT DIFFERENCE
ρ=0
0.1
0.25
1.0
0.50
ALTITUDE ABOVE SEA LEVEL,H(x1000ft. or 304.8m)

FIG 1C

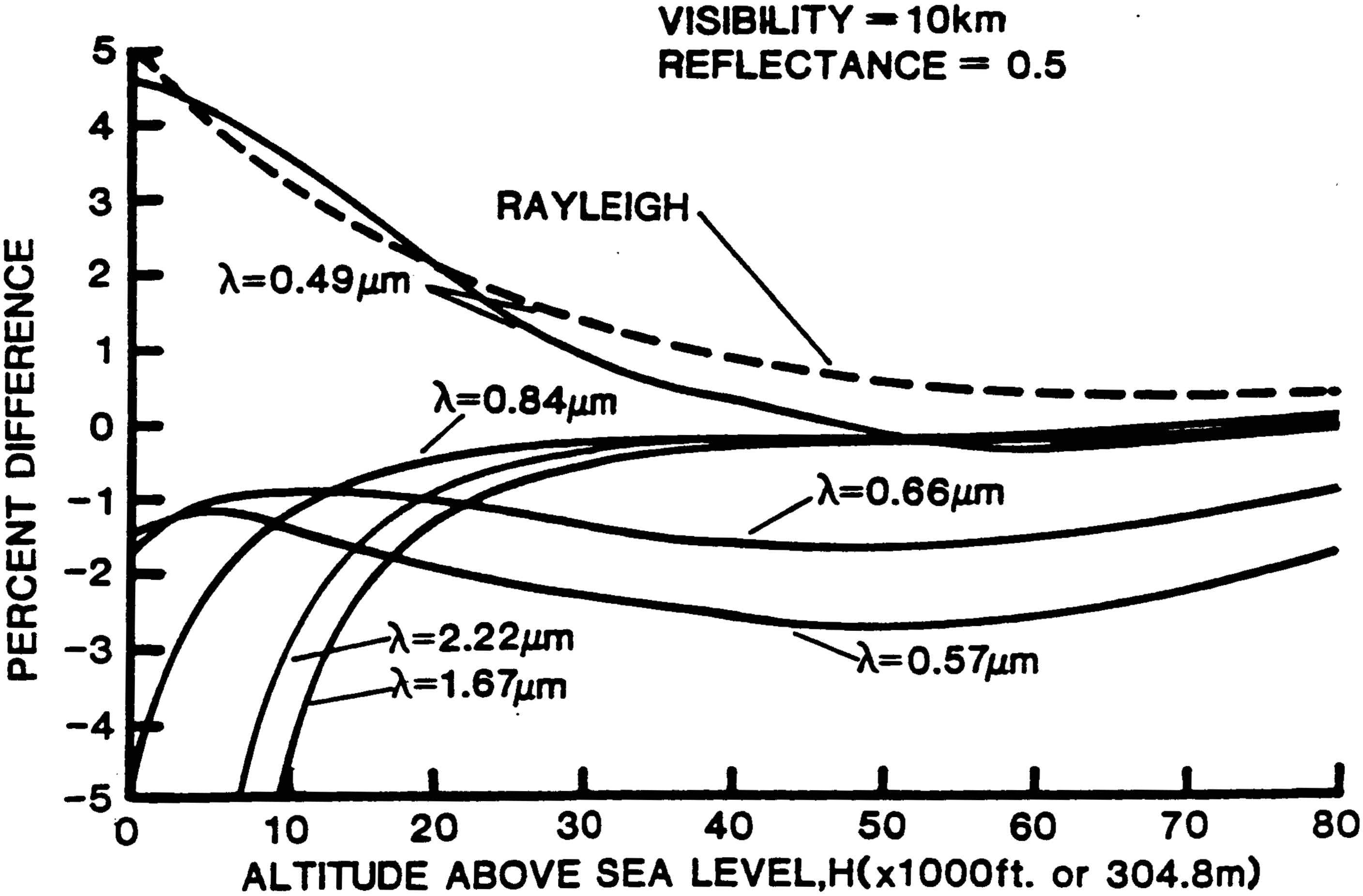

VISIBILITY = 10km
REFLECTANCE = 0.5
RAYLEIGH
λ=0.49μm
λ=0.84μm
λ=0.66μm
λ=2.22μm
λ=1.67μm
λ=0.57μm
PERCENT DIFFERENCE
5
4
3
2
1
0
−1
−2
−3
−4
−5
0
10
20
30
40
50
60
70
80
ALTITUDE ABOVE SEA LEVEL,H(x1000ft. or 304.8m)

FIG 1

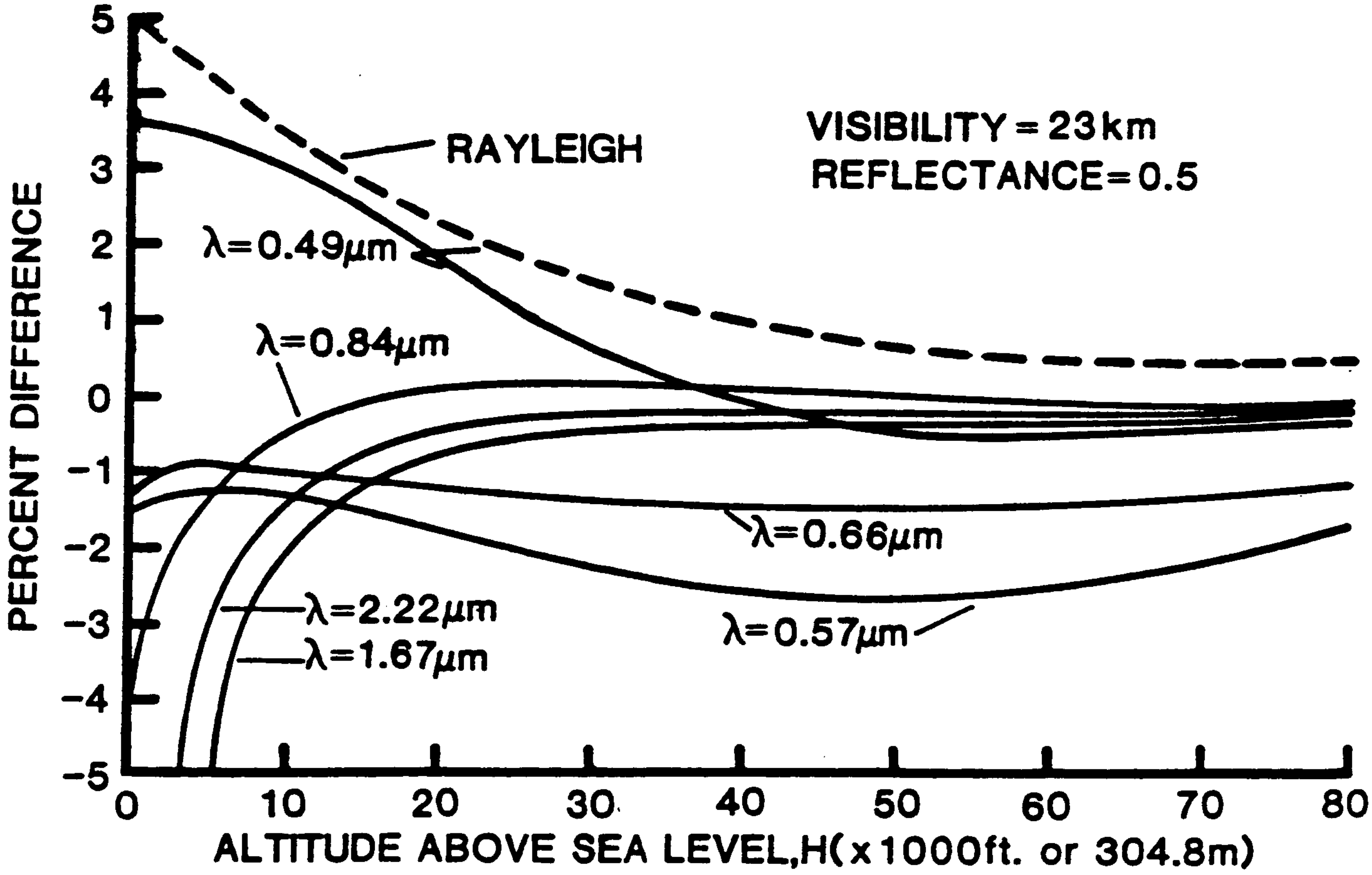

VISIBILITY = 23km
REFLECTANCE = 0.5
RAYLEIGH
λ=0.49μm
λ=0.84μm
λ=0.66μm
λ=2.22μm
λ=1.67μm
λ=0.57μm
PERCENT DIFFERENCE
5
4
3
2
1
0
−1
−2
−3
−4
−5
0
10
20
30
40
50
60
70
80
ALTITUDE ABOVE SEA LEVEL,H(x1000ft. or 304.8m)

FIG 12

SECTION IV

THEORY, METHODOLOGY AND SENSITIVITY ANALYSIS OF CALIBRATION PROCEDURE

CHAPTER 3

RADIATIVE TRANSFER THROUGH THE ATMOSPHERE

In this chapter the numeric solution to the transfer of visible and near infrared energy within the atmosphere is discussed. Models of the atmosphere are included. Particular emphasis is given to Rayleigh and Mie theories of scattering as well as absorption due to atmospheric ozone and water.

The fundamental theory of radiative transfer was developed by Chandrasekhar (1950). He was first to formalize the problem of radiative transfer in a solar-illuminated plane-parallel atmosphere and to present a solution in the form of a set of nonlinear equations. He accounted for polarization by adopting the four Stokes parameters to characterize the field. However, even with this framework, these equations remained unsolved for several years. This can be attributed to the fact that the radiance at a given altitude within the atmosphere and directed in a given direction is expressed in terms of the radiances incoming from all directions, at that altitude. In practice, the closed-form solution, expressing the field in terms of known boundary values, cannot be written. The number of equations involved would be overwhelming. Approximations (that is, assuming single scattering) are often made. This is acceptable if high accuracy is not a criterion. The LOWTRAN 6 code (Kneizys et al., 1983), developed by the Air Force Geophysics Laboratory, is one such approximate code.

The software required to solve the Chandrasekhar equations was developed, using the Gauss-Seidel iterative technique, by Herman [Herman (1963), Herman and Browning (1965), Herman, Browning, and Curran (1971)]. In his method an initial guess is made of the field present after propagation through one atmospheric layer. A solution for successive layers is made using quantities that have been calculated in the previous layer. At the ground a reflectance model, usually Lambertian, is used to compute the upwelling radiance. Radiances are then traced moving back up to the top of the atmosphere. Once the radiances at all atmospheric levels have been solved, the process is repeated using updated values of the assumed radiances. All unknowns are changed from their previously calculated values, as the values of the initial unknowns are changed. After several iterations the unknowns converge to a unique solution. This solution is exact in the sense that all orders of multiple scattering are accounted for. Computational accuracy is thought to be limited only by the atmospheric models and input parameters required to run the code.

We use this radiative transfer program in the absolute radiometric calibration of Landsat's Thematic Mapper. In the following, it is referred to as the Herman code.

The Equation of Transfer

The attenuation of radiation through some distance ds can be described by the equation

$$dL_\lambda = -k_{T\lambda}\, \rho\, L_\lambda\, ds \,. \tag{3.1}$$

Here $k_{T\lambda}$ is the total mass extinction coefficient (in units of area per mass, such as cm^2g^{-1}), ρ is the density of the medium (mass/volume, or g cm^{-3}), and L is the radiance (W $cm^{-2}sr^{-1}\mu m^{-1}$) at point s within the medium. The distance ds is a positive quantity, irrespective of coordinate system. Owing to this attenuation, and owing to scattering into the beam, radiance varies with distance s. Extinction and density may also vary spatially. In addition, the radiance and mass extinction coefficient vary with wavelength. It is common to identify spectral concentrations with a subscript λ (such as L_λ) and spectral functions as (λ). To simplify, these notations are omitted, but the spectral nature is still implied.

The mass extinction coefficient is composed of a scattering term, k_s, and an absorption term, k_a. Thus,

$$k_T = k_s + k_a \ . \tag{3.2}$$

A related parameter is the volume extinction coefficient, $\beta_T = \rho\ k_T$, which has units of inverse length. Usually one prefers to describe the variation of extinction within the atmosphere in terms of the particle or molecular density. Thus, the radiative transfer equations most often use the mass extinction coefficient rather than the volume extinction coefficient. The former is usually assumed constant throughout the atmosphere. It will vary spatially with altitude only if effects such as pressure broadening, variations of aerosol refractive index, or variations in aerosol radial size distribution occur. Conversely, the parameter β_T varies dramatically with altitude owing to its proportionality to density.

To describe the distribution of radiance, normalized to the incoming irradiance, that is scattered from a beam, the phase function $P(\theta)$ is introduced. Here θ is the angle between the incident and scattered beams. Equivalently, $P(\theta,\phi;\theta',\phi')$ describes that radiance scattered from a differential solid angle $d\omega$ centered about (θ,ϕ) into a differential solid angle $d\omega'$ about (θ',ϕ'). In this chapter, the first angles within parentheses are those of the incident beam; the angles that follow the semicolon are those of the scattered beam. When $P(\theta)$ is used within an integrand, the integration is with respect to the primed angles. For example, by integrating the phase function over all outgoing angles $d\omega'$, the total energy lost from a beam through scattering can be computed. This is given by

$$\begin{aligned} \Delta L_s(\theta,\phi) &= -k_s \, \rho \, L(\theta,\phi) \, ds \\ &= -k_T \, \rho \, ds \int_0^{2\pi}\!\!\int_0^{\pi} P(\theta,\phi;\theta',\phi') \, L(\theta,\phi) \, \sin\theta' \, d\theta' \, d\phi'. \end{aligned} \tag{3.3}$$

$L(\theta,\phi)$ is not a function of the scattered angles, and may be placed outside the integral. Using the above equality, the identity

$$\int_0^{2\pi}\!\!\int_0^{\pi} P(\theta,\phi;\theta',\phi') \, \sin\theta' \, d\theta' \, d\phi' \equiv \frac{k_s}{k_T} \tag{3.4}$$

is made. The ratio k_s/k_T is known as the single scattering albedo. It is that fraction of the total attenuation due to scattering for a single collision, and is equal to the integral of the phase function over the scattered angles. A conservative scattering atmosphere is one in which the single scatter albedo is unity.

The energy balance equation, which summarizes the sources and sinks acting on a beam, can be written

$$
\begin{aligned}
dL(\theta,\phi) &= k_T\, \rho\, ds \int_{4\pi} P(\theta',\phi';\theta,\phi)\, L(\theta',\phi')\, d\omega' \\
&\quad + k_T\, \rho\, ds\, P(\theta_0,\phi_0;\theta,\phi)\, E + e\rho\, ds \\
&\quad - k_T\, \rho\, L(\theta,\phi)\, ds \, .
\end{aligned}
\tag{3.5}
$$

The first term is the energy scattered into $d\omega$ due to incoming fields from all directions $d\omega'$, where $d\omega' = \sin\theta'\, d\theta'\, d\phi'$. Note how this integral over the phase function differs from before. The energy into $L(\theta,\phi)$ from all incoming $L(\theta',\phi')$ is computed here, as opposed to the energy out of $L(\theta,\phi)$, as in Eq. (3.3). The second term accounts for single scattering out of the solar beam. The incident solar beam has an irradiance E at distance s and propagates along (θ_0,ϕ_0) where $\theta_0 >$ 90°, $\theta_0 = \theta_z + 90°$, and θ_z is the solar zenith angle. The third term accounts for emission within the atmosphere. The spectral parameter e_λ (here denoted only as e) is the emitted spectral radiant flux propagating in an infinitesimal cone containing that direction of propagation, divided by the solid angle of the cone, and normalized with respect to the density of the medium. The final term is the energy lost due to scattering and absorption processes.

The sources can be readily grouped together by introducing the source function

$$J(\theta,\phi) = \int_{4\pi} P(\theta',\phi';\theta,\phi)\, L(\theta',\phi')\, d\omega' + P_o(\theta_o,\phi_o;\theta,\phi)\, E + e/k_T \, . \tag{3.6}$$

This is the radiance added to the incident beam per unit $k_T \rho\, ds$. Throughout the visible and near infrared regions of the spectrum, emission is considered to be negligible. For our application, therefore, the source function will have contributions only from scattering. After dividing both sides by $(-k_T \rho\, ds)$ and introducing the source function, Eq. (3.5) becomes

$$\frac{dL(\theta,\phi)}{-k_T \rho\, ds} = L(\theta,\phi) - J(\theta,\phi) \, . \tag{3.7}$$

The derivative with respect to s is now expanded in terms of derivatives with respect to the x, y, and z axes. Here a Cartesian coordinate system is defined such that the z axis is directed upward and the x axis is directed such that the sun falls within the x-z plane. In addition, the zenith angle θ is defined with respect to an outward normal directed along the z axis. A beam propagating along $\theta = 0°$ is propagating out toward space; a beam directed into the sun will have an azimuth angle of $\phi = 0°$. This coordinate system is depicted in Fig. 3.1.

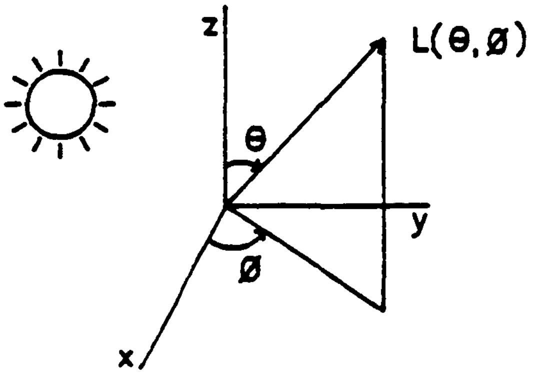

Figure 3.1 Coordinate system used to represent beam directionality.

Two assumptions are placed on the atmosphere to be modeled. The atmosphere is assumed to be (a) in steady state (no variations with time) and (b) horizontally homogeneous, which implies a flat earth. (As the following equations use the steady-state assumption, they cannot be used to describe the propagation of a pulsed lidar beam. Here significant changes occur within the atmosphere as the beam travels.) These assumptions imply that there will be no variations in the field or source function along a horizontal plane, and there will be no variations with time. Thus if the generalized function f here represents either L or J, the derivatives df/dx, df/dy, and df/dt will be zero and $df/ds = (df/dz)(dz/ds) = (df/dz)\cos\theta$.

A few definitions may be conveniently introduced here. First, let $\mu \equiv |\cos\theta|$. With the sun at a solar zenith angle of θ_z, rays propagating downward from the sun are associated with $-\mu_0 = |\cos(\theta_z+90°)|$. While μ itself is always positive, the angle −μ will be associated with downward propagating beams and μ will be associated with upward directed beams. Second, let the optical depth at any height z within the atmosphere be defined as

$$\tau(z) \equiv \int_z^\infty k\ \rho\ dz\ . \qquad (3.8)$$

The optical depth between two altitudes is given as

$$\begin{aligned} \Delta\tau(z_1,z_2) &= \int_{z_1}^{z_2} k\ \rho\ dz \\ &= \tau(z_1) - \tau(z_2)\ . \qquad (3.9) \end{aligned}$$

As τ is a positive quantity that monotonically decreases with increasing altitude z, the integration within Eq. (3.9) will always be set up such that $z_2 > z_1$, and hence $\Delta\tau(z_1,z_2)$ will be positive. If z is at ground elevation and $k = k_T$, then the optical depth defined by Eq. (3.8) is equal to τ_{ext}. This is the extinction optical thickness, or total optical depth of the atmosphere.

The attenuation of radiance can now be written in terms of optical depth

$$dL(\theta,\phi) = -k_T\ \rho\ L(\theta,\phi)\ dz/\cos\theta = d\tau\ L(\theta,\phi)/\cos\theta\ . \qquad (3.10)$$

Here the substitutions $ds = dz/\cos\theta$ and $d\tau = -k_T\ \rho\ dz$ (τ decreases with increasing z) have been made within Eq. (3.1). Note that $ds = dz/\cos\theta$ is again a positive quantity. For downward directed beams both dz and $\cos\theta$ are negative; for upward directed beams both are positive. This is necessary to assure that dL, as given by Eq. (3.10), is always negative. (The beam is attenuated by this term.) Two separate equations are, however, required to express ds as a function of μ, as μ in itself carries no sign. For downward directed beams, $ds = -dz/\mu$, while for upward directed beams $ds = dz/\mu$.

The energy balance equation, Eq. (3.7), may likewise be rewritten:

Downward propagation

$$-\mu \; dL(\tau,-\mu,\phi)/d\tau = L(\tau,-\mu,\phi) - J(\tau,-\mu,\phi) \tag{3.11a}$$

Upward propagation

$$\mu \; dL(\tau,\mu,\phi)/d\tau = L(\tau,\mu,\phi) - J(\tau,\mu,\phi) \; . \tag{3.11b}$$

For the time being it will be convenient to write separate equations for downward and upward directed beams. Note that the radiance and source terms are a function of both altitude z (hence a function of τ) and direction (μ,ϕ). The parameters within parentheses serve as a reminder of this dependence. The equation is a linear, nonhomogeneous, first-order differential equation, subject to the following boundary value conditions: the diffuse radiance incident at the top of the atmosphere is zero, there are no contributions to radiance from below the earth's surface, and the exoatmospheric solar irradiance is known. That is,

$$\begin{aligned} L(0,-\mu,\phi) &= 0 \\ L(>\tau_{ext},\mu,\phi) &= 0 \\ E_0(-\mu_0,\phi_0) &= \text{known} \end{aligned} \tag{3.12}$$

The parameter τ_{ext} is the total optical depth at the earth's surface.

Multiplying both sides of Eq. (3.11a) by $\exp(\tau/\mu)$ and both sides of Eq. (3.11b) by $\exp(-\tau/\mu)$, we obtain

For downward propagation

$$-\mu\, e^{\tau/\mu} \frac{dL(\tau,-\mu,\phi)}{d\tau} - L(\tau,-\mu,\phi)\, e^{\tau/\mu} = -\mu \frac{d(L\, e^{\tau/\mu})}{d\tau}$$
$$= -J(\tau,-\mu,\phi)\, e^{\tau/\mu} \qquad (3.13a)$$

For upward propagation

$$\mu\, e^{-\tau/\mu} \frac{dL(\tau,\mu,\phi)}{d\tau} - L(\tau,\mu,\phi)\, e^{-\tau/\mu} = \mu \frac{d(L\, e^{-\tau/\mu})}{d\tau}$$
$$= -J(\tau,\mu,\phi)\, e^{-\tau/\mu} \qquad (3.13b)$$

Consider a ray as it traverses the layer structure shown in Fig. 3.2. The top of a layer is denoted by τ_n and the bottom by τ_{n+1}. These layers are also denoted by τ_i (initial) and τ_f (final), where τ_i can be either τ_n or τ_{n+1}, depending on the direction of propagation. Intermediate altitudes are identified by some τ'.

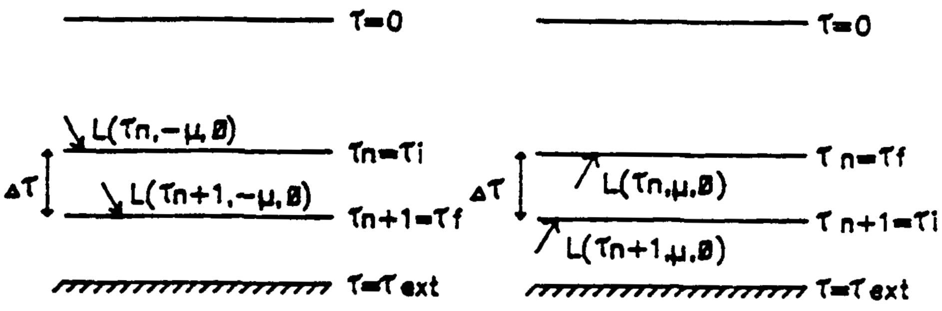

Figure 3.2 Layer nomenclature for beams propagating through the atmosphere.

The radiance after propagation is determined by integrating Eq. (3.13) between the initial and final τ values. Thus,

Downward

$$-\mu\left[L(\tau_{n+1},-\mu,\phi)\ e^{\tau_{n+1}/\mu} - L(\tau_n,-\mu,\phi)\ e^{\tau_n/\mu}\right]$$

$$= -\int_{\tau_n}^{\tau_{n+1}} J(\tau',-\mu,\phi)\ e^{\tau'/\mu}\ d\tau' \qquad (3.14a)$$

Upward

$$\mu\left[L(\tau_n,\mu,\phi)\ e^{-\tau_n/\mu} - L(\tau_{n+1},\mu,\phi)\ e^{-\tau_{n+1}/\mu}\right]$$

$$= -\int_{\tau_{n+1}}^{\tau_n} J(\tau',\mu,\phi)\ e^{-\tau'/\mu}\ d\tau' \ . \qquad (3.14b)$$

Dividing Eq. (3.14a) by $(-\mu\ \exp(\tau_{n+1}/\mu))$ and Eq. (3.14b) by $(\mu\ \exp(-\tau_n/\mu))$, we can rewrite the above as:

Downward

$$L(\tau_{n+1},-\mu,\phi) = L(\tau_n,-\mu,\phi)\ e^{-(\tau_{n+1}-\tau_n)/\mu}$$

$$+ \int_{\tau_n}^{\tau_{n+1}} J(\tau',\mu,\phi)\ e^{-(\tau_{n+1}-\tau')/\mu}\ \frac{d\tau'}{\mu} \qquad (3.15a)$$

Upward

$$L(\tau_n,\mu,\phi) = L(\tau_{n+1},\mu,\phi)\ e^{-(\tau_{n+1}-\tau_n)/\mu}$$

$$+ \int_{\tau_n}^{\tau_{n+1}} J(\tau',\mu,\phi)\ e^{-(\tau'-\tau_n)/\mu}\ \frac{d\tau'}{\mu} \ . \qquad (3.15b)$$

These equations can be combined if τ_i and τ_f are introduced:

$$L(\tau_f,\pm\mu,\phi) = L(\tau_i,\pm\mu,\phi)\, e^{-\Delta\tau/\mu} + \int_{\tau_n}^{\tau_{n+1}} J(\tau',\pm\mu,\phi)\, e^{-\Delta\tau'/\mu}\, d\tau'/\mu \tag{3.16a}$$

where

$$J(\tau',\pm\mu,\phi) = \int_{4\pi} P(\mu',\phi';\pm\mu,\phi)\, L(\mu',\phi')\, d(-\mu')\, d\phi + P(\mu_0,\phi_0;\theta,\phi)\, E\ . \tag{3.16b}$$

Here $\Delta\tau = \tau_{n+1}-\tau_n$ and $\Delta\tau' = |\tau'-\tau_f|$. The solid angle $d\omega' = \sin\theta'\, d\theta'\, d\phi' = d(-\cos\theta')d\phi'$ has been written in terms of μ, or $d\omega' = d(-\mu')\, d\phi'$. Each of the above equations states that the radiance after passing through a layer can be expressed as the initial radiance attenuated by $\exp(-\Delta\tau/\mu)$, plus a contribution from the source function. The source function adds a contribution at each altitude τ' but is attenuated owing to the $\Delta\tau'$ between τ' and the final layer.

Numeric Solution

To evaluate the above radiative transfer equation, the integrals within Eqs. (3.16a) and (3.16b) are replaced with an equivalent sum of integrals with smaller differences between the limits of integration. The new limits are defined such that the parameters J, P, and L can be approximated as constants within the $\Delta\tau$, $\Delta\theta$, and $\Delta\phi$ intervals. They are put outside the integrals, an evaluation is made, and a solution is obtained.

In evaluating the integral over optical depth, Eq. (3.16a), the radiative transfer through a double layer (between layers τ_n and τ_{n+2})

is considered. This allows the average value of the source term to be taken as that at the midpoint of the interval, namely at τ_{n+1}. After this constant value is factored out and $J(\tau_{n+1},\pm\mu,\phi)\int_{\tau_n}^{\tau_{n+2}} e^{-\Delta\tau'/\mu}\,\frac{d\tau'}{\mu}$ is evaluated, Eq. (3.16a) becomes

$$\begin{aligned} L(\tau_f,\pm\mu,\phi) &= L(\tau_i,\pm\mu,\phi)\, e^{-2\Delta\tau/\mu} \\ &\qquad + J(\tau_{n+1},\pm\mu,\phi)\,(1 - e^{-2\Delta\tau/\mu}) \ , \end{aligned} \tag{3.17}$$

where the interval $\Delta\tau$ is still defined as that between τ_n and τ_{n+1}, and τ_f and τ_i are separated by a $2\Delta\tau$ thickness.

In turn, $J(\tau_{n+1},\pm\mu,\phi)$ is evaluated by replacing the integrals within Eq. (3.16b) with sums over the finite differences $\Delta\mu$ and $\Delta\phi$. That is,

$$\begin{aligned} &J(\tau_{n+1},\pm\mu,\phi) \\ &= \sum_{k=1}^{2\pi/\Delta\phi} \left[\sum_{j=1}^{1/\Delta\mu} P(\mu'_j,\phi'_k;\pm\mu,\phi)\, L(\tau_{n+1},\mu'_j,\phi'_k)\, (-\Delta\mu')_j \right] (\Delta\phi')_k \ . \end{aligned} \tag{3.18}$$

As an example, let $\Delta\theta = 10°$ and $\Delta\phi = 30°$. Then,

$$j = 1,\ldots,18 \tag{3.19a}$$

$$\theta'_j = j\Delta\theta - \Delta\theta/2 = [5°,\ 15°,\ \ldots,\ 175°]$$

$$\mu'_j = \cos\theta'_j$$

$$\begin{aligned} (-\Delta\mu')_j &= \cos[(j-1)\Delta\theta] - \cos(j\Delta\theta) \\ &= [\cos 0° - \cos 10°,\ \ldots,\ \cos 170° - \cos 180°] \end{aligned}$$

$$k = 1,\ldots,12 \qquad (3.19b)$$

$$\phi'_k = k\Delta\phi - \Delta\phi/2 = [15°, 45°, \ldots, 345°]$$

$$(\Delta\phi')_k = \Delta\phi = 30° * \pi \text{ rad}/180°$$

Note that P and L have been taken out of the integral over the finite limits $\Delta\theta$ and $\Delta\phi$ and replaced with their values at the midpoints of these finite differences.

At the beginning of each iteration through the atmosphere, the radiances at level τ_1 are required. This is achieved by considering the transfer of radiation through only a single $\Delta\tau$ layer,

$$L(\tau_1,-\mu,\phi) = (1-e^{-\Delta\tau/\mu}) \left[\sum_{k=1}^{2\pi/\Delta\phi} \sum_{j=1}^{1/\Delta\mu} P(\mu'_j,\phi'_k;-\mu,\phi) \right.$$
$$\left. * \; L(0,\mu'_j,\phi'_k)\,(-\Delta\mu')_j\,\Delta\phi + P(-\mu_0,\phi_0;-\mu,\phi)\,E_0 \right] . \qquad (3.20)$$

On the first pass, all upwelling radiances $L(0,\mu'_j,\phi'_k)$, or that energy being reflected out of the atmosphere and into space, are assumed zero. On successive passes, those values computed in previous iterations are assumed. At all times the downwelling radiances $L(0,\mu'_j,\phi'_k)$, at the top of the atmosphere, are assumed zero. This means that the only energy entering the atmosphere is from the solar irradiance E_0. At the bottom of the atmosphere the upwelling radiances are computed by multiplying the sum of the diffuse and direct downwelling irradiances by ρ/π. This assumes Lambertian surface characteristics.

In choosing a numeric value for the layer thickness $\Delta\tau$, Herman (1963) used a statistical analysis to compute the probability that scattering within a layer would be due to single scattering alone. The $\Delta\tau$ interval must be small enough to neglect variations of the source term, which is equivalent to requiring that L and E remain approximately constant over the interval. This is likely if a photon has a small probability of undergoing more than one scattering event. Conversely, $\Delta\tau$ must not be so small as to make the computation time excessive. A value of $\Delta\tau = 0.02$ was chosen. Here, approximately 96% of the scattered radiation is associated with a single collision. Since the effective depth of the atmosphere is ($\Delta\tau$ μ), a greater percentage of multiple scattering occurs at larger zenith angles. As θ approaches 90°, this error builds up rapidly. Calculations down to 85° can be made without introducing any serious errors.

Polarization

Although the Herman code that we have used does not account for changes in polarization as a ray propagates through the atmosphere, it can be modified to do so. However, preliminary studies indicate that the original code is accurate enough for our calibration work, given the atmospheric conditions we have encountered at White Sands to date. For this reason the studies within this dissertation were made using the original Herman code, which is both easier and faster to run. For completeness, the theory behind the polarization code is discussed here.

To be as accurate as possible, the radiative transfer equation must describe the state of polarization of a scattered field, as this field generally has undergone a change in polarization compared to that of the incident field. To describe this state, the amplitude of the electric field components along two orthogonal directions and the phase difference between these components are required. For example, let A_ℓ and A_r be the paralle$\underline{l}$ and perpendicula$\underline{r}$ field components, defined with respect to a reference plane. This reference plane is chosen as that containing the incident and scattered beams. Then,

$$\begin{aligned} A_\ell &= a_\ell \exp(-i\delta_\ell) \exp[i(\omega t-kz)] \\ A_r &= a_r \exp(-i\delta_r) \exp[i(\omega t-kz)] \\ \delta &= \delta_\ell - \delta_r \end{aligned} \tag{3.21}$$

As an alternative to requiring that the amplitudes a_ℓ and a_r and the phase difference δ be known, the state of polarization may be represented by the four Stokes parameters introduced by Sir George Stokes in 1852. These have the advantage of all having the same dimension, that of an irradiance. The four parameters are

$$\begin{aligned} E_\ell &= A_\ell A_\ell^* = a_\ell^2 \\ E_r &= A_r A_r^* = a_r^2 \\ U &= 2\,\mathrm{Re}(A_\ell A_r^*) = 2\,a_\ell a_r \cos\delta \\ V &= 2\,\mathrm{Im}(A_\ell A_r^*) = 2\,a_\ell a_r \sin\delta \end{aligned} \tag{3.22}$$

where the asterisk denotes that the complex conjugate has been taken.

The state of polarization can be represented by an ellipse, which in turn is described by the Stokes parameters (Fig. 3.3). Let χ be the angle between the direction of the major axis and the ℓ direc-

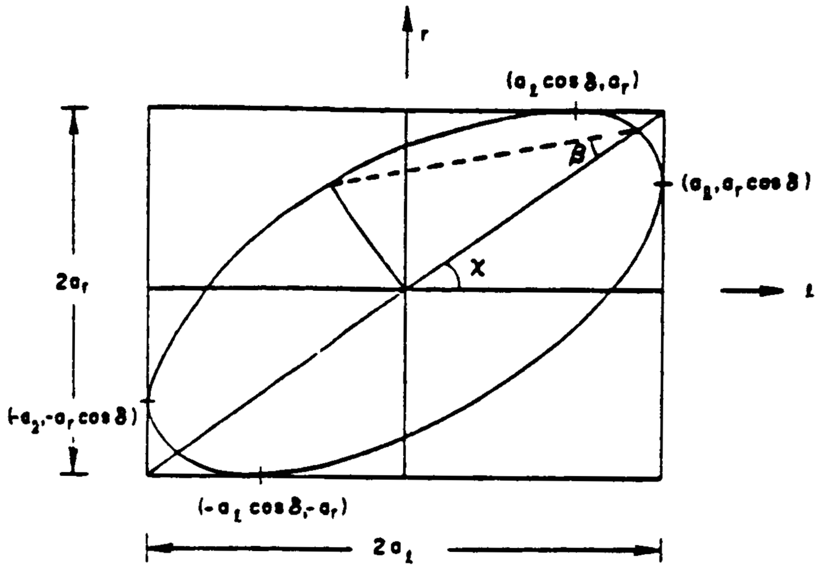

Figure 3.3 Representation of elliptical polarization.

From Liou (1980).

tion. Knowing χ is equivalent to knowing the plane of polarization, or that plane through the direction of propagation and the ray containing the maximum electric field vector. Also, let the ellipticity be represented by the angle β, whose tangent is the ratio of the lengths of the major and minor axes. It can be shown, as in Chandrasekhar (1950), that

$$\begin{aligned} E &= E_\ell + E_r \\ Q &= E_\ell - E_r \\ \tan 2\chi &= U/Q \\ \sin 2\beta &= V/E \end{aligned} \tag{3.23}$$

Therefore, the parameters E and Q define the irradiances in two perpendicular directions within a plane transverse to the direction of propagation, U determines the plane of polarization, and V gives the ellipticity of the electromagnetic wave. With these, all quantities relevant to the description of the state of polarization are determined. In addition, the percentage polarization is given as

$$P = \sqrt{Q^2 + U^2 + V^2}/E \ . \tag{3.24}$$

For unpolarized light, $U = V = 0$, as the time average over $\sin\delta$ and $\cos\delta$ are zero, and $E_\ell = E_r$ (hence $Q = 0$). The polarization P equals zero, as expected. One example of unpolarized light is that which is initially from the sun (though light does become partially polarized after scattering within the atmosphere). Conversely, for a completely polarized beam, $E^2 = Q^2 + U^2 + V^2$ and $P = 1$.

The expressions

$$\begin{aligned} A_\ell &= S_\ell \, A_{o\ell} \\ A_r &= S_r \, A_{or} \end{aligned} \tag{3.25}$$

are next utilized to determine the four Stokes parameters of the scattered field. S_ℓ and S_r relate the magnitude of the scattered fields A_ℓ and A_r to that of the incident fields $A_{o\ell}$ and A_{or}. They are functions of the angle between the incident and scattered directions of propagation, and as will be shown later, differ amongst the Rayleigh and Mie particles. By substituting Eq. (3.25) into Eq. (3.22), the four Stokes parameters are determined:

$$\begin{aligned} E_\ell &= S_\ell S_\ell^* E_{0\ell} \\ E_r &= S_r S_r^* E_{0r} \\ U &= U_0 \, \mathrm{Re}(S_\ell S_r^*) + V_0 \, \mathrm{Im}(S_\ell S_r^*) \\ V &= U_0 \, \mathrm{Im}(S_\ell S_r^*) + V_0 \, \mathrm{Re}(S_\ell S_r^*) \end{aligned} \qquad (3.26)$$

In much the same way as Eqs. (3.16a,b) represent the transfer of radiant flux within the atmosphere, they likewise can, with few modifications, represent the transformation of the Stokes parameters as the beam they represent undergoes scattering within the atmosphere. First, from Eq. (3.26) it can be shown that not all the scattered Stokes parameters are independent of each other. To account for this, the radiative transfer equation is rewritten in matrix form, that is,

$$\begin{aligned} L_p(\tau_f,\pm\mu,\phi) &= L_p(\tau_i,\pm\mu,\phi)\, e^{-\Delta\tau/\mu} \\ &\quad + \int_{\tau_n}^{\tau_n+\Delta\tau} J_p(\tau',\pm\mu,\phi)\, e^{-\Delta\tau'/\mu}\, d\tau'/\mu \end{aligned} \qquad (3.27a)$$

and

$$\begin{aligned} J_p(\tau',\pm\mu,\phi) &= \int_{4\pi} P_{pq}(\mu',\phi';\pm\mu,\phi)\, L_q(\tau',\mu',\phi')\, d\omega' \\ &\quad + P_{pq}(-\mu_0,\phi_0;\pm\mu,\phi)\, E_{0q}\, e^{-\tau'/\mu_0} \, . \end{aligned} \qquad (3.27b)$$

Here p and q are related to one of the four Stokes parameters, and P_{pq} is a 4 × 4 matrix. Thus, the pth component of radiance is determined by summing the source function over the four incoming Stokes components, that is, q = 1, 2, 3, and 4.

The matrix P_{pq} cannot be written directly from Eq. (3.26). Because the equation of radiative transfer traces components relative to a vertical plane within the atmosphere, and not the scattering plane, a coordinate transformation must be performed. The most general such scattering phase matrix has been given by Sekera (1955). It takes the form

$$P_{pq} = \begin{bmatrix} A_{11}A_{11}^{*} & A_{12}A_{12}^{*} & \mathrm{Re}(A_{11}A_{12}^{*}) & -\mathrm{Im}(A_{11}A_{12}^{*}) \\ A_{21}A_{21}^{*} & A_{22}A_{22}^{*} & \mathrm{Re}(A_{21}A_{22}^{*}) & -\mathrm{Im}(A_{21}A_{22}^{*}) \\ 2\,\mathrm{Re}(A_{11}A_{21}^{*}) & 2\,\mathrm{Re}(A_{12}A_{22}^{*}) & \mathrm{Re}(A_{12}^{*}A_{21}+A_{11}A_{22}^{*}) & -\mathrm{Im}(A_{21}A_{12}^{*}+A_{11}A_{22}^{*}) \\ 2\,\mathrm{Im}(A_{11}A_{21}^{*}) & 2\,\mathrm{Im}(A_{12}A_{22}^{*}) & \mathrm{Im}(A_{11}A_{22}^{*}-A_{12}^{*}A_{21} & \mathrm{Re}(A_{11}A_{22}^{*}-A_{21}A_{12}^{*}) \end{bmatrix} \tag{3.28}$$

The quantities A_{pq} are given by

$$\begin{aligned} A_{11} &= T_1 \cos\Delta\phi + T_2 \cos\psi \\ A_{12} &= (\mu' T_1 + \mu T_2) \sin\Delta\phi \\ A_{21} &= (\mu T_1 + \mu' T_2) \sin\Delta\phi \\ A_{22} &= T_1 \cos\psi + T_2 \cos\Delta\phi \; . \end{aligned} \tag{3.29}$$

Here μ and μ' are directional cosines of the incident and scattered beams (measured, as before, from the local vertical). The angle $\Delta\phi$ is defined as the difference between the azimuth angles of the incident and scattered beams. Furthermore,

$$\begin{aligned} \cos\psi &= (1 - \mu^2)^{1/2} (1 - \mu'^2)^{1/2} + \mu\mu' \cos\Delta\phi \\ T_1 &= (S_\ell - XS_r)/(1 - X^2) \\ T_2 &= (S_r - XS_\ell)/(1 - X^2) \\ X &= \cos\theta = \mu\mu' + (1 - \mu^2)^{1/2} (1 - \mu'^2)^{1/2} \cos\Delta\phi \end{aligned} \qquad (3.30)$$

and S_ℓ and S_r are the proportionality constants defined in Eq. (3.25). Note that all the functions within Eqs. (3.28) through (3.30) are defined with respect to the angles θ, θ', and $\Delta\phi$, all angles relative to a vertical plane within the atmosphere.

Rayleigh Scattering by Molecules

Both molecules, whose radii r are on the order of 10^{-4} μm, and aerosols, whose radii range from 0.01 to 10 μm, are responsible for scattering within the atmosphere. Molecular scattering in the visible and near ir, where $2\pi r \ll \lambda$, can be characterized by a simple scattering law due to Lord Rayleigh (J. W. Strutt, third Baron of Rayleigh). In 1872 he derived the scattering law that now bears his name, using the elastic-solid ether theory. He predicted that scattering varies inversely as the fourth power of the wavelength, and so explained the blue color of the sky. In 1899 Rayleigh revised his derivation to use the electromagnetic theories of Maxwell and Hertz. Thus, the dependence of scattering on refractive index was determined. The scattering law has since undergone one slight revision to account for molecular anisotropy. This was done in the 1920s, shortly after some scattering experiments made by Rayleigh's son demonstrated the need for this modification. A complete development of the Rayleigh scattering law is given in texts such as McCartney (1976). Highlights of its development are given here.

Dipole Scattering

The mechanical oscillator model of the atom is used to study the interaction of a molecule with an incident field. A binding force is characterized by a spring that induces a linear restoring force to the electron as it is displaced. Such a displacement occurs when a molecule is subject to an applied electric field, A_0. An induced dipole moment $p = ex$ is created, where e is the charge on an electron and x is the displacement. This electric dipole oscillates synchronously with the field, and in turn produces the scattered wave. The new field is proportional to (1) the acceleration of the electron and to (2) $\sin\theta$, where θ is the angle between the dipole moment and direction of observation, and it is inversely proportional to R, the distance from the dipole. It has an amplitude

$$A = \frac{\omega^2 p_0 \sin\theta \, \sin\omega(t-R/c)}{4\pi\varepsilon_0 c^2 R} . \qquad (3.31)$$

Because of the $\sin\theta$ dependence, the dipole cannot radiate along the axis of the dipole. The maximum dipole moment p_0 is found by solving the equation of motion for the maximum electron displacement:

$$p_0 = ex_0 = \frac{e^2 A_0}{m(\omega_0^2 - \omega^2)} = \frac{n^2-1}{n^2+2} \frac{3\varepsilon_0}{N} A_0 . \qquad (3.32)$$

Here, ω_0 is the resonant frequency of oscillation, equal to $\sqrt{k/m}$ where k is the restoring force on the electron.

The latter equality within Eq. (3.32) utilizes the Lorenz-Lorentz expression to substitute for the molecular parameters. Now n, the refractive index of the gas in bulk form, and N, the number of dipole oscillators per unit volume, are used. The refractive index of air molecules considered here is found to be nearly 1 and real, and to vary as a function of wavelength. This wavelength dependence is given by Edlen (1953) as

$$(n-1) \times 10^8 = 6432.8 + \frac{2,949,810}{146 - \lambda^{-2}} + \frac{25,540}{41 - \lambda^{-2}} \quad . \qquad (3.33)$$

For example, $n = 1.000293$ at $\lambda = 0.55$ μm. Both the Lorenz-Lorentz and Edlen expressions are derived in many discussions on the dispersion of electromagnetic waves, as in Liou (1980).

The Rayleigh expressions assume that scatterers have resonant frequencies far above the visible and infrared spectral regions. Thus they are pure scatterers and absorb no energy. Such an assumption is valid for nitrogen and oxygen molecules, which are responsible for 99% of molecular scattering. Ozone and water vapor molecules have an imaginary component to their refractive index at those wavelengths of interest (that is, they have resonant frequencies near those frequencies corresponding to visible light). The effects of scattering from these species can be overlooked without loss of accuracy, as they compose such a small fraction of the atmospheric gases. (The columnar amount of ozone is typically on the order of 0.35 atm-cm. This implies that there will be only 0.35 cm of ozone within a 1 cm^2 atmospheric column of air, in which there are several kilometers of atmospheric scatterers.)

The irradiance produced at a distant point R from the dipole is given by the Poynting vector $\overline{E}$,

$$\overline{E} = c\, \varepsilon_0 \langle A^2 \rangle \ . \tag{3.34}$$

The mean of A^2 is found by substituting a factor of 1/2 for $\sin^2\omega(t-R/c)$, and using Eqs. (3.31) and (3.32) for the electric field strength. To remove the dependence of scattering on distance R, the intensity I (W/sr) is instead computed. The intensity at distance R is found by multiplying the irradiance $\overline{E}$ by R^2 (since $I = d\Phi/d\omega = d\Phi/dA * dA/d\omega$, and $dA = R^2\, d\omega$). Hence,

$$I(\theta) = \frac{\pi^2\, \varepsilon_0\, c\, \sin^2\theta\, (n^2-1)^2\, A_0^2}{2\, N^2\, \lambda^4} \ . \tag{3.35}$$

In addition to the previous equations, the substitutions $\omega = 2\pi c/\lambda$ and $(n^2+2)^2 \approx 9$ (since $n \approx 1$) have been made in writing Eq. (3.35).

Cross Section

The scattering cross section of a gas molecule is defined as that cross section of an incident wave, acted on by the molecule, having an area such that the irradiance flowing across it is equal to the flux scattered in all directions. Thus,

$$\sigma = \frac{\int_{4\pi} I(\theta')\, d\omega'}{c\ \varepsilon_0\ A_0^2/2} \ . \tag{3.36}$$

Using Eq. (3.35), $d\omega' = 2\pi \sin\theta'\, d\theta'$, and $\int_0^\pi \sin^3\theta'\, d\theta' = 4/3$, the cross section is obtained. To this the correction factor $(6 + 3\delta)/(6 - 7\delta)$ must be added. This is done to account for molecular anisotropy, which prevents the dipole moment from aligning itself exactly with the electric vector of the primary wave. Thus,

$$\sigma_{Ray} = \frac{8\pi^3(n^2-1)^2}{3\ N^2\ \lambda^4}\ \frac{6 + 3\delta}{6 - 7\delta} \ . \tag{3.37}$$

Gucker and Basu (1953) have determined that $\delta = 0.035$.

Rayleigh Optical Depth

The volume scattering coefficient for molecules, β_{Ray}, gives the fractional amount of flux scattered in all directions for a unit volume of gas. Because the scattered field from a collection of dipoles adds incoherently, the coefficient for a unit volume is just N (molecules/volume) times the cross section given by Eq. (3.37), or $\beta_{Ray} = \sigma_{Ray}\ N$. (Also, the mass extinction coefficient is found to be $k_{Ray} = \sigma_{Ray}\ N/\rho = \sigma_{Ray}/m$, or cross section per unit mass. Here m is the mass of the molecule and ρ is the mass density.) Using the definition of optical depth, Eq. (3.8), the Rayleigh component of optical depth is determined by

$$\tau_{Ray} = \sigma_{Ray} \int_{z}^{\infty} N(z)\, dz \; . \qquad (3.38)$$

Model values of the molecular number density as a function of altitude can be found in the U.S. Standard Atmosphere of 1962 (USSA, 1962; Valley, 1965; Elterman, 1968), and Table 4.4 (page 84) of this manuscript.

The tabulated values of mass density ρ, or number density N, refer to air at sea-level temperature and pressure. It is desirable to compute the scattering coefficients at nonstandard values of temperature, pressure, and altitude. This is done using the equation of state for an ideal gas ($P = \rho RT$, P being atmospheric pressure, R the universal gas constant, and T the temperature on the Kelvin scale). Thus,

$$\rho = \rho_0 \frac{P}{P_0} \frac{T_0}{T} \; , \qquad (3.39)$$

where ρ_0, P_0, and T_0 are defined at standard atmosphere conditions.

In using the Herman code to model the atmosphere, τ_{Ray} is determined using surface measured atmospheric pressure. At ground level,

$$\tau_{Ray} = \frac{8\pi^3(n^2-1)^2}{3\,\lambda^4 N_s^2} \; \frac{6 + 3\delta}{6 - 7\delta} \; N_c \; 10^{16} \; \frac{P}{P_0} \; , \qquad (3.40)$$

where

n = refractive index as given by Eq. (3.33)

λ = wavelength in μm

N_s = molecular number density at sea level for a standard atmosphere

= $2.547 \times 10^{19}\ cm^{-3}$

N_C = columnar number density = $2.154 \times 10^{25}\ cm^{-2}$

δ = 0.035

P_0 = 1013.25 mbar, or 29.92 in. Hg

P = measured atmospheric pressure in same units as P_0.

Using this formalism at $\lambda = 0.55\ \mu m$, for example, $\tau_{Ray} = 0.098$ at standard atmospheric pressure.

Phase Function

The angular dependence on scattering is expressed in terms of the phase function $P(\theta)$. Since there is no absorption by Rayleigh molecules, the integral of the phase function must be normalized to unity and

$$\int_{4\pi} P(\theta)\, d\omega' = k_s/k_T = 1 \ . \tag{3.41}$$

To derive the phase function for the scattering of unpolarized light by Rayleigh particles, the incident electric field vector is decomposed into two orthogonal components. As before, let E_ℓ and E_r represent those scattered components paralle$\underline{l}$ and perpendicula$\underline{r}$ to a reference plane, and let $E_{0\ell}$ and E_{0r} be the corresponding incident components. The reference plane is taken as that containing the incident and scattered waves, and the scattered wave deviates from the incident wave by an angle θ. For each of these two components ($i = \ell$ or r), the scattered radiance is found using

$$dL(\theta_i) = I(\theta_i)\,\frac{6+3\delta}{6-7\delta}\,N\,ds$$

$$= \frac{3}{8\pi}\,\sigma_{Ray}\,N\,ds\,\sin^2\theta_i\,E_{oi}\,. \qquad (3.42)$$

To derive this expression, note that $I(\theta)$ is the intensity scattered from a single molecule, and $I(\theta)N\,ds$ is the radiance scattered from a volume of gas. After accounting for anisotropy, the intensity is expressed in terms of σ_{Ray} by using Eqs. (3.35) and (3.37) and expressing the incident irradiance $c\varepsilon_0 A_{oi}{}^2/2$ as E_{oi}.

The angles θ_ℓ and θ_r can readily be expressed in terms of the scattering angle, θ. With reference to Fig. 3.4, it is shown that $\theta_\ell = \pi/2-\theta$, and $\theta_r = \pi/2$. Hence, the total scattered radiance is

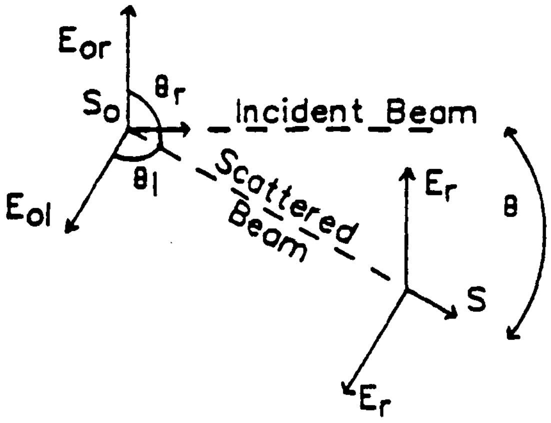

Figure 3.4 Dipole scattering.

given as

$$dL = dL_r + dL_\ell$$

$$= \frac{3}{8\pi}\,\sigma\mathrm{Ray}\ N\,ds\,E_{0r} + \frac{3}{8\pi}\,\sigma\mathrm{Ray}\ N\,ds\,\cos^2\theta\ E_{0\ell}\ . \qquad (3.43)$$

But, since the incoming field is unpolarized, $E_{0r} = E_{0\ell} = E_0/2$. Equation (3.43) becomes

$$dL = \sigma\mathrm{Ray}\ N\,ds\,\frac{3}{16\pi}\,(1 + \cos^2\theta)\,E_0\ . \qquad (3.44)$$

Removing the angular dependence and multiplying by a scaling factor to satisfy Eq. (3.41), the phase function for Rayleigh scattering of unpolarized light is found to be

$$P(\theta) = \frac{3}{16\pi}\,(1 + \cos^2\theta)\ . \qquad (3.45)$$

This expression is the Rayleigh component of the phase function used within Eq. (3.16). It is thus an important parameter in the calculations of the transfer of radiace within the atmosphere.

Because the perpendicular and parallel components are not scattered equally, the resulting radiance will be partially polarized. Although the scattered perpendicular component is independent of the angle θ, the parallel component follows a $\cos^2\theta$ dependence. Thus, if the observation direction is at 90° to the incoming beam, the scattered light will be completely polarized. The scattered energy is symmetric about the incident beam, and equal amounts of energy are sent into the forward and backward hemispheres. If there were only single scattering within the atmosphere, and the atmosphere were composed purely of Rayleigh particles, the skylight everywhere at a 90° angle from the earth-sun line would be completely polarized. This perfectly polarized light is never observed in practice because of multiple scattering within the atmosphere, scattering from aerosols, light reflected from the surface, and anisotropy of air molecules.

If these polarization changes are to be traced through the atmosphere, the matrix form of the phase function is required. For Rayleigh scattering, this becomes

$$P_{pq} = \frac{3}{8\pi} * \begin{bmatrix} \cos^2\psi & \mu^2\sin^2\Delta\phi & \mu\cos\psi\ \sin\Delta\phi & 0 \\ \mu'^2\sin^2\Delta\phi & \cos^2\Delta\phi & -\mu'\sin\Delta\phi\ \cos\Delta\phi & 0 \\ \begin{matrix} -2\mu'\cos\psi \\ * \sin\Delta\phi \end{matrix} & \begin{matrix} 2\mu\sin\Delta\phi \\ * \cos\Delta\phi \end{matrix} & \begin{matrix} -\mu\mu'\sin^2\Delta\phi \\ + \cos\psi\ \cos\Delta\phi \end{matrix} & 0 \\ 0 & 0 & 0 & \begin{matrix} \cos\psi\ \cos\Delta\phi \\ + \mu\mu'\sin^2\Delta\phi \end{matrix} \end{bmatrix} . \tag{3.46}$$

Mie Scattering

To describe scattering by particles of arbitrary size, the equations developed by Mie (1908) are universally used. In developing this theory, Mie had to make the simplifying assumption that the scattering particles were isotropic spheres. Even so, the derivation is complex; it uses Maxwell's equations, a boundary value analysis, and an expansion of the emerging wave in terms of a series of Bessel and Legendre polynomials. For small particles the equations can be approximated by the first term of the Mie series. For this case, however, Rayleigh theory yields an equivalent result with significantly fewer computations. Thus, the term "Mie scattering" is loosely used to refer to the scattering by larger particles that do not lie within the Rayleigh regime.

A complete development of Mie theory is given by Stratton (1941) and van de Hulst (1957). The scattered light is found by breaking the incident beam into components perpendicular and parallel to the scattering plane. The scattered intensities $I_r(\theta)$ and $I_\ell(\theta)$ are proportional to the functions

$$i_r = \left|\frac{2\pi}{\lambda} S_r\right|^2 = \left|\sum_{n=1}^{\infty} \frac{2n+1}{n(n+1)} (a_n \pi_n + b_n \tau_n)\right|^2 \qquad (3.47a)$$

$$i_\ell = \left|\frac{2\pi}{\lambda} S_\ell\right|^2 = \left|\sum_{n=1}^{\infty} \frac{2n+1}{n(n+1)} (a_n \tau_n + b_n \pi_n)\right|^2 . \qquad (3.47b)$$

Each function is found as the sum of an infinite series. Defining the size parameter as $\alpha = 2\pi r/\lambda$, where r is the the radius of the particle, it is found that the number of terms required for convergence is somewhat greater than α for $\alpha > 1$. The amplitudes of the nth electric partial wave and the nth magnetic wave are given by the complex coefficients a_n and b_n. These are

$$a_n = -\frac{j_n(m\alpha)[\alpha\, j_n(\alpha)]' - j_n(\alpha)[m\alpha\, j_n(m\alpha)]'}{j_n(m\alpha)[\alpha\, h_n^{(2)}(\alpha)]' - h_n^{(2)}(\alpha)[m\alpha\, j_n(m\alpha)]'} \qquad (3.48a)$$

$$b_n = -\frac{j_n(\alpha)[m\alpha\, j_n(m\alpha)]' - m^2\, j_n(m\alpha)[\alpha\, j_n(\alpha)]'}{h_n^{(2)}(\alpha)[m\alpha\, j_n(m\alpha)]' - m^2\, j_n(m\alpha)[\alpha\, h_n^{(2)}(\alpha)]'} \,. \qquad (3.48b)$$

With air as the incident medium, the parameter $m = n_{re}(1 - n_{im}i)$ is related to both the real and imaginary components of the refractive index within the sphere. Spherical Bessel and Hankel functions are denoted by j_n and h_n respectively, and primes denote derivatives with respect to the indicated arguments. Thus the coefficients a_n and b_n are determined from the particle characteristics, but are independent of the scattering angle θ. This latter dependence is expressed through the functions π_n and τ_n and involve the first and second derivatives of Legendre polynomials:

$$\pi_n(\cos\theta) = \frac{d[P_n(\cos\theta)]}{d(\cos\theta)} \qquad (3.49a)$$

$$\tau_n(\cos\theta) = \cos\theta\, \pi_n(\cos\theta) - \sin^2\theta\, \frac{d[\pi_n(\cos\theta)]}{d(\cos\theta)} \,. \qquad (3.49b)$$

When the particle is illuminated by plane-polarized light, the intensity of the scattered light is given by

$$I(\theta) = E_0\, \frac{\lambda^2}{4\pi^2}\, (i_r \sin^2\psi + i_\ell \cos^2\psi) \,. \qquad (3.50)$$

Here E_0 is the irradiance of the incoming beam, ψ is the angle of the electric vector from the scattering plane, and i_r and i_ℓ are as defined in Eq. (3.47). For a particle illuminated with a wave whose electric vector is perpendicular to the plane of observation, $\psi = 90°$ and the scattered beam is polarized in the perpendicular direction. Conversely, an incident beam described by $\psi = 0$ is polarized parallel to the scattered plane, as is the scattered beam. For illumination by an unpolarized beam, the scattered intensity is given by

$$\begin{aligned} I(\theta) &= E_{0r} \frac{\lambda^2}{4\pi^2} i_r + E_{0\ell} \frac{\lambda^2}{4\pi^2} i_\ell \\ &= E_0 \frac{\lambda^2}{8\pi^2} (i_r + i_\ell) \end{aligned} \tag{3.51}$$

where $E_{0r} = E_{0\ell} = E_0/2$.

The angular distribution of the scattered field is depicted in Fig. 3.5. Here the solid lines refer to scattering from a perpendicular component of the electric vector, and the dashed lines represent scattering from a parallel component. For $\alpha < 0.1$ the distribution is identical to that predicted from Rayleigh theory. There is a $\cos^2\theta$ dependence in the scattered parallel component but no angular variation in the perpendicular component. As α increases (or particle size increases for a given wavelength), a larger portion of the energy is scattered into the forward direction. If the particle size approaches the wavelength of light, sidelobes begin to appear. The frequency of this structure increases with α, and the width decreases.

The cross section of a Mie scatterer can now be defined. Unlike scattering from a Rayleigh particle, some energy is lost owing

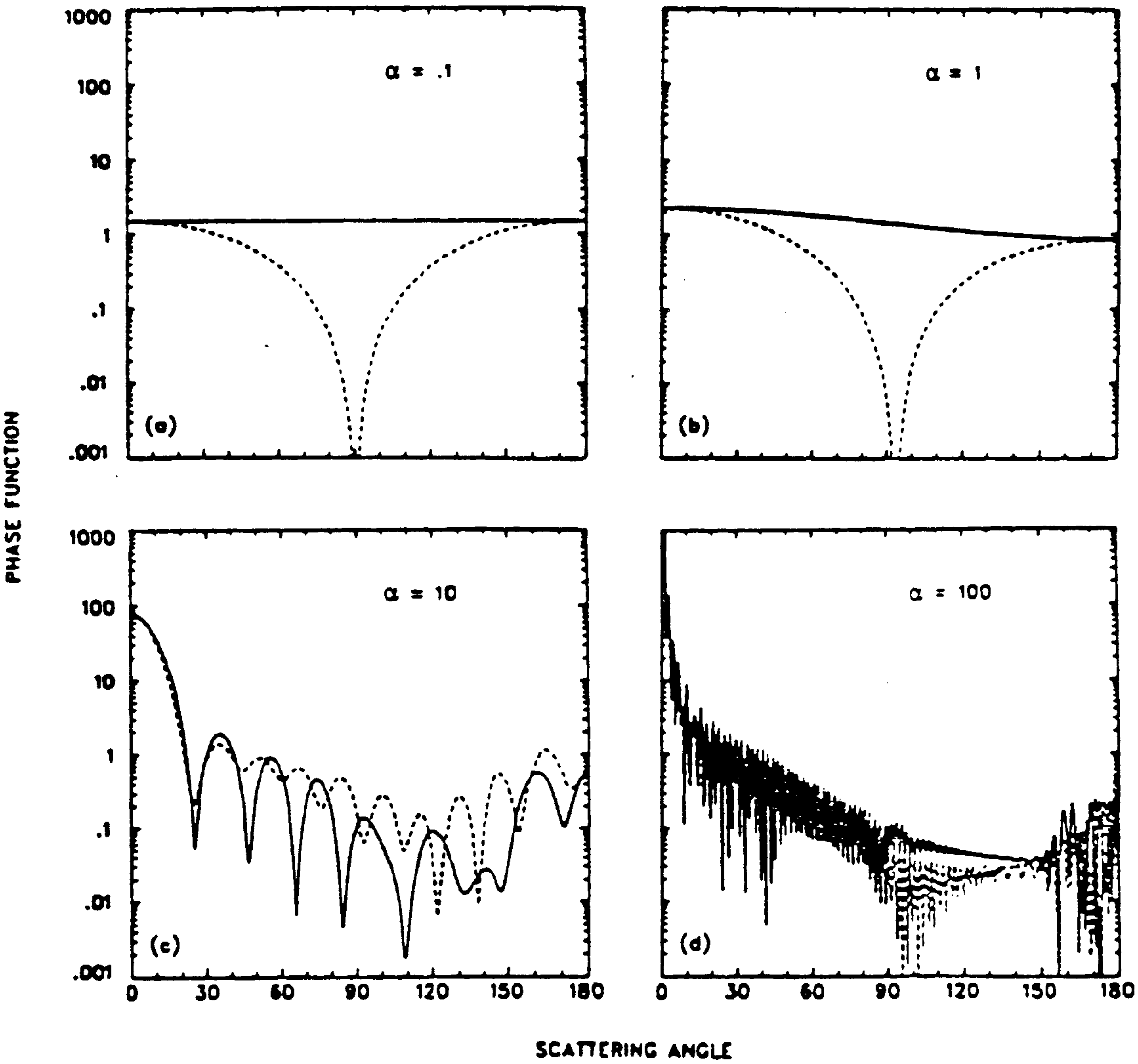

Figure 3.5 Mie scattering from particles of fixed size.

Normalized phase functions for spherical particles with complex refractive index n = 1.5 - 0.0005i and Mie size parameters (a) α = 0.1, (b) α = 1, (c) α = 10, and (d) α = 100. Solid lines are values for components perpendicular to the scattering plane; dashed lines are the parallel components of incident light. From Grams and Rosen (1978).

to absorption as a beam impinges upon a Mie scatterer. The cross section σ_{Mie} must include the effects of this loss. Defining σ_{sc} as the component that accounts for the energy scattered into all directions, and σ_{abs} as the component that accounts for absorption, we have

$$\sigma_{Mie} = \sigma_{sc} + \sigma_{abs} . \tag{3.52}$$

Using Eq. (3.51) and assuming unpolarized illumination, σ_{sc} is computed from

$$\begin{aligned}\sigma_{sc} &= \int_{4\pi} I(\theta)\, d\omega/E_{\circ} = \frac{\lambda^2}{8\pi^2}\int_{4\pi} (i_r + i_\ell) \sin\theta \, d\theta \, d\phi \\ &= \frac{\lambda^2}{2\pi} \sum_{n=1}^{\infty} (2n+1)(|a_n|^2 + |b_n|^2) .\end{aligned} \tag{3.53}$$

The total cross section can likewise be expressed in terms of the Mie coefficients,

$$\sigma_{Mie} = \frac{\lambda^2}{2\pi} \sum_{n=1}^{\infty} (2n+1) \operatorname{Re}(a_n + b_n) . \tag{3.54}$$

In the above, the expansions in terms of a_n and b_n do not easily follow. (Refer to van de Hulst (1957, section 9.32) for more details.)

To simplify, the above cross sections were defined for a particle of fixed radius r. In reality, absorption and scattering within the atmosphere depend on the cumulative effects of many particles within a large size range. This distribution is expressed in terms of a size distribution n(r). It is the normalized number of particles per unit interval of radius per unit volume, hence

$$\int_0^\infty n(r)\, dr = 1 . \qquad (3.55)$$

To determine the properties of light scattered from a polydispersion (collection of particles of different radii), the functions i_r and i_ℓ within Eq. (3.53) are integrated over the size distribution. The scattered energy from such a distribution of particles is very different from that depicted above. The most obvious difference is that the scattered distribution is a much smoother function of wavelength. A few examples of this are shown in Fig. 3.6. To compute these curves, a log normal particle distribution was assumed. A mean radius of r_g = 1 μm, standard deviation $\sigma = 2$ μm, wavelength $\lambda = 0.633$ μm, and real refractive index $n_{re} = 1.525$ were assumed. Curves (a) and (b) give the results for a parallel and perpendicular incident electric vector, respectively. In curves (c) and (d) the molecular scattering contributions have been added. Each example has been computed at several values of the imaginary component of refractive index. As n_{im} increases, the light scattered into angles greater than $\theta = 15°$ decreases. The most significant result of increasing the imaginary refractive index, however, is the increase in absorption. This change can be expressed through the parameters σ_{abs}, or the single scatter albedo.

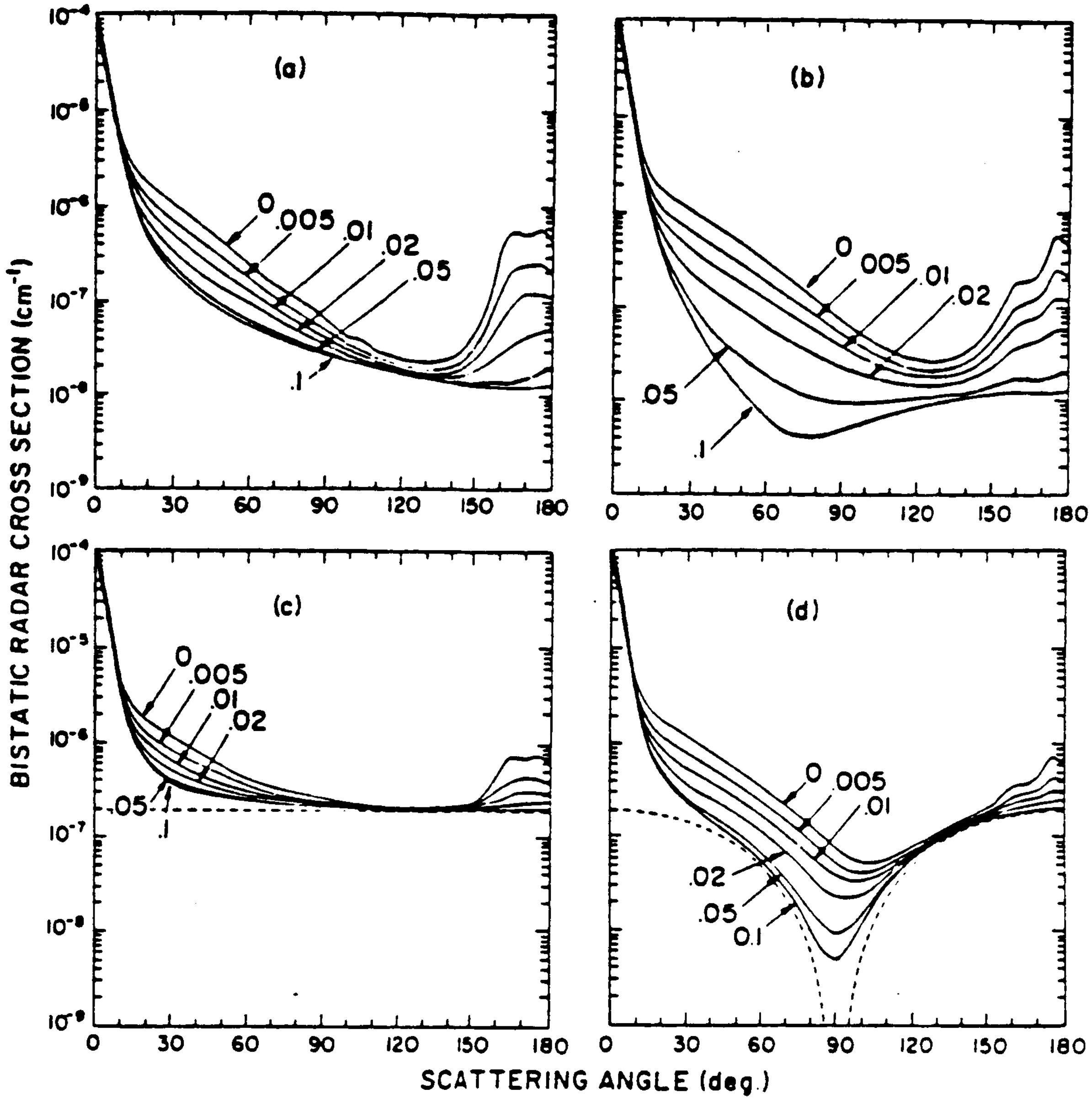

Figure 3.6 Mie scattering by atmospheric polydispersions.

Aerosols are given log normal size number distributions with $r_g = 1$ μm, $\sigma = 2$, and $N_p = 1$ particle/cm^3 in the scattering plane (a) perpendicular and (b) parallel to the electric vector of incident polarized light at a wavelength of 0.633 μm. Curves (c) and (d) are the result of adding molecular scattering contributions at standard temperature and pressure (dashed lines) to the aerosol scattering calculations of (a) and (b) respectively. Calculations refer to particles having $n_{re} = 1.525$ and the indicated values of n_{im}. From Grams and Rosen (1978).

C-2

By integrating the cross section over the size distribution function, the optical depth of the atmosphere can be determined. Defining N(z) as the total number of particles per unit volume at altitude z,

$$\tau_{Mie} = \int\int N(z)\,\sigma_{Mie}(r)\,n(r)\,dr\,dz \;. \tag{3.56}$$

Note that the size distribution is taken as constant with respect to altitude. This is usually assumed the case for lack of better data. More will be said about the radial size distribution function n(r) and the vertical distribution N(z) in the next chapter.

By integrating the cross section over the size distribution, the phase function for Mie scattering can also be found. To see this most readily, let us define the angular scattering cross section $\sigma_{sc}(\theta)$ as the cross section of the incident wave acted on by the particle having an area such that the irradiance flowing across it is equal to the intensity scattered into angle θ. The cross section σ_{sc} defined earlier is equal to the angular cross section integrated over all outgoing angles. With this, the phase function is defined as

$$P(\theta) = \frac{\int \sigma_{sc}(\theta,r)\,n(r)\,dr}{\int \sigma_{Mie}(r)\,n(r)\,dr} \;. \tag{3.57}$$

From this definition it is apparent that the integral of the phase function over all solid angles will not necessarily be equal to 1. It will equal the single scatter albedo and will be equal to 1 only if there is no absorption of energy by the particle (in such a case $\sigma_{Mie} = \sigma_{sc}$). The greater the imaginary component of refractive index, the smaller the single scatter albedo, hence a smaller fraction of energy will be scattered and a greater fraction absorbed.

For illumination by unpolarized light,

$$P(\theta) = \frac{\lambda^2/8\pi^2 \int n(r)(i_r + i_\ell)\, dr}{\int \sigma_{Mie}(r)\, n(r)\, dr} . \qquad (3.58)$$

To run the version of the Herman code that accounts for polarization, the phase function must be written in matrix form. This is done by using S_r and S_ℓ, as defined in Eq. (3.47), within Eqs. (3.28) through (3.30).

Another parameter, closely related to the cross section, that is commonly referred to in the literature is the efficiency factor Q, defined as the cross section of a particle divided by the geometric cross sectional area of that particle, πr^2. If the scattering efficiency factor is plotted versus the size paramter α, Q_{sc} obtains a maximum value of as large as 6, and converges in an oscillatory fashion to a value between 1 and 2 for high α. This implies that the particle can, at times, interact with an incident wavefront greater than its own geometric area. This is explained through diffraction effects, in which diffracted flux is directed into a small angle centered about the forward direction of the incident flux.

Dave Code

To compute the Mie parameters discussed above, a Fortran computer program written by Dave (1969) is used. This program is incorporated into one of the subroutines within the Herman code. Two similar Dave codes exist, one using an upward recurrence relationship in which, starting with a value of $a_0(m\alpha)$, successively higher values are computed, and one using a downward recurrence relationship. In the code that uses an upward recurrence algorithm, any error in the first term will propagate, and for large enough α the results oscillate wildly around the correct value. For this reason the downward recurrence routine is preferred. It does, however, require more storage and 10% to 20% more run time. Both codes require double precision arithmetic, and output results are accurate to six significant figures (with the one exception mentioned above, in which oscillations occur).

CHAPTER 4

MODEL ATMOSPHERES

To calibrate an in-orbit sensor using ground-based measurements, the effects of the atmosphere on propagating radiation must be known. This, in turn, requires that atmospheric parameters affecting radiative transfer be determined. Optical depth, temperature, pressure, and relative humidity are measured on site throughout the morning of the Landsat overpass. It is not feasible, however, to measure all the necessary parameters. For example, the vertical structure of the atmosphere, and aerosol properties such as refractive index, are not easily determined. These unknowns must be characterized with assumed values, based upon data reported in the literature and published models of the atmosphere.

Various models have been constructed that define properties such as temperature, pressure, density, and ozone and water vapor concentrations, as functions of altitude. The U.S. Standard Atmosphere of 1962 (USSA, 1962; Valley, 1965) was established jointly by the U.S. Air Force, U.S. Weather Bureau, and NASA. It gives mean annual values for the mid-latitude belt. To account for variations with latitude and season, the U.S. Standard Atmosphere Supplements of 1966 (USSAS, 1966) were established. McClatchey et al. (1972) make use of these data to construct an attenuation model for the atmosphere. This work is the basis of the LOWTRAN 6 (Kneizys et al., 1983) computer code.

In addition to knowing the atmospheric properties for the days in which Landsat images the earth over White Sands, it is convenient to know what range these parameters may assume. This allows us to define measurement techniques and to estimate the uncertainty of the calibration procedure. This chapter defines a set of model parameters, applicable to the White Sands area. Particular attention is given to those parameters that are required as input to the Herman code. In addition, the range these parameters may assume is predicted. These data are used in the sensitivity study, Chapter 6, and were also used in Chapter 2 to predict the saturation of Landsat imagery. We begin by discussing aerosol characteristics.

Aerosol Characteristics

An aerosol is a dispersed system of small particles suspended in a gas. The aerosols present in the earth's atmosphere have a variety of origins. These include dusts (particularly from arid zones and deserts), volcanic ash, foliage exudations, sea salts, and combustion products. Aerosols introduced into the atmosphere are modified by coagulation, fallout, and washout, which tend to eliminate the very large and very small particles, leaving most particles in the 0.01 to 10.0 μm range. The exact composition of these aerosols depends upon local sources and sinks, meteorological conditions, and geographic locale. Common atmospheric aerosol materials are a 75% solution of H_2SO_4, water-soluble materials consisting of ammonium, calcium sulfate and organic materials, dust, soot, clay, and $(NH_4)_2SO_4$.

To the extent that aerosols can be modeled as isotropic spheres, Mie theory can predict their absorption and scattering of light. For input to the Mie equations, however, it is necessary to know such aerosol properties as refractive index, radial size distribution, and vertical distribution within the atmosphere. Some of these aerosol parameters can be measured. For example, Mie optical depth data can be inverted to obtain the aerosol radial size distribution. Other parameters are more difficult to measure, and model data are used instead. For example, not only are the techniques for measuring refractive index relatively inaccurate, but it often requires several months to collect and evaluate samples. The vertical distribution could be determined in situ, but only through use of costly techniques, such as lidar. As we shall see, the large uncertainty that can be tolerated in this parameter does not warrant such an expensive and time-consuming effort.

Radial Size Distributions

One of the most popular models for the radial size distribution is the Junge, or power law distribution (defined by Junge, 1963). This law was developed from measurements made over Germany in 1958. McCartney (1976) references many investigators who have successfully fit their measured data to this function. The Junge distribution is

$$n(r) = \frac{dN}{N\, d(\log r)} = c' r^{-\nu} . \tag{4.1}$$

Here N is the number of particles per unit volume, c' is a normalization constant, and the exponent ν determines the slope of the distribution curve. Thus n(r) is the number of particles per increment in log r, normalized to the total number of particles. The integral of the size distribution over the radial limits is defined as unity. By noting that d(log r) = 0.434 dr/r, we find the nonlogarithmic form of the distribution:

$$n(r) = dN/(N\,dr) = cr^{-\nu+1} , \tag{4.2}$$

where c = 0.434c'. The parameter ν typically ranges from 2.5 to 4.0. The relative number of small particles increases with ν. The Junge distribution for this range is depicted in Fig. 4.1(a).

A wavelength dependence to optical depth can be empirically related to the radial size distribution of aerosols. The first such relationship was suggested by Ångström (1929), who concluded that

$$\tau_{Mie} = a\lambda^{-\gamma} . \tag{4.3}$$

For small particles, $\gamma = 4$, thus giving the Rayleigh relationship. Under hazy conditions γ may be less than 1. By assuming a Junge distribution, the above relationship can easily be derived, as was done by van de Hulst (1957). Equation (3.56) is used to describe the Mie component of optical depth in terms of the cross section $\sigma_{Mie}(r)$ and radial size distribution n(r). Making the change of variable $\alpha = 2\pi r/\lambda$, and substituting for n(r) from Eq. (4.2), we obtain

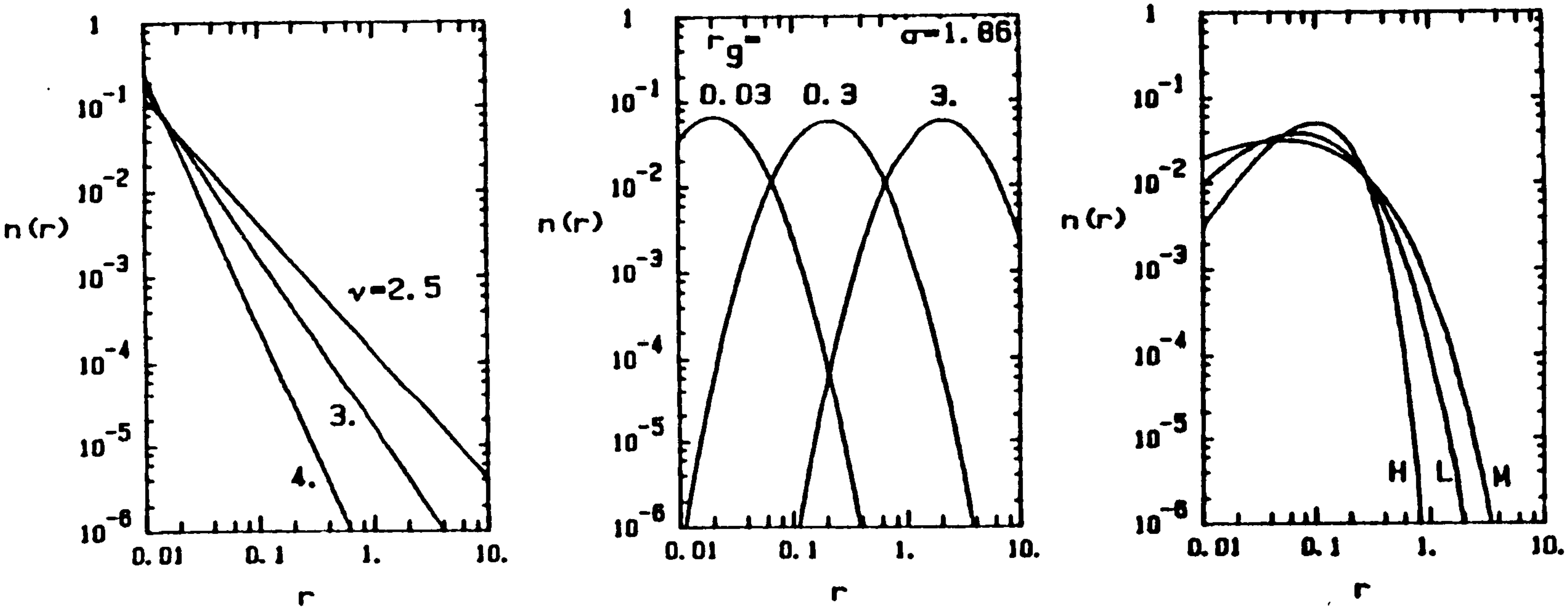

(a) (b) (c)

Figure 4.1 Model radial size distributions.

(a) Junge distribution for ν = 2.5, 3.0, and 4.0. (b) Log normal with r_g = 0.03, 0.3, and 3, all with σ = 1.86. (c) Modified gamma distributions H, L, and M. All curves are drawn for radial limits 0.01 to 10.0 μm.

$$\tau_{Mie} = c(\lambda/2\pi)^{-\nu+2} \int \int N(z)\, \sigma_{Mie}(\alpha)\, \alpha^{-\nu+2}\, d\alpha\, dz \ . \qquad (4.4)$$

It is apparent that the exponent γ within Eq. (4.3) is related to the Junge size distribution by $\gamma = \nu - 2$.

Other commonly used radial size distributions are summarized by Russell et al. (1981) and Yue and Deepak (1983). These include the log normal distribution and the modified gamma distribution proposed by Deirmendjian (1963).

The log normal is probably the most popular for background stratospheric aerosol studies. It is given by

$$n(r) = \frac{A}{\sqrt{2\pi}\ \ln\sigma} \frac{1}{r} \exp\left[- \frac{\ln^2(r/r_g)}{2\ \ln^2\sigma} \right] . \qquad (4.5)$$

Recommended values are $\sigma = 1.86$ and $r_g = 0.07$ µm, but the latter is often adjusted between 0.03 and 3.0 µm to model different atmospheric conditions. The log normal distribution is presented in Fig. 4.1(b).

The modified gamma function is of the form

$$n(r) = Ar^{\alpha} \exp(-Br^{\gamma}) \ . \qquad (4.6)$$

The name is derived from the gamma distribution, which Eq. (4.6) reduces to when $\gamma = 1$. Since the modified gamma function has four adjustable constants, it is frequently used to fit measured data. Deirmendjian (1969) defined constants for three different haze models, designated M, L, and H. The constants are given in Table 4.1.

Constant A, as defined by Deirmendjian, is determined such that n(r) when integrated from zero to infinity is equal to 100 particles/cm^3. As we prefer to work with a normalized distribution, we have defined the alternative constant A' as that required to satisy Eq. (3.55); that is, n(r) when integrated between the radial limits, taken here as 0.01 and 10.0 μm, equals 1. Model H is used for stratospheric dust particles, model L is used to represent continental aerosols, and model M is applied to maritime and coastal aerosols. These three size distributions are drawn in Figure 4.1(c). Here, as for the Junge and log normal curves, the radial limits are taken as 0.01 and 10.0 μm.

Table 4.1 Haze Model Parameters for the Modified Gamma Distribution

Distribution	A	α	B	γ	A'
Haze M	5.3333E+04	1	8.9443	0.5	4.7115
Haze L	4.9757E+06	2	15.1186	0.5	427.8681
Haze H	4.0000E+05	2	20.0000	1	11572.65

A, α, B, and γ from Deirmendjian (1969). A' defined to normalize n(r), integrated from 0.01 to 10 μm, to unity.

It must be kept in mind that no single model can define the radial size distribution precisely, as it is a dynamic property of the atmosphere. Even on a short time scale, changes in optical properties may result from local fluctuations in temperature and water vapor concentrations. As humidity increases, the particle may absorb water vapor, resulting in an increase of particle size and also a change in the effective refractive index.

Refractive Index

The complex refractive index of an aerosol particle is dependent on wavelength and the composition of the particle. Table 4.2, from Kent, Yue, and Deepak (1983), lists these refractive indices for common materials.

Of particular interest to us, however, are the atmospheric studies made in the southwestern United States. For example, researchers at the U.S. Army Atmospheric Sciences Laboratory, White Sands Missile Range, have collected and analyzed local atmospheric particles, with the intent of understanding their composition and scattering properties. Lindberg and Gillespie (1977) used a cascade impactor to collect and separate particles into one of eight size bins. After collecting continuously for three months, they had obtained enough particles for analysis. The composition was determined by use of a potassium bromide spectroscopy technique. The imaginary component of refractive index was determined from a Cary 14 spectrophotometer. They discovered that particles of a given size range had a distinct composition, hence refractive index. The imaginary component of refractive index was found to vary over several orders of magnitude. A strong wavelength dependence was also noted. The giant particles (>1 μm) were composed of clay minerals (montmorillonite, illite, and minerals of the kaolin group), gypsum, quartz, and calcite. These particles have negligibly small imaginary indices, typically <0.001, throughout the visible and near infrared. Submicron particles were predominately carbon and weakly absorbing ammonium sulfate. Carbon is known to be a strong absorber, with an imaginary

Table 4.2 Complex Indices of Refraction of Common Aerosol Materials

Aerosol model	Wavelength (μm)						
	0.488	0.55	0.6328	1.06	1.66	5.0	10.59
Water	1.336-1.E-09i	1.333-1.96E-09i	1.332-1.5E-08i	1.326-5.E-06i	1.316-9.43E-05i	1.325-0.0124i	1.179-0.6777i
Maritime	1.418-0.002i	1.418-0.002i	1.415-0.002i	1.405-0.004i	1.376-0.004i	1.372-0.010i	1.380-0.057i
Maritime/rural	1.475-0.005i	1.474-0.004i	1.473-0.004i	1.463-0.009i	1.408-0.010i	1.381-0.012i	1.550-0.071i
Rural	1.530-0.008i	1.530-0.006i	1.530-0.006i	1.520-0.014i	1.440-0.016i	1.390-0.013i	1.720-0.085i
Rural/urban	1.569-0.086i	1.569-0.082i	1.569-0.80i	1.560-0.089i	1.500-0.096i	1.492-0.116i	1.810-0.198i
Urban	1.607-0.163i	1.607-0.158i	1.607-0.154i	1.600-0.163i	1.559-0.175i	1.593-0.218i	1.895-0.310i
Water soluble	1.530-0.005i	1.530-0.006i	1.530-0.006i	1.520-0.017i	1.487-2.E-02i	1.450-0.012i	1.760-0.07i
Dustlike	1.530-0.008i	1.530-0.008i	1.530-0.008i	1.520-0.008i	1.367-8.E-03i	1.250-0.016i	1.620-0.120i
Soot	1.750-0.450i	1.750-0.440i	1.750-0.430i	1.750-0.440i	1.78-0.469i	1.970-0.600i	2.220-0.730i
Sea salt	1.500-2.E-08i	1.500-1.E-08i	1.490-2.E-04i	1.470-2.E-04i	1.456-7.E-04i	1.470-0.0025i	1.500-0.014i
Crystal	1.500-7.E-03i	1.500-6.E-03i	1.490-2.5E-03i	1.470-2.E-03i	1.456-2.5E-03	1.470-0.02i	1.500-0.2i
75% H_2SO_4	1.432-2.E-08i	1.431-2.E-08	1.429-2.E-08i	1.420-1.5E-06i	1.398-2.72E-04i	1.359-0.0123i	1.737-0.273i
Al_2O_3	1.77-2.E-07i	1.77-2.E-07	1.77-2.E-07i	1.76-6.E-08	1.74-5.5E-08i	1.62-3.1E-05i	0.55-0.061i
NaCl	1.55-1.E-07i	1.55-1.E-07i	1.55-1.E-07i	1.53-1.E-07i	1.53-1.E-07i	1.515E-07i	1.49-1.E-07i
$(NH_4)_2SO_4$	1.53-1.E-07i	1.52-1.E-07i	1.52-1.E-07i	1.51-2.4E-06i	1.49-1.8E-04i	1.46-0.006i	1.98-0.06i
Sahara dust						1.56-0.015i	1.74-0.40i
Volcanic dust						1.56-0.009i	1.95-0.40i

From Kent, Yue, and Deepak (1983)

index near 0.5. Lindberg and Gillespie concluded that there is no single value of refractive index that can be used to describe the aerosols over New Mexico.

From data such as these, Jennings, Pinnick, and Auvermann (1978) proposed a bimodal model of refractive index for aerosols found in the White Sands region. Table 4.3 lists their light aerosol loading model (they also define a model for heavy loading). Typical and extreme values of refractive index are given for two radial modes. At 10.6 μm, minimum extinction is obtained using ammonium sulfate

Table 4.3 Complex Refractive Indices for a Bimodal Particle Size Distribution Characteristic of Light Desert Aerosol Loading

		Small particle mode		Large particle mode	
Wavelength (μm)		Real index	Imaginary index	Real index	Imaginary index
0.55	Minimum	1.52	0.01	1.52	0.0001
	Typical	1.54	0.015	1.54	0.003
	Maximum	1.6	0.03	1.6	0.005
1.06	Minimum	1.5	0.01	1.5	0.0001
	Typical	1.54	0.015	1.5	0.001
	Maximum	1.6	0.06	1.6	0.005
3.8	Minimum	1.56	0.02	1.25	0.001
	Typical	1.6	0.2	1.5	0.02
	Maximum	1.8	1.0	1.8	0.05
10.6	Minimum	1.99	0.06	1.19	0.07
	Typical	2.2	1.25	1.7	0.2
	Maximum	2.04	1.28	2.18	0.02

From Jennings, Pinnick, and Auvermann (1978).

($n = 1.99-0.06i$) for the small particle mode, and sodium nitrate ($n = 1.19-0.07i$) for the large particle mode. The maximum extinction values are determined from carbon ($n = 2.04-1.28i$) and quartz ($n = 2.18-0.02i$) for the small and large modes, respectively. Jennings and coworkers noted that serious errors are introduced in the computed extinction if an average refractive index value is used.

Using these data as a reference, we chose $1.54-0.01i$ as the value with which to model the refractive index of aerosols over White Sands. The sensitivity of calibration to refractive index will be analyzed in Chapter 6, using the range of refractive index values defined in Table 4.3. The error in using an averaged refractive index will thereby be assessed.

Vertical Distribution

Using standard nomenclature, as defined by the International Union of Geodesy and Geophysics in 1960, the atmosphere is divided vertically into four layers on the basis of temperature. These layers are the troposphere, stratosphere, mesosphere, and thermosphere. The tops of the layers are called, respectively, the tropopause, stratopause, mesopause, and thermopause. This stratification of the atmosphere is depicted in Fig. 4.2. The troposphere, or layer closest to the earth, contains three-fourths of the earth's air and nearly all the water vapor and atmospheric particles. On average, the temperature decreases in the troposphere at a lapse rate of -6.5°C/km. The tropopause is defined as that altitude where the lapse rate goes to zero. This occurs at approximately 11 km, but varies from greater

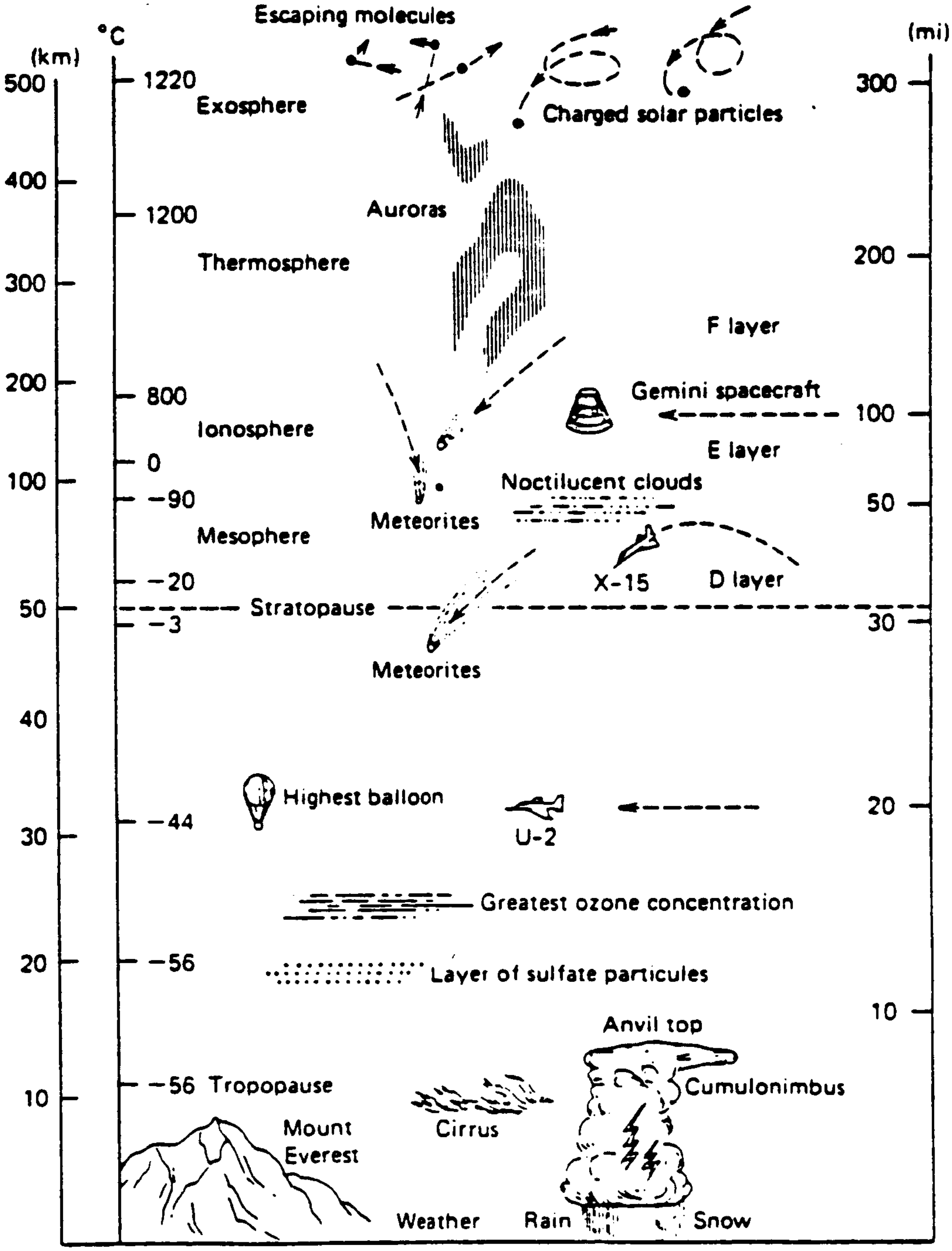

Figure 4.2 Stratification of the atmospheric envelope. From McCartney (1976).

than 16 km in the tropics to less than 9 km in the polar regions. The stratosphere continues next, to about 50 km. Between the tropopause and approximately 20 km, temperatures are constant, near -56°C. Temperatures then increase in the region of increased ozone, owing to an increased absorption of ultraviolet radiation from the sun.

The first 5 km of the atmosphere is a region of strong vertical mixing. This is attributed to factors such as heat transfer across the earth-air interface, winds, and turbulence created by local topography. The size distribution does not change much within this region, but both pressure and particle number density decrease exponentially with altitude. This decrease in particle concentration was measured, by Penndorf (1954), from the study of solar attenuation during eight aircraft flights. His measurements of Mie extinction with altitude were fit to an equation of the form

$$\beta_{Mie}(z,\lambda,V) = \beta_{Mie}(0,\lambda,V)\exp(-z/H_p) \ , \qquad (4.7)$$

where $\beta_{Mie}(0,\lambda,V)$ is the extinction at ground level, and the scale height H_p, found to vary from 1 to 1.4 km, was defined as having a representative average of 1.2 km. Recalling that extinction is related to particle number density through the cross section, and that cross section is assumed constant with altitude, particle concentration is also found to obey an exponential falloff, expressed in terms of the same scale height H_p.

A more generalized and often cited model of the vertical distribution of aerosols is that of Elterman (1968). This distribution is defined from an average profile measured under clear atmospheric conditions (estimated to be 23 km in visibility). The experimental setup is described in Elterman (1966). An intensity modulated searchlight beam was projected into the sky over White Sands, New Mexico. This site was at an elevation of 1.39 km. Synchronous detection at $\lambda =$ 0.55 μm was made 30.2 km away, from Sacramento Peak. Scattering data were obtained to 35 km altitude, at 1 km resolution. It was possible to obtain data to greater altitudes, but aerosol attenuation was considered negligible, and therefore not of interest in this region.

From December 1963 to April 1965, 119 extinction profiles were acquired. The last 79 of these were averaged to yield the vertical profile model. Earlier data were deleted so as to avoid including the unusually high values of stratospheric dust that were present as a result of the Mt. Agung volcanic eruption, March 1963. The Penndorf model was next used to extend the model from 3.7 km to sea level. Finally, a least square fit on data from 26 to 32 km was made, thus enabling the model to be extended to 50 km. This extinction model for aerosol scatterers is presented in Table 4.4, along with a molecular number density profile versus altitude. The latter is defined by the USSA (1962). These profiles, along with the ozone and water vapor profiles to be discussed later, are normalized and used within the Herman code. Here, the optical depth components are computed as a function of altitude, given optical depths at ground level. If the Elterman model of Mie extinction versus altitude is divided by the aerosol cross section at 0.55 μm, a number density profile can be obtained.

Table 4.4 Model Parameters of Mie Extinction and Molecular Number Density as a Function of Altitude

z (km)	β_{Mie} (km^{-1})	N_{Ray} (cm^{-3})	z (cm)	β_{Mie} (km^{-1})	N_{Ray} (cm^{-3})
0	1.58 E-01	2.547 E+19	26	3.62 E-04	7.123 E+17
1	6.95 E-02	2.311 "	27	2.77 "	6.092 "
2	3.00 "	2.093 "	28	2.12 "	5.214 "
3	1.26 "	1.891 "	29	1.63 "	4.466 "
4	6.66 E-03	1.704 "	30	1.25 "	3.828 "
5	5.02 "	1.531 "	31	9.55 E-05	3.283 "
6	3.54 "	1.373 "	32	7.31 "	2.818 "
7	3.29 "	1.227 "	33	5.60 "	2.406 "
8	3.39 "	1.093 "	34	4.29 "	2.056 "
9	3.25 "	9.712 E+18	35	3.29 "	1.760 "
10	3.17 "	8.598 "	36	2.52 "	1.509 "
11	2.97 "	7.585 "	37	1.93 "	1.296 "
12	3.12 "	6.486 "	38	1.48 "	1.116 "
13	2.88 "	5.543 "	39	1.13 "	9.620 E+16
14	2.82 "	4.738 "	40	8.66 E-06	8.308 "
15	2.65 "	4.049 "	41	6.64 "	7.187 "
16	2.52 "	3.461 "	42	5.08 "	6.227 "
17	2.49 "	2.959 "	43	3.89 "	5.404 "
18	2.41 "	2.529 "	44	2.98 "	4.697 "
19	2.03 "	2.162 "	45	2.28 "	4.088 "
20	1.49 "	1.849 "	46	1.75 "	3.564 "
21	1.08 "	1.574 "	47	1.34 "	3.112 "
22	8.13 E-04	1.341 "	48	1.03 "	2.738 "
23	6.22 "	1.144 "	49	7.86 E-07	2.418 "
24	4.93 "	9.760 E+17	50	6.02 "	2.135 "
25	4.15 "	8.335 "			

From Elterman (1968). All parameters defined at $\lambda = 0.55$ μm.

The Elterman data confirm the existence of a stratospheric dust layer at 20 km. This layer, observed by many other researchers, is a stable region of sulfate particles and sulfuric acid droplets. It is found over both urban and rural regions, and exists at an altitude approximately equal to that of greatest ozone concentration. In this layer the smaller particles rapidly decrease with altitude. Those of radius less than 0.1 μm are nonexistent near 20 km. The size distribution of larger particles, however, does not change greatly from that at lower altitudes.

Visibility

In order to model aerosol optical depths under a variety of atmospheric conditions, Elterman (1970) used visibility to compute atmospheric extinction at sea level. Visibility V, or meteorological range, is defined under sunlit conditions as the greatest horizontal distance at which an observer at ground level can distinguish a black object against the background sky. It is thus a subjective evaluation of the attenuation of contrast. As an observer looks along a horizontal path, contrast is reduced owing to direct sunlight, diffuse skylight, and ground reflected light scattered toward the observer. The observed contrast of an ideally black object, at distance V, is given as

$$C = -\exp(-\beta_{ext}\ V) \tag{4.8}$$

(a negative number, as the object is darker than the background, and as contrast is defined as the object minus background, divided by background radiance). Taking the visual threshold of perception as C = 0.02 (the lowest contrast at which an object can just be distinguished), extinction is determined as a function of visibility:

$$\beta_{Mie}(0,0.55,V) = 3.912/V - \beta_{Ray}(0.55)\ . \tag{4.9}$$

This expression was derived by noting that $-\ln(0.02) = 3.912$ and setting $\beta_{ext} = \beta_{Mie}+\beta_{Ray}$. The latter equality can be justified by assuming that absorption over distances on the order of the visual range V are negligible. The extinction that is defined in this manner is for a wavelength of 0.55 µm, the wavelength at which the eye is most sensitive, and for an altitude of $z = 0$ km. In practice, measuring visual range is an imprecise science, relying on the subjective opinion of the observer and requiring the presence of an object at a distance just equal to that at the extreme of visual perception. Nevertheless, it is useful in computing a model of optical depth τ_{Mie}, as is discussed next.

For altitudes above the mixing layer, taken as 5 km, Mie extinction is assumed independent of ground conditions, and hence visibility. At a wavelength of 0.55 µm this extinction is modeled by the data presented in Table 4.4. Conversely, at ground level extinction is determined directly from visibility by means of Eq. (4.9). For intermediate altitudes a scale height is computed to fit these boundary conditions. That is, from Eq. (4.7)

$$H_p = z/\ln[\beta_{Mie}(0,0.55,V)/\beta_{Mie}(z,0.55)] , \qquad (4.10)$$

where

$z = 5$ km

$\beta_{Mie}(0,0.55,V) = 3.912/V - \beta_{Ray}(0.55)$

$\beta_{Ray}(0.55) = 1.162\text{E-}02 \text{ km}^{-1}$

$\beta_{Mie}(5,0.55) = 5.02\text{E-}03 \text{ km}^{-1}$.

After scale height is computed, Mie extinction is determined for all altitudes below 5 km through use of Eq. (4.7) and for altitudes above 5 km through the measured Elterman data, Table 4.4. The Mie extinction is then integrated over all altitudes to yield the Mie optical depth at a wavelength of 0.55 μm:

$$\begin{aligned}\tau_{Mie}(0.55,V) &= \int_0^5 \beta_{Mie}(0,0.55,V)\exp(-z/H_p)\,dz \\ &\quad + \int_5^\infty \beta_{Mie}(z,0.55)\,dz \\ &= \beta_{Mie}(0,0.55,V)\,H_p[1-\exp(-5/H_p)] + \mathrm{B5INTEG}\ . \qquad (4.11)\end{aligned}$$

The first term in the solution is a function of visibility. The second term (B5INTEG) is the Elterman (1968) data integrated between $z = 5$ km and ∞. Figure 4.3 gives $\tau_{Mie}(0.55\ \mu m,V)$ as a function of visibility.

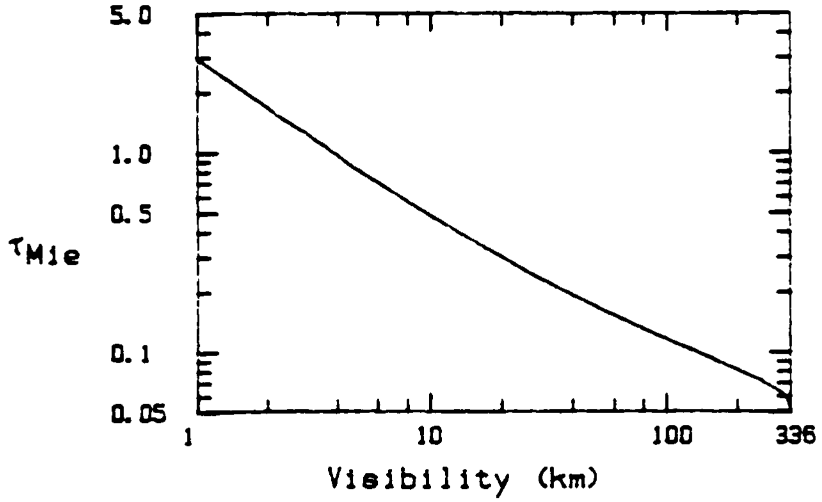

Figure 4.3 Mie optical depth as a function of visibility at a wavelength of 0.55 μm.

The haze/clear boundary, as defined by Elterman (1970), is 15 km.

Elterman next scaled this value of optical depth, using the data of Curcio, Knestrick, and Cosden (1961), to determine the spectral distribution of $\tau_{Mie}(\lambda,V)$. Denoting the extinction data reported by these authors as $\beta_c(\lambda)$, the Mie component of optical depth is found for an arbitrary wavelength:

$$\tau_{Mie}(\lambda,V) = \tau_{Mie}(0.55,V) \; \beta_c(\lambda)/\beta_c(0.55) \; . \qquad (4.12)$$

This is justified by the following argument. It is noted that the ratio of Mie cross sections (integrated over the normalized radial size distribution), $\sigma_{Mie}(\lambda)/\sigma_{Mie}(0.55\ \mu m)$, is independent of visibility. Extinction is related to meteorological conditions only through the number density, or $\beta_{Mie}(z,\lambda,V) = N_{Mie}(z,V)\ \sigma_{Mie}(\lambda)$. (This is an approximation, ignoring changes in radial size distribution and refractive index.) Thus,

$$\begin{aligned} \beta_{Mie}(0,\lambda,V) &= \beta_{Mie}(0,0.55,V) \; \sigma_{Mie}(\lambda)/\sigma_{Mie}(0.55) \\ &= \beta_{Mie}(0,0.55,V) \; \beta_c(\lambda)/\beta_c(0.55) \; . \qquad (4.13) \end{aligned}$$

That is, Mie extinction, at ground level and at a chosen wavelength, is determined from the product of extinction at $\lambda = 0.55\ \mu m$ with the ratioed Curcio data, $\beta_c(\lambda)/\beta_c(0.55\ \mu m)$. As before, Mie optical depth is determined from the integration of extinction with altitude. As extinction for the new wavelength scales as $\beta_c(\lambda)/\beta_c(0.55)$, a constant independent of altitude, so does optical depth.

For the $\tau_{Mie}(0.55,V)$ White Sands model we selected Elterman's model at 0.55 μm. We then used Ångström's formula, rather than the Curcio data, to determine τ_{Mie} at other wavelengths. This wavelength dependence will be found if the aerosols present follow a Junge radial size distribution, and we assumed such a distribution in our calibration. Hence, after determining $\tau_{Mie}(0.55,V)$ from Eq. (4.11), we determined other spectral τ_{Mie} by means of

$$\tau_{Mie}(\lambda,V) = \tau_{Mie}(0.55,V)\ (\lambda/0.55)^{-\nu+2}\ . \qquad (4.14)$$

To model clear-air conditions, we chose for the standard model a visibility of 100 km and $\nu = 2.5$. The resulting τ_{Mie} values are summarized in the bold type of Table 4.5. Also given are τ_{Mie} values for several other combinations of visibility and ν. The first column of this table gives the visibility and ν values; the following columns give τ_{Mie} at the reference wavelength of 0.55 μm and at the six reflective TM bands.

Molecular Absorbers

In the visible and near infrared wavelengths, water vapor, oxygen, and carbon dioxide are the primary atmospheric gases that produce strong absorption lines. Figure 4.4 shows how each of these contributes to atmospheric absorption for a vertical path. The extent of the Thematic Mapper (TM) bands is also given. From this figure it is apparent that ozone and water vapor are the primary absorbers whose effects will have to be accounted for in the calibration process. For this reason, this section focuses on these two gases.

Table 4.5 Summary of Model Parameters Defined for White Sands Missile Range

TM band		1	2	3	4	5	7
Wavelength (μm)	0.55	0.4860	0.5710	0.6610	0.8380	1.6800	2.2200
τ_{Ray} (Pressure, mbar)							
(800.00)	0.0776	0.1287	0.0666	0.0368	0.0141	0.0009	0.0003
(900.00)	**0.0873**	**0.1448**	**0.0749**	**0.0414**	**0.0159**	**0.0010**	**0.0003**
(1000.00)	0.0970	0.1609	0.0833	0.0460	0.0176	0.0011	0.0004
(1013.25)	0.0983	0.1630	0.0844	0.0466	0.0178	0.0011	0.0004
τ_{Mie} (Visibility, km/ν)							
(23/ 2.5)	0.2718	0.2891	0.2667	0.2479	0.2202	0.1555	0.1353
(23/ 3.0)	0.2718	0.3075	0.2618	0.2261	0.1784	0.0890	0.0673
(23/ 4.0)	0.2718	0.3480	0.2521	0.1881	0.1171	0.0291	0.0167
(100/ 2.5)	**0.1156**	**0.1230**	**0.1134**	**0.1054**	**0.0936**	**0.0661**	**0.0575**
(100/ 3.0)	0.1156	0.1308	0.1113	0.0962	0.0759	0.0378	0.0286
(100/ 4.0)	0.1156	0.1480	0.1072	0.0800	0.0498	0.0124	0.0071
(200/ 2.5)	0.0813	0.0865	0.0798	0.0742	0.0659	0.0465	0.0405
(200/ 3.0)	0.0813	0.0921	0.0784	0.0677	0.0534	0.0266	0.0202
(200/ 4.0)	0.0813	0.1042	0.0755	0.0563	0.0350	0.0087	0.0050
τ_{oz} (N_{oz} matm-cm)							
(212.0)	0.0195	0.0055	0.0231	0.0113	0.0013	0.0000	0.0000
(255.0)	**0.0235**	**0.0066**	**0.0277**	**0.0136**	**0.0016**	**0.0000**	**0.0000**
(298.0)	0.0274	0.0077	0.0324	0.0159	0.0018	0.0000	0.0000
(337.0)	0.0310	0.0087	0.0367	0.0180	0.0021	0.0000	0.0000
τ_{H_2O} (Water vapor, g cm^{-2} km^{-1})							
(0.010)	0.0000	0.0000	0.0000	0.0000	0.0006	0.0016	0.0010
(0.100)	**0.0000**	**0.0000**	**0.0000**	**0.0000**	**0.0057**	**0.0155**	**0.0101**
(0.590)	0.0000	0.0000	0.0000	0.0000	0.0335	0.0915	0.0594
(1.000)	0.0000	0.0000	0.0000	0.0000	0.0568	0.1551	0.1007
(10.000)	0.0000	0.0000	0.0000	0.0000	0.5678	1.5508	1.0068
τ_{CO_2}	**0.0000**	**0.0000**	**0.0000**	**0.0000**	**0.0000**	**0.0094**	**0.0035**

Model parameters are in bold type; extreme values, which are defined for sensitivity analysis, are in other rows. The optical depths are given at 0.55 μm, where τ_{Mie} is computed for a given visibility, as well as for the six reflective TM bands.

Aerosol characteristics:

Radial limits: R_{min} = 0.02 μm; R_{max} = 5.04 μm; ΔR = 0.04 μm
Refractive index: 1.54 - 0.01i

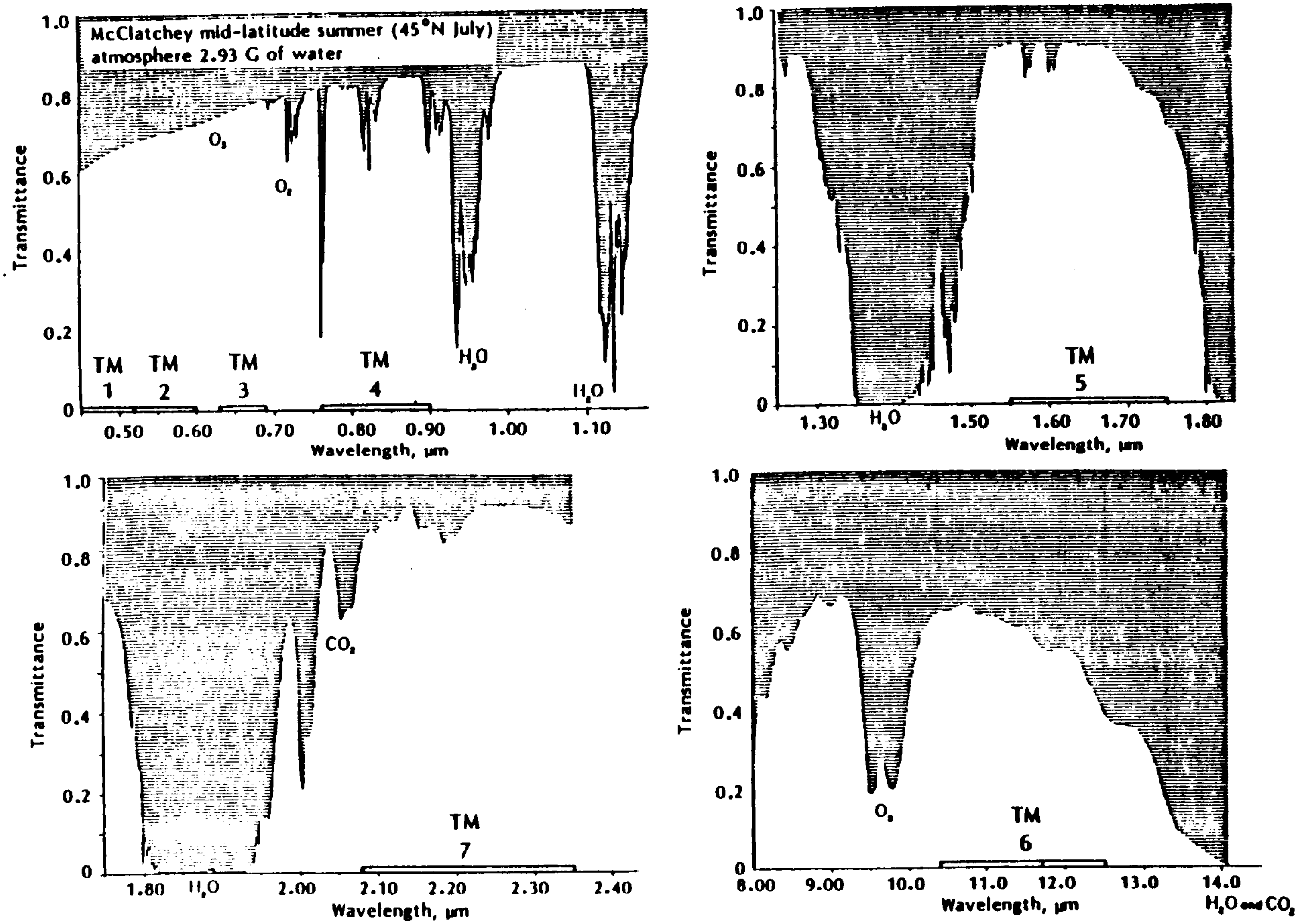

Figure 4.4 Absorption spectra for the principal absorbing gases in the earth's atmosphere.

From Kiang (1983).

Water vapor absorption becomes significant for wavelengths greater than 0.70 μm; carbon dioxide has absorption bands that overlap TM bands 5 and 7. In addition to these, there is significant ozone absorption from 0.4 to 0.9 μm, with a maximum near 0.6 μm. This is due to the Chappius bands, a term applied to this ozone continuum. Nitrogen dioxide also has continuum absorption from approximately 0.34 to 0.50 μm, with a maximum near 0.41 μm. The magnitude of NO_2 absorption is small and is ignored here.

Ozone

Ozone is a minor constituent but a principal absorber of solar radiation, responsible for the depletion of solar radiation between 0.2 and 0.3 μm. It is created primarily between altitudes of 20 and 30 km, where large numbers of oxygen molecules are dissociated by the absorption of ultraviolet radiation. The predicted columnar ozone content of the atmosphere is dependent on both season and latitude, as is shown in Fig. 4.5. Here, the average atmospheric content is plotted for four seasons as a function of latitude. An annual average is also defined, again dependent on latitude. The total amount of ozone is a maximum in spring and a minimum in autumn, with the largest amplitude of variation at high latitudes. For latitudes north of the tropic zone, seasonal variations are nearly sinusoidal. Measurements made over Tucson (King and Byrne, 1976) show that ozone can be expressed as

$$\begin{aligned} N_{oz} &= (255.3 \pm 4.0 \text{ matm-cm}) \\ &+ (42.6 \pm 5.0 \text{ matm-cm}) \sin(2\pi x - \phi) \,, \end{aligned} \qquad (4.15)$$

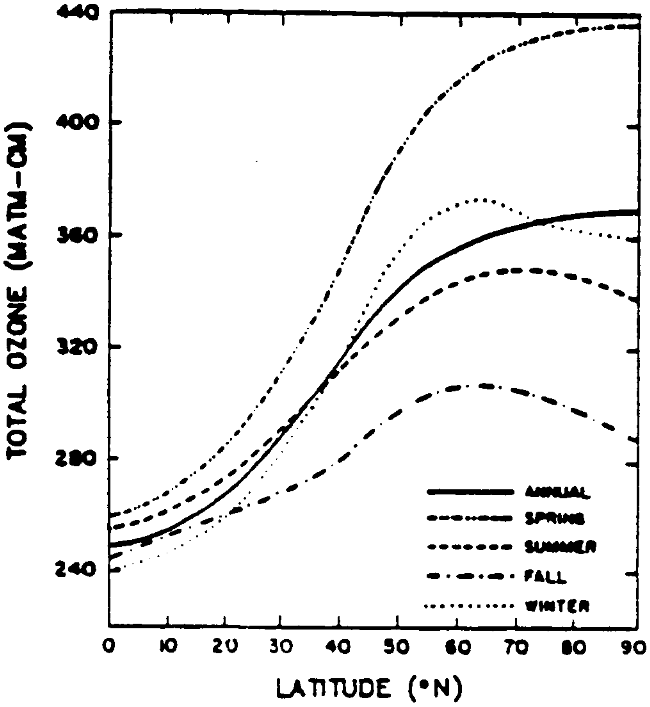

Figure 4.5 Columnar ozone as a function of latitude and season.

From London (1962).

where x is the fractional time of year and ϕ determines the time of year for the distribution peak. The maximum occurs about 23 April, the minimum about 23 October. Since White Sands is at roughly the same latitude as Tucson, this dependence is assumed an appropriate model for our test site.

The total ozone content of a vertical column of air is usually expressed in units of $(\text{matm-cm})_{STP}$. With an atmospheric ozone content of N_{OZ} atm-cm, where 1 atm-cm = 10^3 matm-cm, there would be N_{OZ} cm in height of pure absorber contained in a square centimeter at standard pressure (1013.25 mb) and temperature (273.15 K). Also, 1 atm-cm = 2.69 x 10^{19} molecules/cm, independent of the absorbing gas. Table 4.6 gives one model for the vertical distribution of ozone within the atmosphere. This particular profile is the low latitude profile measured under conditions in which the total ozone content was approximately 250 matm-cm. It was selected, from those defined by Mateer, DeLuisi, and Porco (1980), as the most appropriate with which to model White Sands. The original source of these data includes ozonesonde data archived by the World Ozone Data Centre, and ozonesonde data from the USAF ozonesonde network operated during the early 1960s. In the table, ozone content is defined for 34 atmospheric layers, where the atmospheric pressure at the base of a layer is $\sqrt{2}$ times the atmospheric pressure at the top of the layer. The base of the lowest layer is taken to be 1013.25 mbar, standard pressure.

The spectral dependence of ozone absorption is usually taken as that from Vigroux (1953). These data are based on laboratory measurements at 1013 mbar and 15°C. (The effects of temperature and pressure on the ozone absorption coefficient are considered small.) These absorption coefficients, as published in Elterman (1968), are listed in Table 4.7. To predict an optical depth for a given time of year, the product of number density, such as modeled by Eq. (4.15), and a spectral coefficient, as interpolated from Table 4.7, is determined:

$$\tau_{oz}(0,\lambda) = N_{oz}(0)\,\sigma_{oz}(\lambda) \quad . \qquad (4.16)$$

Table 4.6 Vertical Distribution of Ozone

Layer	Height (km)	Ozone amount for standard low latitude profile (matm-cm)
1	0.	3.96 E+00
2	2.8	3.47 "
3	5.5	2.93 "
4	8.0	2.41 "
5	10.3	1.80 "
6	12.5	1.78 "
7	14.7	2.50 "
8	16.9	7.11 "
9	19.1	1.74 E+01
10	21.3	2.75 "
11	23.6	3.48 "
12	25.9	3.71 "
13	28.1	3.36 "
14	30.5	2.67 "
15	32.8	1.83 "
16	35.2	1.21 "
17	37.7	7.47 E+00
18	40.2	4.30 "
19	42.8	2.31 "
20	45.5	1.21 "
21	48.3	6.31 E-01
22	60.0	3.30 "
23	53.6	1.72 "
24	56.2	9.00 E-02
25	58.8	4.70 "
26	61.4	2.46 "
27	64.0	1.28 "
28	66.6	6.71 E-03
29	69.2	3.51 "
30	71.3	1.83 "
31	73.3	9.58 E-04
32	75.3	5.01 "
33	77.3	2.62 "
34	79.3	2.86 "
Total ozone		250

Ozone amount per layer from Mateer, DeLuisi, and Porco (1980)

Pressure per layer defined from Pres(J) = 1013 $(\sqrt{2})^{J-1}$.

Height from interpolation of USSA pressure versus height (Table 4.8)

Table 4.7 Ozone Absorption as a Function of Wavelength

λ (μm)	σ_{oz} (cm^{-1})
0.27	210.
0.28	106.
0.30	101.
0.32	0.898
0.34	0.064
0.36	0.0018
0.38	0.
0.40	0.
0.45	0.0035
0.50	0.0345
0.55	0.092
0.60	0.132
0.65	0.062
0.70	0.023
0.80	0.01
0.90	0.

From Elterman (1968)

To compute the optical depth from measured parameters for a given wavelength and altitude,

$$\tau_{oz}(z,\lambda) = \tau_{oz}(0,\lambda_r)\,\frac{\sigma_{oz}(\lambda)}{\sigma_{oz}(\lambda_r)}\,\frac{N_{oz}(z)}{N_{oz}(0)}\ . \qquad (4.17)$$

The parameter $\tau_{oz}(0,\lambda_r)$ is that component of optical depth which is deduced from Langley plot measurements, at a radiometer wavelength of λ_r and at ground elevation, $z = 0$ km. The ratios $N_{oz}(z)/N_{oz}(0)$ and $\sigma_{oz}(\lambda)/\sigma_{oz}(\lambda_r)$ are determined from Tables 4.6 and 4.7, respectively.

Table 4.5 lists τ_{oz} for several values of the columnar number density N_{oz}. The model data (computed at $N_{oz} = 255$ matm-cm) are in bold type.

Water Vapor

The amount of water vapor that the atmosphere can contain depends on the air temperature. Below -40°C this amount is negligible. To quantify just how much is present, we used one of many functions of pressure, temperature, or density. Absolute humidity is defined by the actual partial pressure in millibars, or by the actual vapor density in g m^{-3}. Vapor pressure and density are related by $P = \rho RT$, where R is the specific gas constant of the gas in question (universal gas constant divided by the molecular weight of the gas). For water vapor, $R = 461.5$ J kg^{-1} K^{-1}, whereas for dry air $R = 287.06$ J kg^{-1} K^{-1}. Relative humidity is the ratio of actual vapor pressure, at a stated temperature, to the saturation value at that temperature. Other common parameters are mixing ratio and precipitable water. The mixing ratio is the mass of vapor contained in a unit mass of dry air; it is sometimes expressed in units of grams per kilogram. Precipitable water is the amount of water contained in a vertical air column of unit cross section.

The temperature measures of water vapor are the dewpoint, T_d, and frostpoint, T_f. Dewpoint is the temperature at which a given parcel of air would have to be cooled to reach saturation. Frostpoint is defined in the same way, except that saturation is with respect to ice.

In modeling the sensitivity of water vapor to the calibration process, we refer to variations in absorption in terms of water vapor density at ground level. The anticipated range of water vapor is determined from the expected range of late morning temperatures for the area. Figure 4.6 is used to convert these temperatures, at a given relative humidity, to water vapor density at sea level. From a temperature of -12°C and low humidity, to 20°C and high humidity, water vapor varies from approximately 0.01 to 1.0 g cm^{-2} km^{-1}. The vertical profile of water vapor is modeled after data from Sissenwine, Grantham, and Salmela (1968). These data, presented in Table 4.8, assume a density of 0.59 g cm^{-2} km^{-1} at ground level (corresponding to a temperature of 15°C and relative humidity of approximately 50%), and 1.417 g cm^{-2} for the integrated amount of water vapor throughout the atmosphere. (Since water vapor falls off exponentially, a scale height was defined for each layer, and then each layer was integrated over this exponential distribution.)

At the test site, relative humidity is usually measured by a psychrometer. This consists of two thermometers, one of which ("wet bulb") is covered with some material that is saturated with water. As water evaporates, the temperature of the wet bulb decreases. The difference in temperatures is related to the relative humidity. When radiosonde measurements are made, an electrical hygrometer is used. The hygrometer relies on the change in state of a material with moisture. A polystyrene slide, coated with a thin layer of a hydroxyethyl cellulose, is constructed with electrodes on each side. The electrical resistivity of the coating increases as the humidity increases.

In the Herman code, it is not the actual water vapor that is of interest, but the transmittance T at a given wavelength. This is expressed in terms of τ_{H_2O} for water vapor (recall $T = \exp(-\tau)$). To

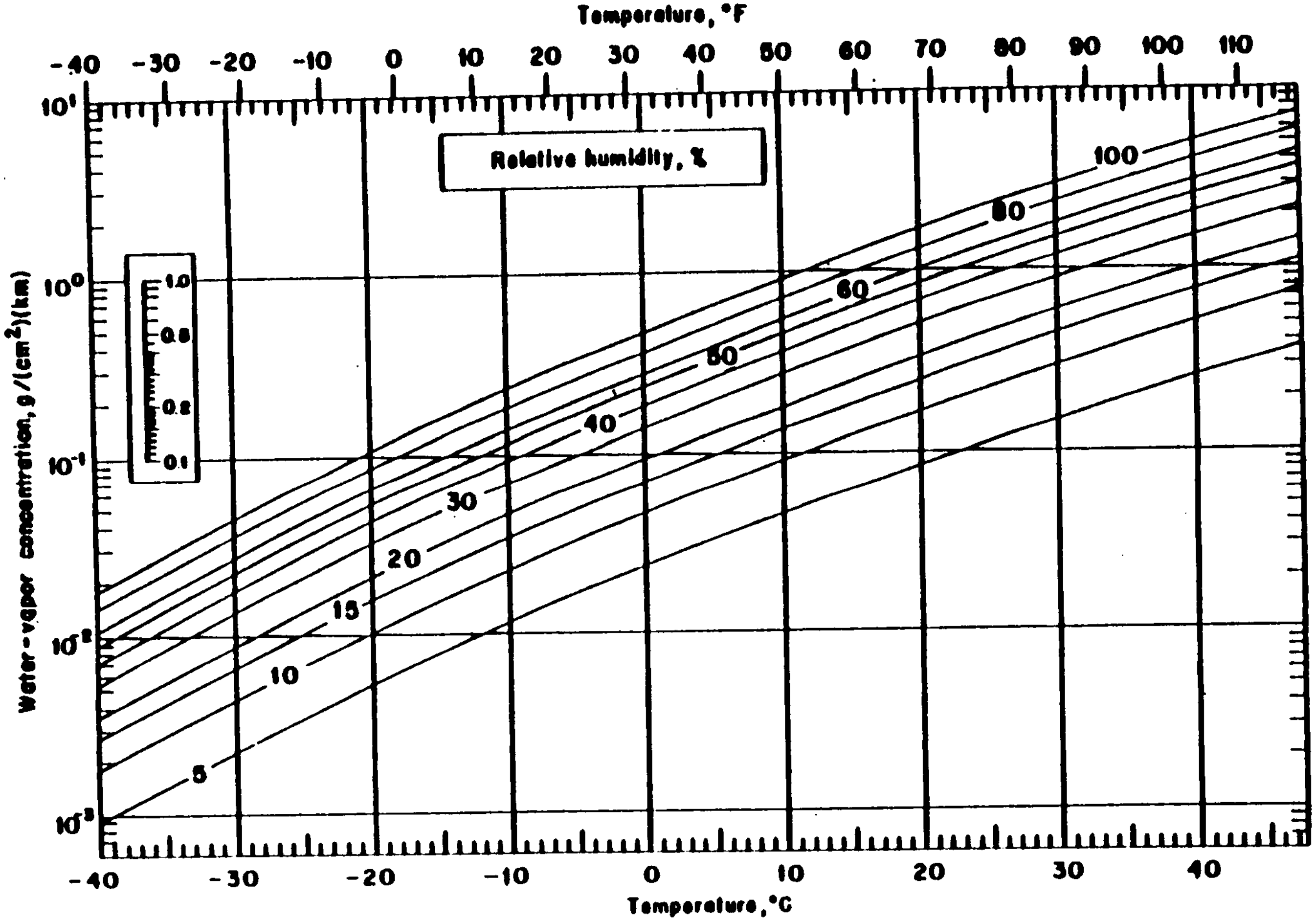

Figure 4.6 Water vapor concentration per kilometer path length as a function of temperature and relative humidity.

From McClatchey et al. (1972).

Table 4.8 Model Vertical Profiles of Pressure, Temperature, and Water Vapor for U.S. Standard Atmosphere

Height (km)	Pressure (mbar)	Temp (K)	Density (g/m^3)	Water vapor (g/m^3)
0	1.013 E+03	288.1	1.225 E+03	5.9 E+00
1	8.986 E+02	281.6	1.111 "	4.2 "
2	7.950 "	275.1	1.007 "	2.9 "
3	7.012 "	268.7	9.093 E+02	1.8 "
4	6.166 "	262.2	8.193 "	1.1 "
5	5.405 "	255.7	7.364 "	6.4 E-01
6	4.722 "	249.2	6.601 "	3.8 "
7	4.111 "	242.7	5.900 "	2.1 "
8	3.565 "	236.2	5.258 "	1.2 "
9	3.080 "	229.7	4.671 "	4.6 E-02
10	2.650 "	223.2	4.135 "	1.8 "
11	2.270 "	216.8	3.648 "	8.2 E-03
12	1.940 "	216.6	3.119 "	3.7 "
13	1.658 "	216.6	2.666 "	1.8 "
14	1.417 "	216.6	2.279 "	8.4 E-04
15	1.211 "	216.6	1.948 "	7.2 "
16	1.035 "	216.6	1.665 "	6.1 "
17	8.850 E+01	216.6	1.423 "	5.2 "
18	7.565 "	216.6	1.216 "	4.4 "
19	6.467 "	216.6	1.040 "	4.4 "
20	5.529 "	216.6	8.891 E+01	4.4 "
21	4.729 "	217.6	7.572 "	4.8 "
22	4.047 "	218.6	6.451 "	5.2 "
23	3.467 "	219.6	5.500 "	5.7 "
24	2.972 "	220.6	4.694 "	6.1 "
25	2.549 "	221.6	4.008 "	6.6 "
30	1.197 "	226.5	1.841 "	3.8 "
35	5.746 E+00	236.5	8.463 E+00	1.6 "
40	2.871 "	250.4	3.996 "	6.7 E-05
45	1.491 "	264.2	1.966 "	3.2 E-06
50	7.978 E-01	270.6	1.027 "	1.2 "
70	5.520 E-02	219.7	8.754 E-02	1.5 E-07
100	3.008 E-04	210.0	4.989 E-04	1.0 E-09

From McClatchey et al. (1972, Table B1), who report pressure, temperature, and density from USSA (1972) and water vapor profile from Sissenwine et al. (1968).

model transmittance for atmospheric gases, the LOWTRAN 6 (Kneizys et al., 1983) computer code was run. After integration between the equivalent TM bandpasses, as computed by Palmer (1984), an average τ_{H_2O} value was determined for TM bands 4, 5, and 7. These were found to be 0.0335, 0.0915, and 0.0594, respectively. (The corresponding values that characterize carbon dioxide absorption were τ_{CO_2} = 0.0, 0.0094, and 0.0035.) The range of predicted τ_{H_2O} values for White Sands was computed by scaling these τ_{H_2O} values by the ratio $\rho_{H_2O}(0,RH,T)/0.59$, where the water content at White Sands may vary between $\rho_{H_2O}(0,RH,T) = 0.01$ and 1.0 g cm^{-2}. The resulting τ_{H_2O} values are summarized in Table 4.5. To compute the band-averaged radiance incident on a sensor, radiances must, in general, be computed over small wavelength intervals of constant optical depth and then averaged. Because water vapor absorption varies rapidly with wavelength, it is difficult to define such intervals and the τ_{H_2O} parameters associated with them. However, the TM bands are selected to avoid regions of strong water vapor absorption, and τ_{H_2O} is therefore small. Any integrals over $\exp(-\tau)$ can be approximated as integrals over terms linear in τ. This justifies the use of a band-averaged water vapor optical depth for use in the radiative transfer code.

Currently, the amount of water vapor present in the atmosphere, for the days of the Landsat overpass, is determined from measured relative humidity, temperature, and Fig. 4.6. It is hoped that within the near future this technique will be replaced by a direct measurement of τ, made with filters matched to TM bands 5 and 7. This will be done with the solar radiometer and Langley plot technique, thereby removing many uncertainties associated with use of LOWTRAN transmittance spectra and the scaling technique.

Solar Irradiance

To compute the spectral radiance incident on an in-orbit sensor, it is necessary to know the exoatmospheric solar spectral irradiance to a high level of certainty. This quantity is defined as the irradiance 1 astronomical unit (AU) from the sun, within a specified wavelength interval, striking a unit surface in free space perpendicular to the sun's rays (and with units such as W cm^{-2} μm^{-1}). This parameter can be measured directly by using a solar spectral radiometer. The irradiance data, when extrapolated to zero air mass, yield values for the spectral exoatmospheric irradiance. This, the Langley plot technique, is discussed in Chapter 5. For such data to be reliable, the radiometer must be calibrated to an acceptable absolute accuracy, if possible to the 1% level. In addition, a temporally stable and spatially homogeneous atmosphere is required. Because of these constraints, we have chosen to rely on published data, for we feel they are more accurate than we can presently measure at White Sands.

Published solar irradiance data are for a mean earth-sun distance of 1 astronomical unit, where 1 AU = 1.496×10^8 km. Variations of this distance throughout the year result in variations of solar irradiance by as much as 6.7%. The minimum earth-sun distance is about 0.98327 AU, occurring about January 3. The maximum distance of 1.01673 AU occurs about July 4. Ephemeris tables, such as the

American Ephemeris and Nautical Almanac (published yearly), can be consulted for the exact distance for a given day of the year. Conversely, mathematical expressions exist from which this distance can be computed. For example, an expression developed by Spencer (1971) gives the eccentricity of the earth's orbit to an error of less than 0.0001. This expression is

$$(r_{\circ}/r)^2 = 1.000110 + 0.34221 \cos\Gamma + 0.001280 \sin\Gamma + 0.000719 \cos(2\Gamma) + 0.000077 \sin(2\Gamma) \,. \quad (4.18)$$

The parameter Γ is called the day angle. It has units of radians, and is given by

$$\Gamma = 2\pi(d-1)/365 \quad (4.19)$$

where d is the day number of the year (d = 1 for January 1; d = 365 for December 31).

Several solar irradiance data sets have been reported. The work of Neckel and Labs (1984) is the most detailed. They report a mean error of 1.5% in the uv, and 1% in the visible. These data are based upon measurements made early in the 1960s, in Switzerland, at an altitude of 3.6 km (11,800 ft). The calculation of determining mean disk irradiance, based upon disk center measurements, has been revised from the 1981 publication. In 1974, the American Society for Testing and Materials (ASTM) accepted the data reported by Thekaekara, Kruger, and Duncan (1969) as its recommended engineering standard. These data, often referred to as the NASA/ASTM standard, were obtained from measurements carried out by NASA during the period 1968-1971 from a Convair research aircraft and are thought to be accurate only to within 5%.

Currently, we use in our Landsat calibration program the data recommended by Frohlich (1983), as published by Iqbal (1983). They are presented here in Table 4.9. Values such as those published by Neckel and Labs, Thekaekara, Arvesen, and others were combined. They were then adjusted to an integrated value of 1367 W m^{-2}, the solar constant as proposed by the World Radiation Center (WRC). The World Meteorological Organization adopted this spectrum as the best available, in 1981. It is referred to as the WRC standard.

The solar constant defines the total amount of irradiance from the sun that falls at the top of the earth's atmosphere at its mean distance from the sun. It is the value of spectral irradiance, integrated over all wavelengths, and measured in units such as W m^{-2}. The solar output can be approximated by treating the sun as a blackbody with peak spectral exitance near 0.5 μm, corresponding to a 6000 K blackbody curve. In actuality, the effective temperature of the sun is wavelength dependent (Slater, 1980), and the true spectrum is by no means smooth at high spectral resolution because of Fraunhofer absorption lines.

The solar constant can be determined with greater certainty than spectral irradiance values. For high accuracy, measurements from high altitude or from orbit are invaluable since atmospheric attenuation cannot be exactly corrected for. The actual solar constant seems to fluctuate slightly, but by only a few tenths of a percent

Table 4.9 Extraterrestrial Solar Spectral Irradiance at Mean Sun-Earth Distance (WRC Spectrum)

λ (μm)	E_0 (W/m^{2}μm)	λ (μm)	E_0 (W/m^{2}μm)	λ (μm)	E_0 (W/m^{2}μm)	λ (μm)	E_0 (W/m^{2}μm)
0.250	64.56	0.460	2032.49	0.730	1355.00	1.750	187.00
0.255	91.25	0.465	2000.00	0.740	1300.00	1.800	170.00
0.260	122.50	0.470	1979.99	0.750	1272.52	1.850	149.01
0.265	253.75	0.475	2016.25	0.760	1222.50	1.900	136.01
0.270	275.00	0.480	2055.00	0.770	1187.50	1.950	126.00
0.275	212.50	0.485	1901.26	0.780	1195.00	2.000	118.50
0.280	162.50	0.490	1920.00	0.790	1142.50	2.100	93.00
0.285	286.25	0.495	1965.00	0.800	1144.70	2.200	74.75
0.290	535.00	0.500	1862.25	0.810	1113.00	2.300	63.25
0.295	560.00	0.505	1943.75	0.820	1070.00	2.400	56.50
0.300	527.50	0.510	1952.50	0.830	1041.00	2.500	48.25
0.305	557.50	0.515	1835.01	0.840	1019.99	2.600	42.00
0.310	602.51	0.520	1802.49	0.850	994.00	2.700	36.50
0.315	705.00	0.525	1894.99	0.860	1002.00	2.800	32.00
0.320	747.50	0.530	1947.49	0.870	972.00	2.900	28.00
0.325	782.50	0.535	1926.24	0.880	966.00	3.000	24.75
0.330	997.50	0.540	1857.50	0.890	945.00	3.100	21.75
0.335	906.25	0.545	1895.01	0.900	913.00	3.200	19.75
0.340	960.00	0.550	1902.50	0.910	876.00	3.300	17.25
0.345	877.50	0.555	1885.00	0.920	841.00	3.400	15.75
0.350	955.00	0.560	1840.02	0.930	830.00	3.500	14.00
0.355	1044.99	0.565	1850.00	0.940	801.00	3.600	12.75
0.360	940.00	0.570	1817.50	0.950	778.00	3.700	11.50
0.365	1125.01	0.575	1848.76	0.960	771.00	3.800	10.50
0.370	1165.00	0.580	1840.00	0.970	764.00	3.900	9.50
0.375	1081.25	0.585	1817.50	0.980	769.00	4.000	8.50
0.380	1210.00	0.590	1742.49	0.990	762.00	4.100	7.75
0.385	931.25	0.595	1785.00	1.000	743.99	4.200	7.00
0.390	1200.00	0.600	1720.00	1.050	665.98	4.300	6.50
0.395	1033.74	0.605	1751.25	1.100	606.04	4.400	6.00
0.400	1702.49	0.610	1715.00	1.150	551.04	4.500	5.50
0.405	1643.75	0.620	1715.00	1.200	497.99	4.600	5.00
0.410	1710.00	0.630	1637.50	1.250	469.99	4.700	4.50
0.415	1747.50	0.640	1622.50	1.300	436.99	4.800	4.00
0.420	1747.50	0.650	1597.50	1.350	389.03	4.900	3.75
0.425	1692.51	0.660	1555.00	1.400	354.03	5.000	3.47
0.430	1492.50	0.670	1505.00	1.450	318.99	6.000	1.75
0.435	1761.25	0.680	1472.50	1.500	296.99	7.000	0.95
0.440	1755.02	0.690	1415.02	1.550	273.99	8.000	0.55
0.445	1922.49	0.700	1427.50	1.600	247.02	9.000	0.35
0.450	2099.99	0.710	1402.50	1.650	234.02	10.000	0.20
0.455	2017.51	0.720	1355.00	1.700	215.00	25.00	0.12

From Iqbal (1983)

over many years. The Solar Maximum Mission satellite measured solar variability to be no larger than 0.2%, although the average solar variability was 0.05%. The NASA value of the solar constant, adopted in 1971 as its design standard, is 1353 ± 21 W m^{-2}. The WRC standard, 1367 ± 2 W m^{-2}, differs from the NASA value by only 1%. The latter value of the solar constant has been defined by Frohlich (1983) and is based on data recorded from 1969 to 1980. It accounts for many changes in the state of the art. For example, only since 1975 has it been known that some instrument characteristics are different in the vacuum of space, as compared to terrestrial characteristics. Furthermore, recent measurements employ more accurate cavity-type absolute instruments.

CHAPTER 5

IN-FLIGHT ABSOLUTE CALIBRATION METHODOLOGY

To achieve the absolute calibration of the Landsat-TM sensor, measurements are made on the morning of the TM overflight. These are the measurements needed to characterize the atmosphere and surface reflectance over a given test site and are used as inputs to the Herman radiative transfer code. The output of this code gives us the radiance that was incident at the entrance pupil of the TM for each of the TM spectral bands. These radiance values are compared to the TM output digital counts from the detectors that sampled the radiometrically measured ground area, to yield the calibration constant.

This chapter gives details of the first two calibrations, of January 3, 1983, and July 8, 1984. As the first calibration involved a Landsat 4 sensor and the second a Landsat 5 sensor, no insight can be gained as to the stability of the TM responsivity in orbit. The purpose of these initial calibrations is to define and evaluate our initial analysis procedures and estimate any large changes in responsivity from the preflight calibration.

Data Reduction of Atmospheric Measurements

The previous chapter gave a theoretical view of the Herman radiative transfer code. Required inputs are: model radial size distribution (Junge, log normal, or that from an inversion), distribution adjustable parameters (such as Junge ν or log normal σ), radial distribution size limits, aerosol refractive index (both real and imaginary), surface reflectance, solar zenith angle at the time of image acquisition, and the optical depths τ_{Mie}, τ_{Ray}, τ_{oz}, and τ_{H_2O}. Of these inputs the optical depth components and Junge ν (assuming this distribution) can be determined from solar irradiance measurements. These data are acquired throughout the morning of the overpass. Initially, τ_{ext} is determined from the negative of the slope of the log irradiance versus air mass curve. This is called the Langley technique. This and the techniques used to extract the component τ values are summarized below.

Langley Plots

Total atmospheric extinction through a vertical path in the atmosphere can be determined with use of a ground-based solar radiometer. The technique is based on the assumption that the transmission of the direct solar flux can be expressed from Beer's law

$$E = E_0 \exp(-\tau_{ext}\ m) \qquad (5.1)$$

where E is the transmitted solar irradiance at wavelength λ, and E_0 is the spectral irradiance outside the earth's atmosphere. The spectral extinction optical depth τ_{ext} describes the attenuation of solar flux along a vertical path through the atmosphere, and the relative air mass m accounts for the slant path when the sun is at a given solar zenith angle. The expression is valid as long as the absorption is unsaturated, and temporal and spatial homogeneity are assumed.

After E is observed at different times of the morning (hence, different air masses), a plot of ln E versus m is made. This is termed a Langley plot (Langley, 1881). The data are fit to a straight line, represented by the equation

$$\ln E = \ln E_{\circ} - \tau_{ext}\, m \tag{5.2}$$

of slope $-\tau_{ext}$ and intercept $E_{\circ}$ (at $m = 0$).

The optical air mass m is the weighted ratio of the path length through the earth's atmosphere toward the sun, divided by the path length to the zenith. In analytic form it is

$$m = \frac{\int_0^{\infty} \rho(s)\, ds}{\int_0^{\infty} \rho(z)\, dz} \; . \tag{5.3}$$

Several commonly used expressions give air mass as a function of the solar zenith angle. To a first approximation it is given by $m = \sec \theta_z$, where θ_z is the solar zenith angle. For $\theta_z < 60°$ this expression is good to within 0.25%. At larger angles refraction and the curvature of the earth must be accounted for. More complex expressions are then used. These equations are empirical fits to the air mass values computed using a given data base for the atmospheric density. Kasten (1964) derived one such empirical formula to compute air mass as a function of apparent solar elevation angle, β'. He used the 1959

ARDC Model Atmosphere (Minzner, Champion, and Pond, 1959), which was known to 84 km. A refractive index of $n_0 = 1.000276$, taken for 15°C, 1013.25 mbar, and $\lambda = 0.7$ µm, was assumed. This wavelength was chosen because it divides the solar spectrum into two parts of equal energy. The data were fit to an equation of the form

$$m = [\sin\beta' + a(\beta' + b) - c]^{-1} \tag{5.4}$$

with $a = 0.15$, $b = 3.885$, and $c = 1.253$. Winker (1980) has compared this expression with two others that are commonly used: the Kasten formula, with coefficients fitting Bemporad's (1907) atmospheric sounding data, and Rozenberg's (1966) formula $m = [\cos\theta_z + 0.025 \exp(-11 \cos\theta_z)]^{-1}$. He computed optical depths from solar irradiance data and found differences of less than 0.5%, as long as data from large solar zenith angles were excluded. For this reason it is recommended that data be fit only between the limits $1 \leq m \leq 6.5$.

Even if data acquired at large air masses are excluded, some uncertainty exists in determining τ_{ext} and E_0 as a result of temporal fluctuations of the atmosphere. From Eq. (5.2) it can be shown that a fluctuation of τ_{ext} will result in a change of E, given by

$$|\Delta(\ln E)| = m \, \Delta\tau_{ext} . \tag{5.5}$$

Thus, random deviations of τ_{ext} will cause deviations of ln E from a straight line, these deviations increasing with increasing air mass. A simple least-squares fit to the data, as is usually used, will give more weight to data that are less reliable, that is, those at a larger air mass.

To remedy this problem, Young (1974) and Herman et al. (1981) have proposed that the Langley plot data be weighted during the reduction, to give equal weight to all data points. The formula derived by Herman and coworkers is developed by assuming that τ_{ext} varies in a purely random fashion throughout the period of measurement. This weighted least-squares solution is

$$\ln E_0 = \frac{N \sum (\ln E_n)/m_n^2 - \sum (\ln E_n)/m_n \sum 1/m_n}{N \sum 1/m_n^2 - (\sum 1/m_n)^2} \qquad (5.6)$$

where the summation is taken over N observations. An instantaneous optical depth is calculated for each observation

$$\tau_n = \frac{\ln E_0 - \ln E_n}{m_n} \qquad (5.7)$$

from which the average optical depth is computed

$$\bar{\tau} = \frac{1}{N} \sum \tau_n \, . \qquad (5.8)$$

This weighting technique should provide more accurate values of atmospheric extinction and the intercept E_0, provided there is not a systematic temporal change in τ_{ext}. On days that are systematically changing, neither method will be reliable.

In practice, τ_{ext} is computed from our solar irradiance measurements using a computer program called LNGPLT.REA. Initially the software was written by Reagan (1983) and was called ATSHRT. We have modified the code to process ephemeris data to the nearest second (before data were truncated to the nearest minute), modified the refractive correction in computing air mass, and generated software to plot the resulting Langley plots on a local system (IBM PC and Hewlett Packard 7470A plotter). Also, we have made extensive modifications to run the code with the newer solar radiometer, built for this program under NASA support.

The code determines air mass from the time of day at which a measurement was made. The zenith angle is first determined from the expression

$$\cos\theta_z = \sin\phi \sin\delta + \cos\phi \cos\delta \cos h \tag{5.9}$$

where ϕ is the observer latitude, δ the solar declination, and h the local solar hour angle. A refraction correction, $\Delta\theta$ (derivation unknown),

$$\Delta\theta = \frac{0.0001953\,\theta^2}{93.389 - \theta} \tag{5.10}$$

is subtracted from the ephemeris-derived zenith angle to give the apparent zenith angle as seen from the earth's surface. Kasten's expression is then used to compute air mass. The air mass versus ln E data are weighted in the manner discussed above.

Instrumentation

Two solar radiometers, shown in Fig. 5.1, are used at our test site to acquire Langley plot data. The first instrument is on loan to us from Dr. John Reagan, Department of Electrical and Computer Engineering. (Actually one of two available Reagan radiometers is used; the instruments are almost identical in construction.) The principles of its construction are given in Shaw et al. (1973). Ten narrowband spectral filters are used, each 10 nm wide. These interference filters are spaced approximately uniformly in the visible region between 0.4 and 0.8 μm. The radiometer is mounted on a camera tripod and is manually pointed at the sun; the filter wheel is manually rotated through the 10 filter positions, and data from the output voltmeter are manually recorded. For these reasons the instrument must be manned by two people during data collection. Before each data set the instrument is aligned, then cycled through the spectral filter wheel positions. A start and finish time is recorded, along with the gain settings. At large air masses, data are recorded every minute or two, decreasing to about one data set every 15 minutes toward noon. It takes approximately 30 seconds to cycle through the filter wheel and record all data. Approximately 100 data sets (each with data from the 10 filter positions) are recorded.

For the January 3 calibration, the Reagan radiometer was the only instrument available to us. The Reagan instrument is still used

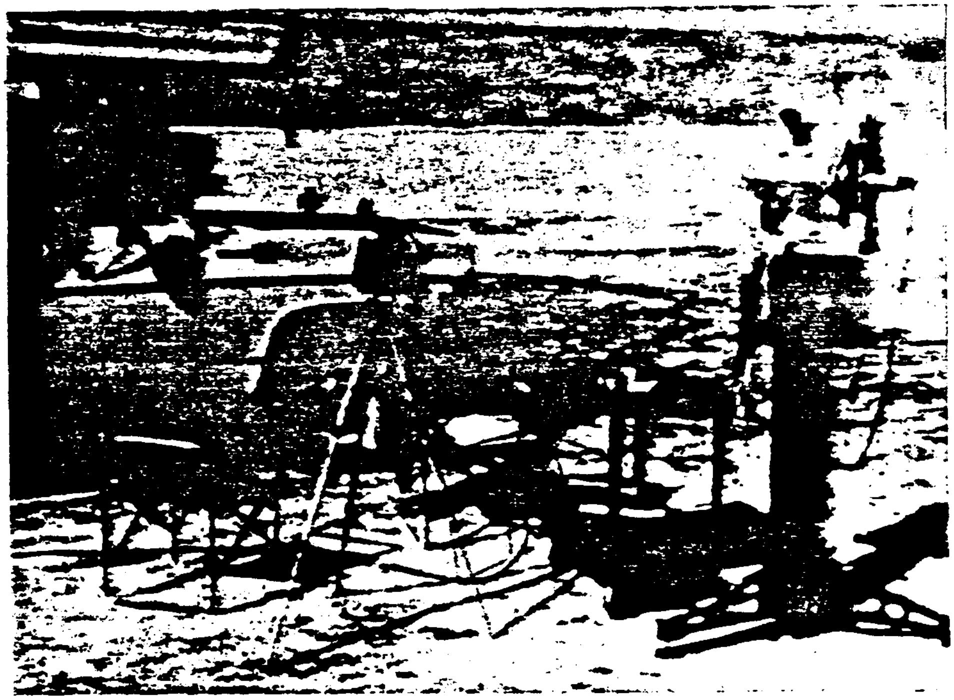

Figure 5.1 Reagan solar radiometer and Castle spectropolarimeter.

Manually operated Reagan instrument is to the left, automated spectropolarimeter to the right.

on all observations, as it is reliable and allows us to collect backup data should there be problems with the newer automated solar radiometer.

By the July 8, 1984, calibration, an automated instrument, the Castle spectropolarimeter, had been built. (Two instruments were actually built, one to be used in a solar radiometer mode, the other to record data from helicopter altitudes for verification of our techniques.) This instrument is also shown in Fig. 5.1, and details of its design are given in Castle (1985). For the visible measurements a silicon detector is used, along with 10 spectral filters. Although the filter wavelengths are slightly different from those of the Reagan radiometer, the principles used in their selection are the same. The Castle instrument is controlled by a TRS-80 Model 100 computer. It automatically tracks the sun, cycles through the filter set, and records data. To increase the dynamic range of the instrument, one of four neutral density filters is automatically positioned. Data are recorded in orthogonal polarizations; it is hoped that this polarization data will be useful in the future to assist in the characterization of atmospheric aerosols.

To determine optical depths, an absolute calibration of the solar radiometers is not required. The Castle spectropolarimeters are calibrated in an absolute sense, however, so that they may be used in the helicopter mode of operation where the measured upwelling radiance is compared to predicted radiances. Whether or not the instruments are calibrated, it is recommended (Reagan et al., 1984) that an accurate measure of V_0 be obtained (the voltage intercept, V_0, obtained from the Langley plot extrapolated to zero air mass). This allows the instantaneous optical depth to be determined with greater accuracy. The method for determining V_0 is to determine the zero air mass voltages from measurements made on clear, stable days, at clean observation sites. It is estimated that the error in measuring V_0 in this fashion is less than a few tenths of a percent. Instrument calibration is found to be stable over a period of months to a year.

Optical Depth Components

The extinction optical depth, τ_{ext}, is composed of three components

$$\tau_{ext} = \tau_{Mie} + \tau_{Ray} + \tau_{abs} , \tag{5.11}$$

as discussed in Chapter 2. Each has a wavelength dependence. The component τ_{abs} is in turn attributed to ozone, water vapor, carbon dioxide, and other absorbing gases. The Rayleigh component is most easily characterized, having the pressure and wavelength dependence given in Eq. (3.40). Mie optical depths are determined by subtracting the τ_{Ray} component from the total optical depth, at wavelengths outside the Chappius ozone band and water vapor absorption regions. By fitting these discrete points to a curve, one can define the complete τ_{Mie} versus wavelength dependence. Following King and Byrne (1976), this curve is defined as

$$\log \tau_{Mie} = a_0 + a_1 \log\lambda + a_2 (\log\lambda)^2 , \tag{5.12}$$

with the adjustable constants a_0, a_1, and a_2 determined from a least-squares fit to the data. The ozone component of optical depth is then determined from $\tau_{oz} = \tau_{ext} - \tau_{Ray} - \tau_{Mie}$ at the wavelength of maximum ozone absorption, amongst those wavelengths covered by the solar radiometer. The spectral dependence of τ_{oz} follows from this information and a knowledge of the ozone absorption coefficient.

In the calibrations reviewed here, a Junge radial size distribution is assumed. For the January 1983 calibration, the model parameter $\nu = 2.5$ was used to characterize the particle size versus radius slope (see Eq. (4.4)). By July 1984 our procedure had changed. The Junge ν parameter was then determined from the slope of the log τ_{Mie} versus log λ curve. Eventually, we hope to explore the use of inversion techniques in determining radial size distributions (King et al., 1978).

In the two calibrations reported here, τ_{H_2O} is determined from a knowledge of the relative humidity and temperature during the time of the Landsat overpass. These quantities are used to scale τ_{H_2O}, as predicted from LOWTRAN and the U.S. Standard Atmosphere. (Further details of the procedure are given in Chapter 4.) In future calibrations the Castle spectropolarimeter will be equipped with a spectral filter matched to TM band 5. Thus the water vapor optical depth can be measured directly.

Test Site Selection

We selected the flat gypsum area within the White Sands Missile Range, New Mexico, as our primary test site. The gypsum sand area covers an area of 30 x 30 km, and its uniformity and Lambertian characteristics aid in the characterization of the surface reflectance. White Sands is at an elevation of about 1219 m (4000 ft) and has many clear days in which aerosol loading is low, thus reducing the uncertainties that result from errors in characterizing aerosol properties. Because of the high reflectance of the sands, a large component of the radiance viewed by Landsat is due to direct reflection. This reduces the errors in accounting for multiple scattering effects. Finally, by selecting this area, we have the support of the U.S. Army's Atmospheric Science Laboratory (ASL). This lab can provide meteorological data, such as site relative humidity and temperature data, and has provided radiosonde data upon request.

The equipment used to characterize the gypsum reflectance has been a Barnes modular multispectral radiometer (MMR). Readings are taken at the pixel centers of a 4 x 4 pixel test area (each pixel being 30 m on a side). In calibrations following that of July 1984, the use of helicopter photography has been investigated (Capron, 1985) in order to better characterize an extended area of the test site. Future plans call for the angular distribution of reflectance to be measured at the site.

Reflectance

The nomenclature, measuring geometry, and techniques associated with determining the reflectance of a given surface are quite varied. With this in mind, the technical basis of our measurements at White Sands is presented here. Because we are interested in the directional properties, as well as the magnitude, of the reflectance at the field site, we determine the reflectance factor. Reflectance factor and other quantities are defined below. A spectral dependence is assumed for each quantity. All of our reflectance measurements are made with finite spectral bandwidths. These are, in general, the 40-nm bandwidths of a laboratory radiometer, or those bandwidths associated with the Thematic Mapper and the Barnes modular multispectral radiometer.

Definitions and Nomenclature

Reflectance factor, $R(\theta,\phi;\theta',\phi')$, unitless: Ratio of the flux reflected by a sample surface to that which would be reflected into the same beam geometry by a lossless, Lambertian surface that is identically irradiated. Thus,

$$R(\theta,\phi;\theta',\phi') = \frac{\int_{\mathrm{IFOV}} L_t(\theta',\phi') \cos\theta' \sin\theta' \, d\theta' \, d\phi'}{\int_{\mathrm{IFOV}} L_p(\theta',\phi') \cos\theta' \sin\theta' \, d\theta' \, d\phi'} \tag{5.13}$$

is the reflectance factor measured with a detector having a given instantaneous field of view (IFOV). L_t is the radiance reflected off the sample target, and L_p is the radiance reflected off a perfect (lossless), diffuse surface. The incident beam originates from (θ,ϕ), and the reflected beam is viewed in the direction (θ',ϕ').

Reflectance, ρ, unitless: Ratio of the reflected flux to the incident flux. When referring to this parameter one needs to specify if the flux is integrated over the reflecting hemisphere, or if the reflected flux is measured within a given cone angle. The hemispherical reflectance can be related to the reflectance factor by

$$\rho = \int_{2\pi}\int_{\pi/2} L_t(\theta',\phi') \cos\theta' \sin\theta' \, d\theta' \, d\phi'/E \qquad (5.14)$$

where E is the incident irradiance, generally from a well collimated beam. It is computed from

$$E = \int_{\omega} L_t(\theta,\phi) \cos\theta \, d\omega \,. \qquad (5.15)$$

Note that the integration is over the solid angle $d\omega = \sin\theta \, d\theta \, d\phi$.

Bidirectional reflectance distribution function (BRDF), f, in sr^{-1}: The ratio of the radiance reflected in the direction (θ',ϕ') to the total irradiance on the surface from the direction (θ,ϕ):

$$f(\theta,\phi;\theta',\phi') = L_t(\theta',\phi')/E \,. \qquad (5.16)$$

The quantity $R(\theta,\phi;2\pi)$ is equivalent to ρ. The 2π denotes that the reflectance factor has been integrated over a hemisphere. $R(\theta;d)$, or $R(\theta/d)$, is an equivalent description, the "d" denoting that the diffuse component of reflectance has been included. Even when an integration is not implied, the symbols ϕ and ϕ' are often dropped for simplicity (as is true for any of the above parameters).

Choice of the Reflectance Factor

In calibrating the TM we are interested in knowing the radiance reflected from the gypsum sands into a number of discrete angles. This allows both the directly and diffusely reflected solar radiation to be accurately characterized. A complete BRDF measurement is, however, both time-consuming and difficult to measure. The equipment required is relatively complex, and there are difficulties associated with measuring the incident irradiance. Instead we have chosen to characterize the gypsum by the reflectance factor $R(\theta_z;0°)$. This accurately describes the flux that is directly reflected toward the Landsat sensor. As the gypsum sands are not truly Lambertian, some error is incurred in not computing the full BRDF. Without the BRDF data, a Lambertian surface is assumed. Thus an overestimate is made in the radiance not directly reflected toward the TM. Owing to atmospheric scattering in the atmosphere, some of this flux eventually reaches the sensors. This is the diffuse component of the radiance. The error made in predicting this term increases with increased multiple scattering and with departure from Lambertian behavior. Even so, the use of the reflectance factor is justified because the radiance received at the TM is dominated by the direct component, and multiple scattering is small for clear atmospheric conditions.

Calibrating the Field Reference

The reflectance factor is measured with respect to a reference panel that is calibrated in the laboratory to account for its nonideal characteristics. The calibration procedure is briefly described in the following paragraphs. Here a development of the equations used in the two-step calibration procedure is given.

To begin, it is assumed that a laboratory standard is available. We used a 50-mm-diameter Halon (G-80) disc procured from Eastman Kodak and subsequently calibrated by the National Bureau of Standards (NBS) for $R_{NBS}(45°;0°)$. The fictional parameter $V_p(45°;0°)$ is thereby computed:

$$V_p(45°;0°) = \frac{V_{NBS}(45°;0°)}{R_{NBS}(45°;0°)} . \qquad (5.17)$$

This is the voltage that would have been measured had a unit reflectance Lambertian surface been present.

Using the above, the reflectance factor of the reference panel is found for the same geometry:

$$\begin{aligned} R_{ref}(45°;0°) &= \frac{V_{ref}(45°;0°)}{V_p(45°;0°)} \\ &= \frac{V_{ref}(45°;0°)\, R_{NBS}(45°;0°)}{V_{NBS}(45°;0°)} . \qquad (5.18) \end{aligned}$$

In the next phase of calibration, the reflectance factor measurements are made at the angle of interest, θ. For the ideal Lambertian surface the detector response at angle θ is easily predicted from the response at 45°. Such a surface reflects radiance uniformly into the upper hemisphere, thereby reflecting a factor of $1/\pi$ of the incident irradiance. Thus, for this perfect ($\rho = 1$) Lambertian surface, illuminated with a beam of irradiance $E(\theta)$, the following relationships hold:

$$V_p(45°;0°) = C\,E(45°)\,\rho/\pi = C\,E_\theta\,\cos 45°/\pi \qquad (5.19)$$

$$\begin{aligned} V_p(\theta;0°) &= C\,E(\theta)\,\rho/\pi = C\,E_\theta\,\cos\theta/\pi \\ &= \frac{V_p(45°;0°)\cos\theta}{\cos 45°}\;. \end{aligned} \qquad (5.20)$$

The detector is assumed to have a given response C to the incoming radiance. This latter result is now substituted into the equation for $R_{ref}(\theta;0°)$, to yield the final, desired result:

$$\begin{aligned} R_{ref}(\theta;0°) &= \frac{V_{ref}(\theta;0°)}{V_p(\theta;0°)} \\ &= \frac{V_{ref}(\theta;0°)\cos 45°}{V_p(45°;0°)\cos\theta} \\ &= \frac{V_{ref}(\theta;0°)\cos 45°\,R_{ref}(45°;0°)}{V_{ref}(45°;0°)\cos\theta}\;. \end{aligned} \qquad (5.21)$$

Calibration of January 3, 1983

This section describes the first calibration of a Landsat sensor, using the ground-based measurement techniques discussed above. Measurements were made just months after our contract was initiated. The calibration is of the Landsat-4 TM. Unfortunately, no further calibrations of this sensor were made. No imagery was recorded over our White Sands test site after January 3, as the spacecraft developed severe problems in the solar panels and data telemetry. The following paragraphs are from Castle et al. (1984), which reports the details of this calibration. Data were taken at Cherry site, located just south of Northrup strip.

Determination of Spectral Radiance at the TM from Site Measurements

On January 3, 1983, an 80-mm layer of two-day-old snow covered the flat gypsum surface at the White Sands Missile Range. The reflectance of the snow was measured by reference to a 1.2 x 1.2-m barium sulfate panel using a Barnes modular multispectral 8-channel radiometer (Model 12-1000), which collected radiant flux simultaneously in all the TM spectral bands over a total field angle of 15°. The instrument was mounted on a rotatable boom 2.5 m above the snow to allow an average radiance value to be determined for an area of about 0.5 x 0.5 m. The measurements were made at 1708 GMT, coinciding with the overpass of the TM. The solar zenith angle was 62.8°. With the radiance of the barium sulfate panel at 62.8° as a reference, the reflectance of the snow in TM bands 1 to 4 was found to be 0.769, 0.761, 0.756, and 0.732, respectively, with an rms uncertainty of ±0.02 in all cases.

After the TM overpass, hand-held Exotech radiometer measurements were made at the pixel centers of a 4 x 4 pixel area on the snow (pixel size 30 X 30 m) to check for significant differences from the Barnes radiometer data. Variations between the Barnes and the

Exotech data were small and were attributed to variations introduced by the Exotech measurement technique rather than to variations in the snow reflectance. The 4 x 4 pixel area was later found to be at an angle to the scan lines; as a result, the individual detectors obtained different numbers of samples (see Table 5.6, page 131). By reference to an access road and nearby frozen water surfaces we were able to accurately locate the known reflectance area on the TM imagery.

A solar radiometer (Shaw et al., 1973) with nine 10-nm-wide spectral bands in the visible and near IR was used to determine the total spectral optical depths τ_{ext} at these nine wavelengths. The measured barometric pressure of 889.5 mbar allowed the Rayleigh spectral optical depth τ_{Ray} to be determined. From these data the Mie and ozone spectral optical depths (King and Byrne, 1976) were derived.

In TM bands 1, 2, and 3, the τ_{abs} (molecular absorption) component of τ_{ext} is due entirely to ozone. In band 4, water vapor and CO_2 predominate. Their effects are included in Table 5.1, which lists the values for the various atmospheric components in bands 1 through 4.

Table 5.1 January 3 Optical Depth Components at TM Midband Wavelengths

Band	λ_c(μm)	τ_{ext}	τ_{Mie}	τ_{Ray}	τ_{abs}
1	0.485	0.291	0.148	0.142	0.001
2	0.57	0.218	0.138	0.074	0.006
3	0.66	0.172	0.128	0.041	0.003
4	0.84	0.134	0.110	0.015	0.009

Because of the limitations of the instruments used in this calibration, τ_{abs} in band 4 due to water vapor and CO_2 could not be measured. Instead, the LOWTRAN code (Kneizys et al., 1980) was used to compute the water vapor and CO_2 transmittances across band 4 at 5 cm^{-1} intervals. The water vapor transmittance was scaled, to account for the 44% relative humidity measured at White Sands on January 3, then averaged to find $\tau_{H_2O+CO_2}$. The effect of an error in this estimate can be judged by noting that the inclusion of water vapor and CO_2 lowered the predicted radiance level at the TM by only 2%.

The data in Table 5.1 and the reflectance values quoted above were used as inputs to the Herman radiative transfer code. In using the code, the atmosphere is divided into a sufficient number of plane-parallel layers such that changes in radiance within each layer are due only to single scattering processes. The Gauss-Seidel iterative technique is used to solve the equation of radiative transfer. Upon convergence, all multiple scattering effects have been taken into account. A Junge radial size distribution was assumed for the aerosols. A ν value of 2.5 was assumed in the equation for radial distribution

$$\frac{dN}{dr} = Cr^{-(\nu+1)} \qquad (5.22)$$

where r is the aerosol radius. Values of 5.02, 0.02, and 0.04 μm were used for the maximum and minimum radii and incremental step size, respectively, for the aerosols. The aerosols were given a refractive index of 1.54-0.01i and assumed to have a vertical distribution as measured by Elterman (1966).

The following quantities were calculated by the code. Their values are listed in Table 5.2.

$E_{D,Dir}$	The downward direct solar irradiance at the ground is $E_0 \cos\theta_z * \exp(-\tau_{ext} \sec\theta_z)$, where E_0 is the exoatmospheric solar irradiance and θ_z is the solar zenith angle.
$E_{D,Dif}$	The downward diffuse solar irradiance at the ground.
$L_{U,Dir}$	The upward direct radiance at the TM is $(E_{D,Dir}+E_{D,Dif}) * \exp(-\tau_{ext} \sec 5°)\ \rho/\pi$.
$L_{U,P}$	The upward path radiance at the TM is $L_T - L_{U,Dir}$.
L_T	The total radiance at the TM at a 5° nadir angle.

Table 5.2 Radiative Transfer Code Output

Band	Solar zenith angle	$\frac{E_{D,Dir}}{E_0}$	$\frac{E_{D,Dif}}{E_0}$	$\frac{L_{U,Dir}}{E_0}$	$\frac{L_{U,P}}{E_0}$	$\frac{L_T}{E_0}$
1	55°	0.345	0.185	0.097	0.033	0.130
	65°	0.212	0.152	0.067	0.025	0.092
2	55°	0.392	0.145	0.105	0.024	0.129
	65°	0.253	0.122	0.073	0.019	0.092
3	55°	0.425	0.122	0.111	0.019	0.130
	65°	0.282	0.104	0.078	0.015	0.093
4	55°	0.454	0.095	0.112	0.014	0.126
	65°	0.308	0.082	0.079	0.011	0.090

Data are normalized to unity exoatmospheric solar irradiance.

Values for the exoatmospheric irradiances within the TM passbands, E_0, were found by evaluating

$$E_0 = \frac{1}{d^2} \int_{\lambda_2}^{\lambda_1} E_{0\lambda}\, d\lambda \tag{5.23}$$

where d = 0.983 astronomical units for January 3, λ_1 and λ_2 are the wavelength limits of the TM passbands as determined by using the equivalent passband technique of Palmer and Tomasko (1980), and $E_{\theta\lambda}$ is the exoatmospheric solar spectral irradiance data of Neckel and Labs (1981). The integration was carried out using 2- to 10-nm intervals as dictated by the resolution of the Neckel and Labs data. The required values of L_T/E_θ for the center wavelength of each band and the solar zenith angle of 62.8° were found by interpolating between the 55° and 65° radiative transfer code data in Table 5.2. These, when multiplied by their corresponding E_θ values, gave the radiances in mW cm^{-2} sr^{-1} in the TM passbands listed in Table 5.3. (An error of less than 1% is introduced using the value at the center wavelength of each band instead of evaluating

$$E_\theta = \frac{1}{d^2}\int_{\lambda_2}^{\lambda_1} E_{\theta\lambda}\, \ell(\lambda)\, d\lambda \tag{5.24}$$

where $\ell(\lambda)$ is the output as a function of wavelength from the radiative transfer code, as given by L_T/E_θ in Table 5.2.)

Table 5.3 Exoatmospheric Irradiance and the Band-Integrated Radiance at the TM As Determined from Site Measurements

Band	Equivalent TM bandwidths (μm)	Wavelength limits (μm)	E_θ (mW cm^{-2})	L_T (mW cm^{-2} sr^{-1})
1	0.0715	0.4503-0.5218	14.4	1.45
2	0.0887	0.5269-0.6156	16.6	1.66
3	0.0771	0.6213-0.6984	12.3	1.25
4	0.1349	0.7719-0.9068	14.7	1.44

Radiance at the TM from Image Digital Counts and System Calibration Data

The next step in the calibration procedure is to determine L_T from preflight and in-flight internal calibration data. By identifying our site on the Landsat image, we determined which detectors scanned the area and in what order, and how many samples each collected. The site was scanned from north to south by detectors 3, 2, 1, 16, and 15, in that order. They collected 1, 3, 5, 4, and 2 samples, respectively. We found the average digital count for each detector, using offset and gain values reported by Barker et al. (1985b), then calculated the average spectral radiance L_T = (average count - offset)/gain. (Throughout this report, spectral radiances are referred to the TM entrance pupil.) These spectral radiances were multiplied by the number of samples for each detector. The resultant products were added and then divided by the total number of samples, 15. Thus we derived a value for the average spectral radiance of our site as measured by the TM, proportionally weighted according to the number of samples per detector. These values are listed in Table 5.4. Then the average spectral radiance per band was multiplied by the equivalent bandwidth to provide the weighted average radiance in each band, as shown in column B of Table 5.5.

Barker et al. (1985a) have reported that the TM internal calibrator, used in flight, indicates that the response of TM bands 1 through 4 has slowly decreased with time during the period July-December 1982. We have used these data to modify the prelaunch calibration data. These modified values are listed in column C of

Table 5.4 Average Counts and Spectral Radiances (mW cm^{-2} sr^{-1} μm^{-1}) for Five Detectors As Calculated from Preflight Calibration Data

	Band 2		Band 3		Band 4	
Detector	Average count	Average spectral radiance	Average count	Average spectral radiance	Average count	Average spectral radiance
3	139.0	17.04	165.0	15.40	133.0	11.89
2	143.7	17.42	169.7	15.86	132.0	12.02
1	146.2	17.52	171.6	15.73	134.2	12.00
16	141.5	17.43	167.8	15.85	132.0	12.01
15	147.5	17.65	172.5	15.88	131.5	12.05
Weighted average		17.46		15.78		12.01

Table 5.5 Comparison of TM Band Radiances (mW cm^{-2} sr^{-1}) for Data of January 3, 1983

Band	Column A	Column B	Column C	(A-B)/A, %	(A-C)/A, %
2	1.66	1.55	1.50	6.6	9.8
3	1.25	1.22	1.16	2.4	7.2
4	1.44	1.62	1.57	-12.9	-9.6

Column A gives the radiance levels at the TM as derived from ground and atmospheric measurements at White Sands on January 3, 1983, and the use of an atmospheric radiative transfer program (see Table 5.3).

Column B gives the weighted average radiance in each passband (mW cm^{-2} sr^{-1}) as determined from TM image data of our White Sands site in conjunction with pre-flight calibration data.

Column C gives the values in column B as modified by the change in response suggested by the internal calibrator data of December 8, 1982.

Table 5.5. With respect to this decrease in response, we note that the internal calibrator compares the responses of only the TM filters, detectors, and electronics to seven different irradiance levels; it does not measure any change in transmittance of the image-forming system. It is also possible that the decrease in response is wholly or partly due to a change in the output of the internal calibrator.

Because of the small number of samples collected over the test site and the small variation in the digital counts recorded by each detector in each band, the most meaningful way to summarize the results of the calibration is to list the individual counts for each detector and the radiance in each band, as shown in Table 5.6. Note

Table 5.6 Digital Counts for Each Detector That Sampled the Ground Site, and the Radiance at the TM Determined from the Measurements at White Sands

	Detector No.					Radiance at TM
	3	2	1	16	15	(mW cm^{-2} sr^{-1})
Band 2	139	143	147	141	147	1.66
		144	146	141	148	
		143	145	141		
			147	143		
			146			
Band 3	165	170	172	167	172	1.25
		169	172	167	172	
		170	171	168		
			171	169		
			172			
Band 4	133	132	134	133	130	1.44
		131	134	131	133	
		133	134	131		
			134	133		
			135			

that whereas there are significant detector-to-detector variations within a band, the variations for a given detector are consistent with the expected uncertainty in the output of the analog-to-digital converter for a constant input analog signal.

Extension of Calibration to Other Detectors

To extend the calibration of the five detectors in each band to all 16 detectors in each band, a 10 x 16 pixel test site of uniform reflectance was selected from an analysis of the TM imagery of White Sands. This site was 500 m southwest of the 4 x 4 pixel test site described earlier. Its uniformity was such that none of the 16 rows of 10 pixels exhibited a variance of greater than 1.5 digital counts, the average variance being 0.9 digital count. The average number of digital counts for each of the 16 detectors in each band in this 10 x 16 pixel area is listed in Table 5.7. To verify, a posteriori, that the large site had the same reflectance as the 4 x 4 pixel site, the digital counts were compared for detectors 3, 2, 1, 16, and 15 in the three bands. For the 15 detectors that sampled both sites (five each in three bands) the digital count difference between the two sites was less than 1 for nine of the detectors.

It is interesting that there was no evidence of a level shift, as described by Kieffer, Eliason, and Chavez (1985), in this part of the scene. The 10 x 16 pixel area was selected on the basis of its close statistical match to the 4 x 4 pixel area and was later found to have been scanned by detectors 1 through 8 in one direction and by detectors 9 through 16 in the reverse direction. However, in other

Table 5.7 Average Digital Counts for the 10 x 16 Pixel Test Site in the Three TM Bands

Detector	Band 2	Band 3	Band 4
1	145.4	171.5	133.8
2	142.7	167.8	131.0
3	141.0	167.4	133.0
4	143.0	166.8	131.4
5	145.2	168.4	131.2
6	144.0	168.7	132.4
7	142.8	167.3	131.7
8	142.5	167.5	132.0
9	143.4	168.8	132.6
10	142.1	167.5	137.2
11	141.4	166.3	130.9
12	141.7	169.8	132.7
13	145.2	168.6	134.2
14	143.8	168.9	132.3
15	146.2	170.2	130.7
16	141.0	167.1	132.1

parts of the scene, certain detectors did exhibit a level shift of up to 3 counts.

The average digital count values in Table 5.7 can be compared to our computed TM entrance pupil radiance values given in Column A of Table 5.5 to provide a single point calibration for all detectors in TM bands 2, 3, and 4.

Summary

The absolute calibration of five detectors in TM bands 2, 3, and 4, as determined by measurements at White Sands on January 3, 1983, is given in Table 5.5. Preflight calibration results agree with these in-flight measurements to 6.6%, 2.4%, and 12.9% in bands 2, 3, and 4, respectively. Table 5.7 shows the absolute calibration extended to all the detectors in bands 2, 3, and 4. The estimated uncertainty in these results is ±5%; the estimated uncertainty in the preflight calibration is no better than ±6% (Barker et al., 1985b; Norwood and Lansing, 1983).

Band 1 saturated over the snowfield at White Sands. Preflight data (Barker et al., 1985b) indicate that a saturation level of 255 counts corresponds to a radiance at the sensor of 1.14 mW cm^{-2} sr^{-1} in TM band 1. We estimate that the snowfield provided a radiance level of 1.45 mW cm^{-2} sr^{-1} at the sensor.

Calibration of July 8, 1984

The data reduction for the July 8, 1984, calibration has been reported in our seventh quarterly report on Contract NAS5-27382, to NASA. This section has been extracted from that report with minor revisions. These include an analysis of the diffuse-to-direct data and a comparison of the predicted radiance with that determined from the preflight gain and offset values. A new test site (Chuck site) was selected for this calibration. It is 5 km east of the previous site and at a right angle bend in the road. The bend facilitates locating the site on the TM imagery.

Field Measurements

This was our first opportunity to acquire on-site measurements at White Sands in conjunction with Thematic Mapper imagery from Landsat 5. Imagery was not available for previous trips owing to cloud cover. The instrumentation on hand included two Barnes modular multispectral radiometers, a cart and yoke (to carry the MMRs), the older of Reagan's two radiometers, both of the Castle spectropolarimeters, four Polycorders, a printer, the Compaq computer, and two 0.6 x 0.6 m standard reflectance panels.

Sunrise on the morning of July 8 was at 6:10 a.m. New Mexico is on Mountain Daylight Time (MDT) this time of year, as are the times quoted here. The Reagan instrument was set up and began acquiring solar irradiance measurements at 7:15 a.m. (air mass 4). Temperature, humidity, and pressure readings were taken on site.

Two 4 x 4 pixel test grids had been laid out on the previous visit. Each was aligned with the east/west scan lines expected of Landsat. (Later, the grids were found to be misaligned, and were rotated in October 1984.) A road with a 90° bend separated the two grids, facilitating their identification on the digital TM imagery. Each site was measured with an MMR. Starting at the center of each 30-m pixel, five reflectance measurements were taken of the gypsum sands, within an area of about 5.0 x 0.5 m. Reflectance panel readings were taken periodically during the course of these measurements. (Both the $BaSO_4$ and Halon panels were recalibrated immediately upon our return to Tucson.) The data were averaged and recorded on Polycorders. The grid north of the road was scanned from 11:00 to 11:20 a.m., using Barnes MMR S#116, mounted on a cart with a $BaSO_4$ panel. Simultaneously, the south grid was scanned with Barnes MMR S#119 attached to a yoke for hand operation. A painted Halon panel was used as the reference here. In addition to the two 4 x 4 pixel areas, two small areas were scanned, between 10:20 and 11:44 a.m. These areas were selected for their contrast, representing extremes of light and dark for the local area, and were used to assign reflectance values to the digitized aerial photo. Diffuse-to-direct measurements were taken between 8:30 and 10:20 a.m., by comparing the radiance reflected from a reflectance panel to that measured in a similar configuration but with the sun blocked by a styrofoam parasol. These data can be compared with the radiative transfer code to verify our atmospheric models.

A helicopter overflight was arranged for this trip. The flight lasted almost 1 hour. It had the dual purpose of recording radiance at intermediate altitudes, again for comparison to the radiative transfer codes, and photographing the site. Five rolls of Ektachrome, ASA 100, were shot. All photos were taken at 1/500 of a second, with a 200 mm focal length lens. A series was taken at 1829, at 610, and at 152 m (6000, 2000, and 500 ft) AGL (above ground level). The photos were bracketed from F/16 to F/22. Those taken at 610 m were particularly suited to our needs. Eight colored ground cloths had been laid out to define the two 4 x 4 pixel areas that were measured with the MMR. The blue and orange ground blankets were the most visible from the air, as well as the easiest to see on the color slides.

Langley Plot Computations

The Reagan radiometer was cycled through its narrowband filter set 95 times during the course of the morning. Each data set included a start and finish time (to the nearest second) and a voltage reading for each of the nine spectral filters. These data were used as input to a program that computed solar zenith angle from ephemeris data, as described earlier in this chapter. Using a refraction correction, we calculated air masses for each measurement. These τ_{ext} results are given in Table 5.8.

Using measured atmospheric pressure (883 mbar), we computed τ_{Ray}. After subtracting this from τ_{ext}, we plotted a curve that contained only Mie and molecular absorption components, as shown in Figure 5.2(a). To determine τ_{Mie}, a curve is fit through all the $\tau_{ext} - \tau_{Ray}$ data points that do not include absorption. Normally this is done by submitting the optical depth values to a routine that fits them to an equation of the form $\log \tau_{Mie} = a_0 + a_1 \log \lambda + a_2 (\log \lambda)^2$, as described earlier. For this case, two of the spectral filter data sets were rejected because no power was available at the site to operate the radiometer heater. The data for the 0.872 and 1.03 μm channels are less reliable without the temperature stabilization, owing to fluctuations in detector responsivity.

Instead of our normal procedures, a manual fitting of the data was performed. A curve of the form $\log \tau_{Mie} = a_0 + a_1 \log \lambda$ was assumed (a straight line on this log/log plot). This is an approximation, valid only if the aerosols can be correctly modeled as obeying a Junge radial size distribution, $dn/dr = c\, r^{-(\nu+1)}$. In such a case the data would fall exactly on a line whose slope, a_1, yields the Junge parameter ν by means of the relationship $a_1 = -\nu + 2$. By using only the 0.440 and 0.780 μm data points, a slope was determined. At these wavelengths the ozone absorption coefficients are small. Actually,

Table 5.8 Langley Plot Results for July 8, 1984

Wavelength (μm)	τ_{ext}	τ_{Mie}	τ_{Ray}	τ_{oz}
0.4000	0.4426	0.0981	0.3172	0.0000
0.4400	0.3060	0.0922	0.2138	0.0006
0.5217	0.1921	0.0824	0.1063	0.0127
0.6120	0.1543	0.0743	0.0555	0.0246
0.6708	0.1091	0.0699	0.0382	0.0098
0.7120	0.1063	0.0673	0.0300	0.0046
0.7797	0.0842	0.0634	0.0208	0.0027
0.8717	0.0948	0.0589	0.0133	0.0006
1.0303	0.1103	0.0528	0.0068	0.0000

Data from "Old" Reagan Radiometer (SN002)
8 July, 1984
Chuck Site, White Sands, New Mexico

Latitude	32.935 °
Longtitude	106.407 °
Right ascension	7.226 hours
Declination	22.365 °
Difference (dec)	-419.3 arc-sec
Earth-sun distance	1.016701 AU
Pressure	883 mbar

$\log \tau_{Mie} = a_0 + a_1 \log \lambda$

$a_0 = -1.269, \quad a_1 = -0.654$

$\tau_{Ray} = 29123.7 \, (n^2-1)^2/\lambda^4$

$$(n-1)*10^8 = 6432.8 + \frac{2949810}{146 - \lambda^2} + \frac{25540}{41 - \lambda^2}$$

$\tau_{oz,\lambda} = NOZ*\alpha_\lambda$

NOZ = columnar ozone
= $\tau_{oz,0.612\mu m}/\alpha_{0.612\mu m}$ = 213.2 matm-cm

α = spectral absorption coefficient

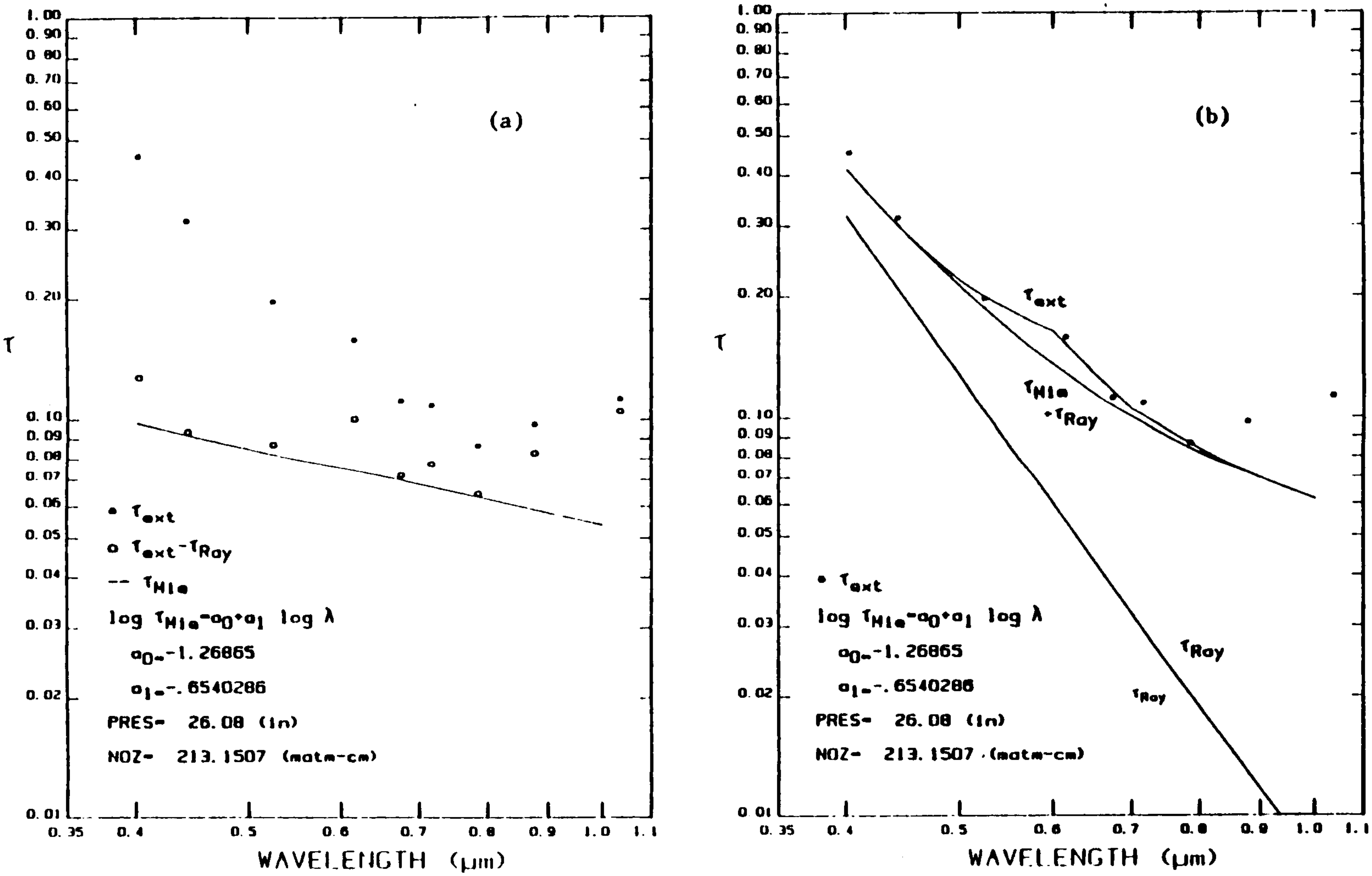

Figure 5.2 Optical depth versus wavelength data from the Reagan radiometer.

(a) τ_{Mie} (solid line), determined from a fit to $\tau_{ext} - \tau_{Ray}$ data. (b) The deduced τ_{Ray}, $\tau_{Ray} + \tau_{Mie}$, and $\tau_{Ray} + \tau_{Mie} + \tau_{oz}$ curves, plotted as a function of wavelength.

the 0.440 µm and 0.872 µm pair is preferred, as the absorption coefficients are approximately equal. The data at 0.872 µm for this date, however, are unreliable, owing to the temperature problem mentioned above. With the given constraints, the slope was found to be $a_1 =$ -0.654; thus $\nu = 2.65$ and $a_0 = -1.269$. With these constants the τ_{Mie}, τ_{Ray}, and τ_{oz} components can be computed for any wavelength. Figure 5.2(b) shows how each of these components contributes to the total optical depth. Table 5.9 gives the respective components for the TM midband wavelengths. These data were used as input to the radiative transfer code. To be complete, a component of τ_{H_2O} was included for band 4. This was determined from the temperature (31.3°C) and relative humidity (36%) for late morning of July 8. Using Fig. 4.6 we find that the columnar amount of water vapor for this date was approximately 1 g cm^{-2} km^{-1}. This corresponds to an optical depth, from Table 4.5, of $\tau_{H_2O} = 0.0568$ (averaged over band 4). Table 5.9 also reports the exoatmospheric solar irradiance, corrected for the earth-sun distance d = 1.0167378 AU. These were computed by weighting

Table 5.9 Spectral Components for TM Midband Wavelengths

Wavelength (µm)	τ_{ext}	τ_{Mie}	τ_{Ray}	τ_{oz}	τ_{H_2O}	E_0 (mW cm^{-2} μm^{-1})
0.486	0.2340	0.0864	0.1421	0.0055	0.	189.162
0.571	0.1744	0.0777	0.0735	0.0232	0.	176.723
0.661	0.1226	0.0706	0.0406	0.0114	0.	149.453
0.838	0.1342	0.0605	0.0156	0.0013	0.0568	104.284

E_0 is computed by multiplying band-averaged irradiance (Table 5.10) data with $1/d^2$, where d = 1.0167378 for this date.

the solar irradiance data of Iqbal (1983) with the TM-5 response function (Barker and Markham, 1985), namely

$$\bar{E}_{o\lambda} = \frac{\int_0^\infty R_\lambda E_{o\lambda}\, d\lambda}{\int_0^\infty R_\lambda\, d\lambda} . \tag{5.25}$$

These data are given in Table 5.10, for each of the TM-5 reflective bands. This approach was adopted since the integrating sphere output was so weighted with R_λ during the prelaunch calibration (Barker, 1985), and later a comparison is made to the prelaunch calibration. It is interesting that $\bar{E}_{o\lambda}$, when averaged (with no weighting) over the cut-off limits reported by Palmer (1984), differs from those computed by Eq. (5.25) by no more than 0.5%. These solar irradiance data are multiplied by a factor of $1/d^2$ to obtain the data in Table 5.9. The midband wavelengths of the TM sensor were computed by Palmer (1984) using the moments method and the preflight filter transmittance data.

Table 5.10 Weighted Exoatmospheric Data for Mean Earth-Sun Distance

Band	$\bar{E}_{o\lambda}$ (mW cm^{-2} sr^{-1} μm^{-1})
1	195.5475
2	182.6889
3	154.4979
4	104.2836
5	22.0186
7	7.4777

Panel Calibration

The Herman radiative transfer code requires that the absolute reflectance of the gypsum sands be known. We have instead chosen to use the reflectance factor $R(\theta_z/0°)$. Here θ_z is the angle incident upon the gypsum, and 0° is the reflected angle, equal to the Thematic Mapper nadir-look angle. By use of this quantity, the amount of light reflected in the direction of the TM is accurately characterized. A full BRDF characterization would be preferred. The gain in accuracy is not warranted, however, as the BRDF data would be difficult and time-consuming to obtain.

In the field this reflectance is measured with one of two Barnes MMRs. Since these are uncalibrated, they must be used in conjunction with a reference panel. The reflectance factor of the gypsum sands is determined by the relationship

$$R_{sand} = \frac{V_{sand} R_{ref}}{V_{ref}} . \tag{5.26}$$

Here V_{sand} and V_{ref} are the output voltages of the MMR when looking over the sands and reflectance panel, respectively. These voltages are proportional to the radiance scattered upward and within the instrument's 15° field of view (FOV). R_{ref} is the reflectance of the panel, as determined in the laboratory. On July 8 one of the radiometers was assigned the Halon panel and the other was assigned the $BaSO_4$ panel. While looking at the sands, each instrument was periodically swung over the reference panel, and voltage readings were recorded. Upon our return to Tucson, we calibrated both panels.

The calibration of the panels was conducted at the Optical Sciences Center, in a manner illustrated in Fig. 5.3. A tungsten lamp was put at the focal point of an off-axis parabolic mirror. The emerging collimated beam illuminated the reference panel at a known angle. The radiance reflected in a direction normal to the surface was measured using a radiometer built by Che Nianzeng (Nianzeng, 1984). Then the reference panel was removed, and a primary standard surface was put in its place. This primary standard was a Halon panel that had been calibrated for reflectance factor $R_{NBS}(45°/0°)$ by NBS on February 8, 1984. In the first phase of the field panel calibration, the reflectance factor $R_{ref}(45°/0°)$ was computed from Eq. (5.18). Next, the desired reflectance factor was computed from Eq. (5.22).

The above steps were repeated for four spectral bandpass filters, each 40 nm wide. The measurement uncertainty was estimated

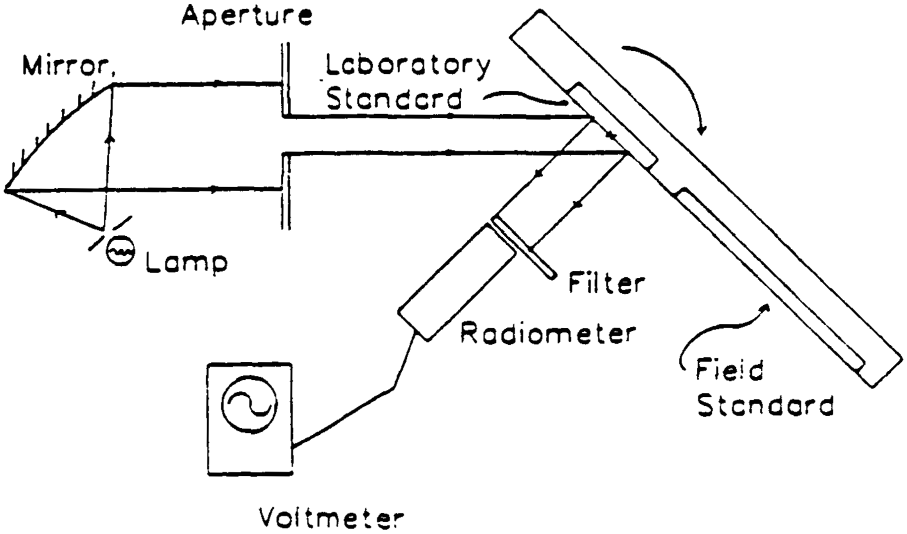

Figure 5.3 Laboratory setup for the calibration of field reflectance panels.

to be less than 1%. A small error in the reflectance factor was also introduced owing to the nonuniformity of the panels. In the field the radiance reflected from the panels was averaged over a larger area. This was due to the 15° FOV, as compared to the 1° FOV of the laboratory radiometer. The results of the panel calibration are shown in Table 5.11. At those angles in which the reflectance factor is greater than unity, more energy is directed than would be from a perfect Lambertian surface.

Reflectance Data

Both the MMR data and the panel calibration data were used to determine the absolute reflectance of each of the test sites at White Sands. The field measurements were taken at several times throughout the morning. The data taken closest to the time of the Landsat overpass, 11:07:40 MDT, were used in the radiance computations.

Several interpolations had to be made on the laboratory calibration data. The solar zenith angles were first computed for those times at which a field measurement of the gypsum sands was taken. The panel reflectance factors of Table 5.11 were next interpolated to find the corresponding reflectance values at these angles, for the four spectral filters available on Che's radiometer. These wavelengths differ from those of the MMR; therefore one final interpolation was necessary in order to compute the reflectances for the seven MMR wavelengths. (The wavelengths of the MMR correspond to those of the TM.)

Table 5.11 Laboratory Calibration of the Reflectance Factors of $BaSO_4$ Panel 5 and Halon Panel

Irradiance angle (°)	Filter bandwidth (nm)			
	430–470	530–570	630–670	830–870
		$BaSO_4$ Panel 5		
10	1.0420	1.0355	1.0205	0.9858
15	1.0196	1.0138	0.9990	0.9651
20	1.0011	0.9945	0.9807	0.9479
25	0.9836	0.9779	0.9642	0.9331
30	0.9668	0.9610	0.9479	0.9185
35	0.9499	0.9449	0.9327	0.9045
40	0.9326	0.9279	0.9169	0.8905
45	0.9155	0.9119	0.9007	0.8773
50	0.8971	0.8937	0.8851	0.8627
55	0.8783	0.8765	0.8676	0.8474
60	0.8597	0.8582	0.8498	0.8326
65	0.8380	0.8390	0.8310	0.8157
70	0.8157	0.8174	0.8127	0.7986
75	0.7926	0.7929	0.7892	0.7789
		Halon Panel		
10	0.9965	1.0007	1.0020	1.0042
15	0.9892	0.9949	0.9951	0.9973
20	0.9829	0.9872	0.9888	0.9901
25	0.9741	0.9794	0.9804	0.9816
30	0.9648	0.9702	0.9716	0.9728
35	0.9556	0.9597	0.9618	0.9636
40	0.9442	0.9489	0.9499	0.9515
45	0.9319	0.9368	0.9377	0.9391
50	0.9166	0.9210	0.9231	0.9253
55	0.8991	0.9042	0.9061	0.9073
60	0.8784	0.8832	0.8860	0.8877
65	0.8539	0.8608	0.8633	0.8638
70	0.8221	0.8297	0.8323	0.8343
75	0.7805	0.7872	0.7919	0.7944

Date: July 12, 1984
Samples: $BaSO_4$ panel 5 and Halon panel
Reference: Halon calibrated at (45°/0°) geometry by NBS (February 8, 1984)
Location: Infrared Laboratory, Optical Sciences Center
Viewing zenith angle: 0°
Irradiance angle: 10°-75°

The reflectance factors of the gypsum were determined from the above computed panel reflectances by means of Eq. (5.26). This data reduction is summarized in Table 5.12. Only the data in channels 1 through 4 are used here. Reflectance factors are given for pixels 1 through 16; these pixels are identified on Fig. 5.4.

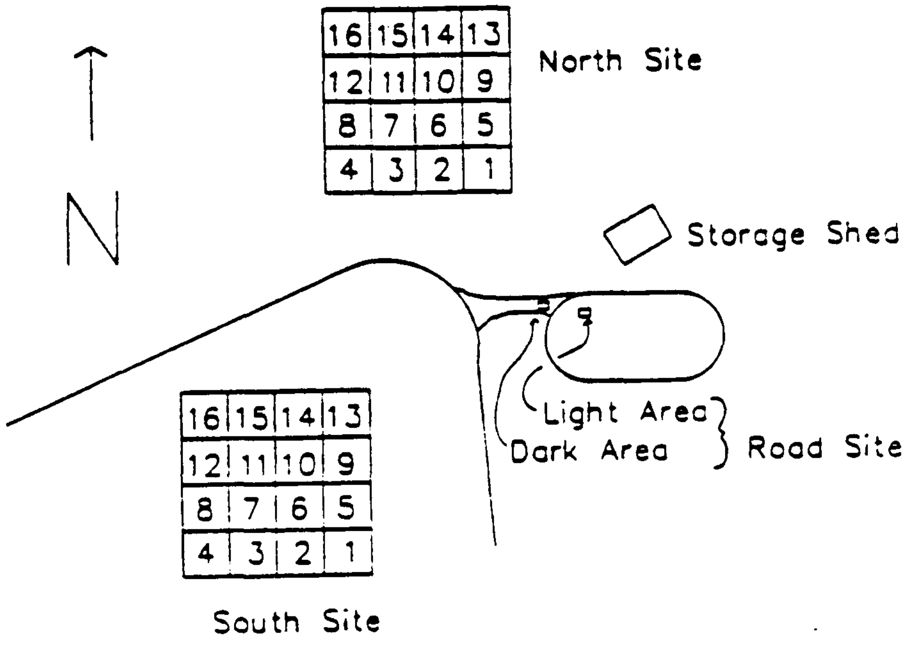

Figure 5.4 Schematic of Chuck site test area.

Radiative Transfer Computations

The mean reflectance values, given in bold type in Table 5.12, were used as input to the radiative transfer code. Also input were the atmospheric components listed in Table 5.9. The model assumptions, described earlier, were made for the aerosols. The code was run for solar zenith angles of 25° and 35°. The output, given in

Table 5.12 Absolute Reflectance of White Sands Test Sites

Time	CH(1)	CH(2)	CH(3)	CH(4)	CH(5)	CH(6)	CH(7)
			North Site				
BaSO$_4$							
10:52	0.957	0.952	0.939	0.915	0.858	0.839	0.715
11:02	0.964	0.959	0.946	0.921	0.863	0.844	0.718
Road							
10:54	0.510	0.577	0.619	0.650	0.625	0.527	0.259
Pixels 1-4,8							
10:57	0.503	0.573	0.616	0.648	0.620	0.517	0.246
10:57	0.510	0.581	0.627	0.660	0.632	0.527	0.236
10:58	0.515	0.584	0.629	0.661	0.631	0.525	0.244
10:59	0.530	0.601	0.645	0.680	0.646	0.535	0.231
11:01	0.504	0.571	0.617	0.652	0.629	0.526	0.231
BaSO$_4$							
11:02	0.964	0.959	0.946	0.921	0.863	0.844	0.718
11:08	0.968	0.963	0.950	0.924	0.866	0.846	0.719
Pixels 5-7							
11:04	0.475	0.538	0.579	0.610	0.589	0.492	0.233
11:05	0.488	0.552	0.594	0.626	0.601	0.497	0.230
11:06	0.504	0.571	0.613	0.643	0.611	0.502	0.224
BaSO$_4$							
11:08	0.968	0.963	0.950	0.924	0.866	0.846	0.719
11:15	0.973	0.968	0.954	0.929	0.869	0.849	0.719
Pixels 9-12							
11:08	0.488	0.555	0.599	0.630	0.605	0.501	0.230
11:10	0.504	0.574	0.620	0.653	0.623	0.511	0.229
11:11	0.512	0.580	0.624	0.657	0.627	0.519	0.228
11:12	0.526	0.597	0.643	0.676	0.637	0.520	0.213
BaSO$_4$							
11:15	0.973	0.968	0.954	0.929	0.869	0.849	0.719
11:20	0.976	0.971	0.958	0.932	0.871	0.851	0.720
Pixels 13-16							
11:17	0.501	0.566	0.608	0.637	0.611	0.512	0.252
11:18	0.533	0.602	0.644	0.674	0.640	0.533	0.225
11:19	0.511	0.581	0.624	0.656	0.631	0.526	0.228
11:20	0.513	0.583	0.626	0.656	0.621	0.508	0.215
Cumulative:							
Mean	**0.507**	**0.576**	**0.619**	**0.651**	0.622	0.516	0.231
SDEV	0.015	0.017	0.018	0.019	0.015	0.013	0.010

Table 5.12—Continued

Time	CH(1)	CH(2)	CH(3)	CH(4)	CH(5)	CH(6)	CH(7)
			South Site				
$BaSO_4$							
10:58	0.965	0.968	0.970	0.971	0.973	0.974	0.980
11:09	0.969	0.973	0.974	0.975	0.977	0.978	0.983
1st Scan							
10:59	0.489	0.551	0.599	0.642	0.625	0.500	0.233
10:59	0.494	0.557	0.601	0.638	0.618	0.497	0.241
11:00	0.491	0.548	0.590	0.627	0.604	0.481	0.229
11:00	0.468	0.529	0.573	0.612	0.591	0.468	0.229
11:01	0.487	0.546	0.588	0.626	0.600	0.480	0.246
11:01	0.493	0.550	0.592	0.632	0.606	0.482	0.228
11:02	0.509	0.572	0.615	0.653	0.630	0.508	0.251
11:02	0.514	0.576	0.618	0.658	0.628	0.500	0.231
11:03	0.486	0.546	0.590	0.629	0.614	0.491	0.236
11:04	0.503	0.567	0.611	0.650	0.634	0.519	0.256
11:04	0.516	0.578	0.622	0.660	0.637	0.512	0.243
11:05	0.498	0.559	0.603	0.641	0.621	0.500	0.241
11:05	0.510	0.572	0.616	0.654	0.624	0.492	0.228
11:06	0.510	0.569	0.610	0.647	0.616	0.489	0.230
11:06	0.506	0.567	0.610	0.650	0.632	0.514	0.250
11:07	0.503	0.561	0.603	0.643	0.622	0.500	0.250
Mean	**0.499**	**0.559**	**0.603**	**0.641**	0.619	0.496	0.239
SDEV	0.013	0.014	0.013	0.013	0.013	0.014	0.010
$BaSO_4$							
11:16	0.972	0.975	0.976	0.977	0.980	0.980	0.986
11:27	0.976	0.979	0.980	0.981	0.984	0.984	0.989
2nd Scan							
11:16	0.492	0.552	0.594	0.634	0.619	0.499	0.247
11:17	0.495	0.561	0.607	0.646	0.625	0.500	0.240
11:17	0.494	0.557	0.601	0.638	0.616	0.488	0.236
11:18	0.493	0.555	0.601	0.640	0.621	0.494	0.239
11:18	0.499	0.558	0.600	0.638	0.612	0.487	0.248
11:19	0.512	0.573	0.618	0.659	0.633	0.503	0.235
11:19	0.508	0.571	0.614	0.653	0.629	0.502	0.238
11:20	0.520	0.582	0.626	0.666	0.638	0.503	0.234
11:21	0.501	0.563	0.610	0.651	0.633	0.505	0.242
11:21	0.521	0.587	0.633	0.673	0.654	0.527	0.250
11:22	0.519	0.582	0.626	0.665	0.643	0.513	0.239
11:22	0.518	0.579	0.623	0.662	0.642	0.517	0.249
11:23	0.520	0.584	0.630	0.670	0.639	0.500	0.229
11:24	0.513	0.573	0.618	0.659	0.633	0.502	0.244
11:24	0.507	0.573	0.618	0.658	0.640	0.520	0.254
11:25	0.514	0.574	0.616	0.655	0.630	0.501	0.250

Table 5.12—Continued

Time	CH(1)	CH(2)	CH(3)	CH(4)	CH(5)	CH(6)	CH(7)
Mean	0.508	0.570	0.615	0.654	0.632	0.504	0.242
SDEV	0.011	0.011	0.012	0.012	0.011	0.011	0.007
			Road Site				
$BaSO_4$							
10:27	0.940	0.935	0.924	0.900	0.846	0.828	0.711
10:32	0.943	0.939	0.927	0.903	0.849	0.831	0.711
1st Dark Area Scan							
10:28	0.445	0.495	0.529	0.553	0.540	0.472	0.235
10:28	0.459	0.508	0.541	0.562	0.543	0.473	0.228
10:28	0.463	0.513	0.544	0.565	0.543	0.470	0.223
10:29	0.458	0.509	0.543	0.564	0.543	0.470	0.224
10:29	0.473	0.525	0.559	0.581	0.558	0.481	0.226
Mean	0.459	0.510	0.543	0.565	0.545	0.473	0.227
SDEV	0.010	0.011	0.011	0.010	0.007	0.005	0.005
1st Light Area Scan							
10:29	0.516	0.580	0.623	0.656	0.607	0.480	0.178
10:30	0.501	0.560	0.600	0.632	0.585	0.463	0.169
10:30	0.504	0.564	0.602	0.635	0.589	0.469	0.174
Mean	0.507	0.568	0.608	0.641	0.594	0.471	0.174
SDEV	0.008	0.010	0.013	0.013	0.012	0.009	0.004
$BaSO_4$							
10:37	0.947	0.942	0.930	0.906	0.851	0.832	0.712
10:40	0.949	0.944	0.932	0.908	0.852	0.834	0.712
2nd Dark Area Scan							
10:37	0.447	0.495	0.527	0.549	0.534	0.467	0.233
10:38	0.455	0.505	0.538	0.559	0.543	0.473	0.233
10:38	0.457	0.506	0.538	0.560	0.541	0.469	0.224
10:38	0.457	0.507	0.540	0.562	0.541	0.467	0.224
10:38	0.476	0.525	0.558	0.579	0.556	0.476	0.223
Mean	0.458	0.508	0.540	0.562	0.543	0.470	0.227
SDEV	0.011	0.011	0.011	0.011	0.008	0.004	0.005
2nd Light Area Scan							
10:39	0.516	0.578	0.618	0.651	0.604	0.477	0.177
10:39	0.505	0.566	0.605	0.638	0.590	0.463	0.167
10:40	0.504	0.561	0.597	0.628	0.583	0.464	0.172
Mean	0.509	0.568	0.607	0.639	0.592	0.468	0.172
SDEV	0.007	0.009	0.011	0.011	0.010	0.008	0.005
$BaSO_4$							
11:38	0.989	0.983	0.969	0.942	0.879	0.859	0.722
11:42	0.991	0.986	0.972	0.945	0.881	0.860	0.723

Table 5.12—Continued

Time	CH(1)	CH(2)	CH(3)	CH(4)	CH(5)	CH(6)	CH(7)
3rd Dark Area Scan							
11:39	0.478	0.534	0.568	0.589	0.569	0.495	0.245
11:39	0.479	0.534	0.569	0.591	0.567	0.488	0.233
11:40	0.487	0.543	0.577	0.598	0.573	0.493	0.236
11:40	0.485	0.542	0.577	0.598	0.571	0.490	0.233
11:40	0.499	0.554	0.587	0.608	0.580	0.495	0.232
Mean	0.486	0.541	0.576	0.597	0.572	0.492	0.236
SDEV	0.008	0.008	0.008	0.008	0.005	0.003	0.005
3rd Light Area Scan							
11:41	0.540	0.608	0.651	0.682	0.629	0.498	0.189
11:41	0.530	0.597	0.639	0.669	0.614	0.481	0.176
11:42	0.530	0.598	0.639	0.667	0.613	0.485	0.181
Mean	0.533	0.601	0.643	0.673	0.619	0.488	0.182
SDEV	0.006	0.006	0.007	0.008	0.009	0.009	0.006

Table 5.13, was normalized for an exoatmospheric solar irradiance of 1. After interpolating the data for a solar angle of 29.2158° (that corresponding to the time of the overpass), we multiplied the output by the appropriate irradiance value. These final values are given in Table 5.14. They are the radiances predicted to be incident on the TM sensor on the morning of July 8, as it imaged our White Sands site.

Because of instrument problems and difficulties in accurately mapping ground reflectance due to the helicopter photography not being vertical, the results of the July 8, 1984, measurement have high uncertainties associated with them. In particular, the τ_{ext} data are highly questionable at longer wavelengths, owing to the lack of tem-

Table 5.13 Herman Code Output

	Zenith angle					
	25°			35°		
	Wavelength (µm)			Wavelength (µm)		
	0.571	0.661	0.838	0.571	0.661	0.838
July 8, 1984, calibration						
$\nu = 2.65$, $R = 0.02$ to 5.02, step 0.04, $N = 1.54 - 0.01i$						
τ_{Mie}	0.0777	0.0706	0.0605	0.0777	0.0706	0.0605
τ_{Ray}	0.0735	0.0406	0.0156	0.0735	0.0406	0.0156
τ_{abs}	0.0232	0.0114	0.0581	0.0232	0.0114	0.0581
Refl	0.576	0.619	0.651	0.576	0.619	0.651
E_{dir}	0.7477	0.7916	0.7816	0.6621	0.7053	0.6954
E_{dif}	0.1262	0.1001	0.0621	0.1199	0.0956	0.0593
L_{path}	0.0230	0.0181	0.0113	0.0208	0.0162	0.0102
L_T	0.15760	0.17351	0.16421	0.14117	0.15584	0.14686
Intermediate altitude: 10,000 ft above sea level						
τ_{Mie}	0.0423	0.0385	0.0330	0.0423	0.0385	0.0330
τ_{Ray}	0.0584	0.0323	0.0124	0.0584	0.0323	0.0124
τ_{abs}	0.0230	0.0113	0.0236	0.0230	0.0113	0.0236
Refl	0.576	0.619	0.651	0.576	0.619	0.651
E_{dir}	0.7907	0.8278	0.8399	0.7043	0.7410	0.7530
E_{dif}	0.0877	0.0663	0.0395	0.0836	0.0634	0.0380
L_{path}	0.0080	0.0068	0.0048	0.0072	0.0060	0.0042
L_T	0.16028	0.17546	0.16853	0.14343	0.15755	0.15072

E_{dir} = Downward direct solar irradiance at the ground, $\cos\theta_z \exp(-\tau_{ext} \sec\theta_z)$

E_{dif} = Downward diffuse solar irradiance at the ground

L_{path} = Upward path radiance at the TM,

$$\frac{L_T - (E_{dir} + E_{dif}) \exp(-\tau_{ext} \sec 5^\circ)\, \rho}{\pi}$$

L_T = Total radiance at the TM at a 5° nadir angle

All irradiance and radiance values are normalized for an exoatmospheric solar irradiance of 1.

Table 5.14 Computed Radiance at Landsat Sensors

Band	L (mW cm^{-2} sr^{-1} μm^{-1})
	North Site
2	26.6269
3	24.8167
4	15.8268

perature stabilization of the solar radiometer. It is difficult to assess the magnitude of this uncertainty. However, the measurement attempt was worthwhile because of the experience gained in instrument operation and data reduction.

Comparison to Preflight Calibration

To compare our predicted radiance values to those determined from preflight gains and offsets (Table 1.2), we identified the north site on the digital image knowing that the southeast blanket was 28.6 m from the nearest corner of the building. The distances between this building and the dark helicopter landing pad are also known, the latter appearing as a darker pixel in the digital image.

Once the site was identified, 16 digital counts were averaged. As band 1 was saturated, and as no solar radiometer measurements were taken in the near infrared, only bands 2 through 4 were inspected. Our test site was misaligned to the north/south scan lines of Landsat; hence the 16 pixels used in the average formed a diamond pattern, with an edge 45° from the Landsat pixel edges. As average counts were used, so too were average gain and offset values used in the calculation (thus it was not individual detectors that were calibrated, but rather a band average). Detector 8 was, however, identified as going through the top of the road, as the northernmost detector of the digitized quadrant was detector 16. Table 5.15 gives the radiances determined from the preflight data base. Difference in these radiances, and those determined from our ground-based calibration, were 6.0%, 8.7%, and -12.4% for bands 2, 3, and 4, respectively.

Table 5.15 Radiances Computed from Preflight Calibration Gains and Offsets

Band	Gain	Offset	Count	L_{pre}	%CH
2	7.8595	1.6896	199.2	25.1301	6.0
3	10.2031	1.8850	234.9	22.8377	8.7
4	10.8206	2.2373	197.75	18.0686	-12.4

L_{pre} = (average count - offset)/gain

$$\%CH = \frac{(L_{Ground} - L_{Pre})*100}{L_{Pre}}$$

Diffuse/Direct Data

The analysis of the diffuse/direct ratio, as obtained from measurements made on July 8, 1984, is given in Table 5.16. The total irradiance incident on the ground was first measured, by taking a reading, using the MMR, of the radiance of a reference panel. On this date the Barnes MMR S#116 and a $BaSO_4$ panel were used. The diffuse component of solar irradiance was measured by blocking the sun with a styrofoam parasol, and taking a reading from the reference panel. The

Table 5.16 Diffuse/Direct Ratios

Time	(θ_z)	MMR band			
		1	2	3	4
Measured ratios:					
8:50.0	(57.77°)	0.3349	0.2588	0.2114	0.1682
8:51.0	(57.56°)	0.3322	0.2572	0.2092	0.1676
8:59.0	(55.90°)	0.3182	0.2476	0.2035	0.1636
9:13.0	(52.98°)	0.2960	0.2328	0.1948	0.1579
9:22.0	(51.10°)	0.2847	0.2247	0.1887	0.1535
9:29.0	(49.63°)	0.2747	0.2174	0.1839	0.1496
9:29.4	(49.55°)	0.2729	0.2160	0.1824	0.1486
9:41.1	(47.10°)	0.2588	0.2057	0.1745	0.1428
9:41.6	(46.99°)	0.2587	0.2054	0.1731	0.1421
9:52.9	(44.62°)	0.2488	0.1985	0.1679	0.1382
9:53.5	(44.50°)	0.2476	0.1983	0.1694	0.1393
10:04.5	(42.19°)	0.2369	0.1896	0.1603	0.1302
10:05.0	(42.09°)	0.2365	0.1895	0.1607	0.1316
10:11.2	(40.79°)	0.2313	0.1857	0.1578	0.1293
10:11.6	(40.71°)	0.2307	0.1856	0.1587	0.1312
		TM band			
		1	2	3	4
Predicted ratios from Herman code output:					
	(25°)	0.2483	0.1688	0.1265	0.0795
	(35°)	0.2680	0.1811	0.1355	0.0853
	(45°)	0.3012	0.2016	0.1502	0.0947
	(55°)	0.3600	0.2368	0.1751	0.1108
	(65°)	0.4809	0.3060	0.2226	0.1411

difference between the total and diffuse readings gave the direct component. In the table, these ratios are compared with that predicted by the Herman radiative code. It is hoped that, on future calibrations, data such as these can be used to validate our calibration, or to adjust certain input parameters to achieve more accurate results. Progress in this area is reported by Capron (1985).

CHAPTER 6

SENSITIVITY OF COMPUTED RADIANCE TO THE INPUT PARAMETERS OF THE HERMAN CODE

In this chapter we analyze the sensitivity of computed radiance to the following Herman code input parameters:

(1) Tau components: τ_{Ray}, τ_{Mie}, τ_{oz}, and τ_{H_2O}

(2) Aerosol phase function parameters: distribution slope (i.e., Junge ν), refractive index

(3) Vertical distributions: pressure, aerosol, ozone, water vapor, and surface elevation

(4) Non-Lambertian surfaces

(5) Multiple scattering: number of iterations, $\Delta\tau$ layer thickness

Each input is varied in turn, and the Herman radiative transfer code is run to determine the effect on computed radiance. For each individual Herman code run, all input parameters are held constant except the one under study. The constant parameters are those that were defined in Chapter 4 and are considered representative for White Sands. They are summarized in Table 6.1. The aerosol phase function is determined assuming a refractive index of 1.54-0.01i and a Junge radial size distribution with $\nu = 2.5$. Tau components are computed assuming a visibility of 100 km, barometric pressure of 900 mbar, and number densities of 255 matm-cm and 0.1 g cm^{-2} km^{-1} for ozone and water vapor, respectively. A solar zenith angle of 45° and a range of surface reflectances are assumed. TM bands 1, 2, and 5 were selected for study. Band 1 contains the greatest amount of multiple scattering,

Table 6.1 Model Parameters for White Sands

- Aerosol phase function inputs:
  - Radial size distribution: Junge with $\nu = 2.5$
  - Radial limits: 5.02 to 0.02 μm in steps of 0.04 μm
  - Refractive index: 1.54-0.01i
- Tau components determined from:
  - Visibility: 100 km
  - Surface barometric pressure: 900 mbar
  - Ozone number density: 255 matm-cm
  - Water vapor number density: 0.1 g cm^{-2} km^{-1}
- Solar zenith angle: 45°
- Surface reflectance factors: 0, 0.15, 0.50, 0.75
- Surface elevation: 1.19 km (Herman code input IHGT = 23)
- $\Delta\tau$ layer thickness: 0.02
- Number of iterations: As required for convergence to <0.5%

band 2 the greatest amount of ozone, and band 5 the greatest amount of water vapor. After the selected input parameter is varied, the percentage changes in the E_{dir}, E_{dif}, L_{path}, and L_T components are tabulated. These are the direct and diffuse irradiances incident at the ground, the upwelling path, and total radiances reflected back out to space at a 5° zenith angle and 90° azimuth angle. Complete job summaries are not included here, but have been distributed as an internal memo and are available upon request (Kastner, 1985). Here only the percentage changes in L_T are given.

It is found that many of the uncertainties for a given input parameter are a function of ground reflectance. Because of this, a model reflectance factor for White Sands is desired. Table 6.2 gives some laboratory reflectometer data, which provide the reflectance of gypsum sand as a function of four levels of moisture content. Diffuse

Table 6.2 Laboratory Reflectance Data for Gypsum Sand

λ (μm)	Dry sand 1	Dry sand 2	Wet sand 1	Wet sand 2
0.488	0.456	0.454	0.382	0.314
0.560	0.500	0.504	0.433	0.357
0.659	0.528	0.534	0.469	0.390
0.834	0.555	0.549	0.498	0.409
1.21	0.500	0.514	0.442	0.331
2.26	0.207	0.175	0.156	0.109

illumination was provided using an integrating sphere. Then, light reflected normal to the surface was collected with a monochromator. The sand was compared with two reference surfaces (a silver and a black plate) to determine absolute reflectance. A study of these data and those measured at White Sands yields a model value of 0.5 for TM bands 1 through 5. A reflectance of 0.15 is selected for TM band 7.

Optical Depth

When careful solar irradiance measurements are made, spectral optical depths can be determined to a high degree of accuracy. A Langley plot is made of the log voltage versus air mass, the slope of which yields the extinction optical thickness of the atmosphere τ_{ext}. Sources of error can fall into one of three categories: (1) instrumentation errors, (2) errors imposed by the atmosphere, and (3) errors associated with determining air mass given the time of day as input. The solar radiometer need not be calibrated in an absolute sense to determine optical depth; hence absolute calibration errors are not of concern. Shaw (1976) has summarized the instrument errors associated with a solar radiometer of his. It is linear to 1% over a range of irradiance extending from E_0 to $10^{-3}E_0$, where E_0 is the solar irradiance. It is stable to ±1% over a 10-month period, and has a readout accuracy of 0.2%. If this instrument is representative, then our instrumentation errors are no greater than 2%. In the next section it is shown that the errors associated with an uncertainty in air mass have a negligible effect on the determination of optical depth. The greatest source of error in determining extinction optical depth, therefore, is the temporal variability of the atmosphere. On clear days on which we have collected data at White Sands, we have found the percentage standard deviation of optical depth has ranged from 2% for the short wavelengths (0.4 μm), to between 4% and 8% for the short wave infrared channel (1.03 μm). As a worst case, an uncertainty of 10% in extinction optical depth is assumed.

Air Mass/Time of Day Errors

Palmer (1982) defined a set of requirements to allow the exoatmospheric solar irradiance to be determined, from the Langley technique, to within 0.1%. These requirements are that the hour angle (and hence the time of day with which each measurement must be taken) be determined to 0.1 sec, and that latitude and solar declination be known to within 1 arc sec. Our interest is not to determine solar irradiance, but rather to measure extinction optical depth, and therefore we redefine the above requirements on hour angle, latitude, and declination using a parallel analysis and the constraint that optical depth be determined to within 2%. It is desired that the uncertainty in this optical depth be limited only by instrumentation errors (assuming a temporally stable atmosphere), and not by the accuracy with which air mass can be determined. The 2% uncertainty in τ_{ext} is more than adequate to allow the computation of upwelling radiance to within 0.5%.

The Langley technique is based on the logarithm of Beer's law, given in Eq. (5.2). By differentiating this equation one obtains

$$m \, d\tau_{ext} + \tau_{ext} \, dm = \frac{dE_0}{E_0} - \frac{dE}{E} \; . \qquad (6.1)$$

Thus the tolerance in m, for an allowed uncertainty in τ_{ext}, can be determined. First the relative error in measured irradiance is taken equal to the relative error in intercept irradiance E_0. The latter can be determined by averaging the intercepts for several days in which measurements were made under clear, stable conditions, preferably at higher altitudes. This leads to

$$\frac{dm}{m} = - \frac{d\tau_{ext}}{\tau_{ext}} = 0.02 \; . \qquad (6.2)$$

Evaluating this expression yields dm = 0.02 at air mass 1, and dm = 0.13 at air mass 6.5.

Of greater interest is the requirement on solar zenith angle and time of day. Using the geometric approximation to air mass, the quantities m, θ_z, and h can be interrelated using

$$m = \sec\theta_z \tag{6.3}$$

and

$$1/m = \cos\theta_z = \sin\phi\,\sin\delta + \cos\phi\,\cos\delta\,\cos h\ . \tag{6.4}$$

Here ϕ is the latitude of the observer, δ the solar declination, and h the hour angle measured from true solar noon. Beginning with the derivative of Eq. (6.3), one finds

$$d\theta_z = \frac{\cos\theta_z\, dm}{\tan\theta_z} = \frac{dm/m}{\tan[\cos^{-1}(1/m)]}\ . \tag{6.5}$$

Evaluating this at $dm/m = 0.02$ yields $d\theta_z = \infty$ at air mass 1, or $d\theta_z = 0.1784°$ (10.7 arc min) at air mass 6.5. This states that a large uncertainty in solar zenith angle can be tolerated with the sun directly overhead, but that it must be known to within 10.7 arc min for θ_z approximately 81°. (A finite difference calculation yields an allowable uncertainty of $d\theta_z = 11.4°$ at $m = 1$, and $d\theta_z = 0.1749°$ at $m = 6.5$.)

The derivative of Eq. (6.4) is next taken in order to assess the allowable uncertainty in time of day. This derivative is

$$\frac{dm}{dh} = m^2\,(\cos\phi\,\cos\delta\,\sin h)\ . \tag{6.6}$$

Using the White Sands latitude $\phi = 32.9°$ and three values of δ (−23.45°, 0°, and 23.45°, corresponding to the winter solstice, the equinoxes, and the summer solstice) the uncertainty in hour angle dh is computed. The uncertainty in local time follows, since 15° in hour angle equals 1 hour of time. Results are given in Table 6.3. As air mass approaches unity the allowed uncertainty in time becomes infinitely large. The most stringent requirements are found at an air mass of 6.5. At worst the time must be known to 51 sec (at $\delta = 0$). Thus the determination of time of day is far less critical than for the case where exoatmospheric irradiance is of interest. Because we record data to the nearest second, we anticipate that errors resulting from uncertainties in time will be negligible.

Table 6.3 Tolerable Uncertainty in Time of Day and Solar Declination

m	δ	h	$\frac{dm}{dh}$	dh(°)	d (sec)	$\frac{dm}{d\delta}$	$d\delta$ (arc min)
2.0	-23.45	21.61	1.1345	2.020	485	-3.2359	-42.4957
4.0	-23.45	52.76	9.8113	0.467	112	-11.2083	-24.5371
6.5	-23.45	61.29	28.5436	0.261	63	-27.8347	-16.0557
2.0	0.00	53.45	2.6980	0.849	204	-2.1727	-63.2899
4.0	0.00	72.68	12.8246	0.357	86	-8.6908	-31.6450
6.5	0.00	79.44	34.8733	0.214	51	-22.9491	-19.4738
2.0	23.45	68.38	2.8643	0.800	192	-1.5008	-91.6274
4.0	23.45	87.48	12.3125	0.372	89	-7.7381	-35.5410
6.5	23.45	94.64	32.4374	0.230	55	-22.1956	-20.1349

The uncertainties dh and $d\delta$ were computed for dm = 0.02.

Equation (6.4) can again be differentiated to determine the required accuracy in solar declination. This derivative is

$$\frac{dm}{d\delta} = m^2 (\cos\phi \sin\delta \cos h - \sin\phi \cos\delta) \quad (6.7)$$

At the worst case of $m = 6.5$, the requirement on $d\delta$ is found to be 16 arc min. Again, this condition is easily satisfied. Because δ and ϕ can be interchanged within Eq. (6.7), the uncertainty in latitude is found to be equal to the uncertainty in declination, or 16 arc min. To summarize, the allowable uncertainties are

$\theta_z = 10.7$ arc min

time = 51 sec

ϕ or $\delta = 16$ arc min

Rayleigh Optical Depth

The Rayleigh component of optical depth τ_{Ray} is determined from the surface measured barometeric pressure and Eq. (2.40). The barometer can be read to within 0.2 mbar, and is calibrated by the Atmospheric Sciences Laboratory (ASL) at White Sands several times a year. Other sources of uncertainty for this parameter may be attributed to the uncertainty of columnar number density, the wavelength dependence of refractive index, and the anisotropy parameter. A 2% uncertainty in τ_{Ray} is assumed.

Table 6.4 summarizes the results of varying τ_{Ray} by both 2% and 10% of its model value (compared to a value determined from an atmospheric pressure of 900 mbar). For the assumed uncertainty of 2%, the change in radiance is less than 0.1% for $\rho = 0.50$. A change of less than 2% was noted in bands 1 and 2 when $\rho = 0$. The deviation in τ_{Ray} that can be expected throughout the year is less than 10% of the mean value. The data in Table 6.4 suggest, therefore, that even

C-3

Table 6.4 Percentage Change in Radiance Due to Variations in Herman Code Inputs

Change in parameter	Band 1				Band 2				Band 5			
	ρ=0	ρ=0.15	ρ=0.50	ρ=0.75	ρ=0	ρ=0.15	ρ=0.50	ρ=0.75	ρ=0	ρ=0.15	ρ=0.50	ρ=0.75
τ_{Ray} (900 mbar)												
2%	1.74	0.42	0.03	-0.01	1.64	0.24	0.02	-0.01	0.	.0	0.	0.
10%	8.71	2.11	0.16	-0.04	8.17	1.19	0.07	-0.03	0.97	0.02	0.	0.
τ_{Mie} (100 km)												
2%	0.24	-0.01	-0.08	-0.09	0.40	-0.01	-0.07	-0.08	1.87	-0.01	-0.03	-0.03
10%	1.22	-0.02	-0.39	-0.42	1.93	-0.05	-0.34	-0.35	9.52	-0.04	-0.17	-0.16
23 km	16.21	-0.22	-5.15	-5.70	26.98	-0.43	-4.74	-4.97	135.05	-0.35	-2.44	-2.28
200 km	-3.53	0.10	1.15	1.24	-5.73	0.17	1.05	1.05	-27.77	0.13	0.52	0.45
τ_{Mie} (23 km)												
10%	2.40	-0.01	-0.93	-1.05	3.74	-0.04	-0.86	-0.94	10.54	-0.03	-0.44	-0.43
τ_{oz} (255 matm-cm)												
10%	-0.16	-0.17	-0.18	-0.17	-0.64	-0.67	-0.67	-0.68	N/A	N/A	N/A	N/A
30%	-0.47	-0.48	-0.49	-0.49	-1.95	-1.99	-1.99	-2.01	N/A	N/A	N/A	N/A
τ_{oz} (337 matm-cm)												
10%	-0.21	-0.21	-0.21	-0.22	-0.86	-0.89	-0.90	-0.90	N/A	N/A	N/A	N/A
30%	-0.60	-0.62	-0.63	-0.64	-2.53	-2.62	-2.65	-2.65	N/A	N/A	N/A	N/A
τ_{H_2O} (0.1 g cm^{-2} km^{-1})												
10%	N/A	N/A	N/A	N/A	N/A	N/A	N/A	N/A	-0.26	-0.61	-0.62	-0.63
30%	N/A	N/A	N/A	N/A	N/A	N/A	N/A	N/A	-0.77	-1.82	-1.86	-1.89
0.01 g cm^{-2} km^{-2}	N/A	N/A	N/A	N/A	N/A	N/A	N/A	N/A	1.48	3.46	3.57	3.62
1.0 g cm^{-2} km^{-1}	N/A	N/A	N/A	N/A	N/A	N/A	N/A	N/A	-12.59	-28.68	-29.24	-29.46
τ_{H_2O} (1.0 g cm^{-2} km^{-1})												
10%	N/A	N/A	N/A	N/A	N/A	N/A	N/A	N/A	-1.31	-3.84	-3.92	-3.94
30%	N/A	N/A	N/A	N/A	N/A	N/A	N/A	N/A	-3.82	-11.10	-11.34	-11.4
10 g cm^{-2} km^{-1}	N/A	N/A	N/A	N/A	N/A	N/A	N/A	N/A	-45.73	-94.79	-96.08	-96.28

Table 6.4--Continued

Change in parameter	Band 1				Band 2				Band 5			
	ρ=0	ρ=0.15	ρ=0.50	ρ=0.75	ρ=0	ρ=0.15	ρ=0.50	ρ=0.75	ρ=0	ρ=0.15	ρ=0.50	ρ=0.75
Imaginary index (1.54-0.01i)												
1.54-0.0001i	4.39	3.75	3.93	4.24	5.58	3.50	3.45	3.65	17.33	1.69	1.49	1.53
1.54-0.001i	3.79	3.26	3.42	3.68	4.80	3.05	3.01	3.18	15.31	1.51	1.33	1.37
1.54-0.1i	-10.63	-9.35	-9.69	-10.28	-13.68	-9.08	-8.89	-9.28	-50.90	-5.98	-5.38	-5.50
Real index (1.54-0.01i)												
1.50-0.01i	-1.11	-0.31	-0.10	-0.09	-1.76	-0.29	-0.06	-0.07	-8.05	-0.13	0.	0.
1.52-0.01i	-0.55	-0.16	-0.05	-0.04	-0.88	-0.14	-0.03	-0.03	-4.05	-0.07	0.	0.
1.60-0.01i	1.54	0.42	0.11	0.09	2.68	0.44	0.10	0.07	12.02	0.20	0.	-0.01
Refractive index (1.54-0.01i)												
1.52-0.003i	2.13	2.19	2.43	2.62	2.53	2.08	2.18	2.29	7.07	1.07	1.02	1.04
Junge ν (2.5)												
2.3	-1.69	-0.75	-0.54	-0.55	-2.28	-0.63	-0.40	-0.42	-5.41	-0.13	-0.04	-0.04
3.0	4.28	1.35	0.54	0.51	6.05	1.09	0.33	0.29	14.96	-0.01	-0.28	-0.29
4.0	14.14	2.07	-1.68	-2.21	20.86	0.90	-2.54	-2.97	14.60	-5.08	-5.65	-5.83
Vertical distributions (exoatmospheric)												
Pressure												
Random	-39.62	-11.38	-2.75	-1.62	-16.85	-2.46	-0.01	0.25	0.21	0.	-0.01	-0.01
Linear	-0.22	-0.01	0.08	0.13	-0.24	0.	0.08	0.10	-0.08	0.	0.	0.01
Accentuated	-40.41	-11.54	-2.78	-1.66	-17.86	-2.65	-0.07	0.22	0.25	0.	-0.01	-0.01
Aerosol												
Random	14.19	4.03	1.32	1.28	27.54	5.33	1.66	1.31	-43.54	-6.65	-6.18	-6.29
Linear	0.19	0.01	-0.08	-0.12	0.17	0.	-0.04	-0.07	-0.54	0.01	0.04	0.05
Accentuated	14.82	4.66	1.45	0.97	25.82	4.50	1.02	0.71	-25.02	-3.35	-3.02	-3.06

Table 6.4--Continued

Change in parameter	Band 1				Band 2				Band 5			
	$\rho=0$	$\rho=0.15$	$\rho=0.50$	$\rho=0.75$	$\rho=0$	$\rho=0.15$	$\rho=0.50$	$\rho=0.75$	$\rho=0$	$\rho=0.15$	$\rho=0.50$	$\rho=0.75$
Ozone												
Random	-0.01	0.	0.	0.	0.	0.	0.01	0.	N/A	N/A	N/A	N/A
Linear	0.45	0.08	-0.11	-0.18	2.06	0.20	-0.31	-0.52	N/A	N/A	N/A	N/A
Accentuated	-0.03	0.	0.01	0.01	-0.14	0.	0.04	0.05	N/A	N/A	N/A	N/A
Water vapor												
Random	N/A	N/A	N/A	N/A	N/A	N/A	N/A	N/A	-0.04	0.	0.	0.01
Linear	N/A	N/A	N/A	N/A	N/A	N/A	N/A	N/A	0.23	0.	-0.01	-0.02
Accentuated	N/A	N/A	N/A	N/A	N/A	N/A	N/A	N/A	0.37	-0.01	-0.02	-0.03
IHGT = 1	0.27	0.04	-0.07	-0.12	0.19	0.01	-0.04	-0.07	-0.78	0.02	0.06	0.08
Non-Lambertian surface												
5%	0.	0.41	0.69	0.83	0.	0.41	0.60	0.67	0.	0.36	0.39	0.41
10%	0.	0.82	1.38	1.67	0.	0.83	1.18	1.35	0.	0.72	0.79	0.83
20%	0.	1.65	2.76	3.37	0.	1.65	2.36	2.72	0.	1.42	1.56	1.65
Multiple scattering												
No. of iterations	3	4	4	5	3	3	4	4	3	3	3	3
Change from 1st pass	-7.84	-16.15	-31.57	-40.16	-4.39	-11.93	-26.16	-34.19	-0.17	-5.19	-14.32	-19.89
$\delta\tau = 0.04$	-0.03	-0.02	-0.02	-0.01	0.	0.	0.	0.	0.	0.	0.	0.
Surface reflectance 2%	0.	1.32	1.85	2.02	0.	1.58	1.94	2.03	0.	1.95	2.01	2.02
Cum. uncertainty	5.19	3.99	4.04	4.36	5.71	3.38	3.32	3.54	16.48	1.23	1.03	1.07

Radiances computed using new parameters are compared to radiances computed using model parameters in parentheses; that is, percentage change = $100(L_{new} - L_{model})/L_{model}$. Cumulative uncertainty found from simultaneous changes of τ_{Ray} (by 2%), τ_{Mie} (by 10%), τ_{oz} (by 10%), τ_{H_2O} (by 30%), n (to 1.52-0.003i), and ρ (by 2%).

model data for this parameter are fairly accurate for all but a surface reflectance of zero.

Mie Optical Depth

The uncertainty in Mie optical depth is assumed equal to the uncertainty in extinction optical depth. This is justified in that the Rayleigh component can be determined to a much higher level of certainty, and for the solar radiometer wavelengths for which there is no molecular absorption τ_{Mie} is determined as the difference of τ_{ext} and τ_{Ray}. At other wavelengths τ_{Mie} can be accurately interpolated, as it is a slowly varying function. Thus a 10% level of uncertainty in τ_{Mie} is assumed although it is quite possible that this parameter can often be measured to within 2%.

To assess the impact on the uncertainty of τ_{Mie}, we ran the Herman code with several values of this parameter. Inputs representing a 2% and a 10% deviation from model values of τ_{Mie} were used, as well as inputs corresponding to visibilities of 23 km and 200 km. Table 6.4 compares these results to the radiances computed in the model atmosphere (having a visibility of 100 km). The errors in computed radiance due to the anticipated 10% error in τ_{Mie} are -0.4%, -0.3%, and -0.2% for bands 1, 2, and 5 at a reflectance of 0.50. Larger changes in radiance (10% for band 5) are noted when the reflectance is zero. This seems to be a result of small changes in radiances having a large effect on the percentage changes, when the initial radiances were also small. The change in radiance for all other reflectances, including $\rho = 0.15$, are less than 0.5%. Errors on the order of 5% ($\rho = 0.50$) result when erroneous model data are used (for example, assuming a visibility of 23 km when the actual visibility is 100 km). Such errors in τ_{Mie} are not representative, in that measured values of τ_{Mie} are used in the calibrations. Finally, a 10% deviation in τ_{Mie} is studied at solar zenith angles 25° and 65°. These results, given in Table 6.5, show that the radiances differ by approximately 0.1% from the 45° study, and indicate that the radiances computed at large solar zenith angles will be slightly less accurate.

To model the uncertainty in radiance due to an uncertainty in either τ_{Mie} or τ_{Ray}, we use a simplified radiative transfer equation,

$$L_T = (E_{Dir} + E_{Dif}) \exp(-\tau_{ext}) \rho/\pi + L_{Path} \qquad (6.8)$$

where

$$E_{Dir} = \mu_0 \exp(-\tau_{ext}/\mu_0)$$

$$E_{Dif} = A[1 - \exp(-\tau_s/\mu_0)]$$

$$L_{Path} = B[1 - \exp(-\tau_s/\mu_0)]$$

and

$$\mu_0 = \cos(\theta_z)$$

$$\tau_{ext} = \tau_{Ray} + \tau_{Mie} + \tau_{abs}$$

$$\tau_s = \tau_{Ray} + \tau_{Mie} .$$

L_T is the normalized radiance incident at an in-orbit sensor, and θ_z is the solar zenith angle. The A and B coefficients are determined for a

Table 6.5 Percentage Change in Radiance at Solar Zenith Angles of 25° and 65°

Change in parameter	Band 1				Band 2				Band 5			
	$\rho=0$	$\rho=0.15$	$\rho=0.50$	$\rho=0.75$	$\rho=0$	$\rho=0.15$	$\rho=0.50$	$\rho=0.75$	$\rho=0$	$\rho=0.15$	$\rho=0.50$	$\rho=0.75$
$\theta_z = 25°$												
τ_{Ray} 2%	1.71	0.39	0.04	0.	1.59	0.22	0.02	0.	0.	0.	0.	0.
τ_{Mie} 10%	1.23	0.02	-0.30	-0.31	1.99	0.03	-0.24	-0.24	9.28	0.05	-0.10	-0.08
τ_{oz} 10%	-0.14	-0.15	-0.16	-0.15	-0.56	-0.58	-0.59	-0.59	N/A	N/A	N/A	N/A
τ_{H_2O} 30%	N/A	N/A	N/A	N/A	N/A	N/A	N/A	N/A	-0.62	-1.58	-1.63	-1.65
1.52-0.003i	3.51	2.49	2.39	2.51	5.10	2.44	2.16	2.22	18.29	1.36	1.03	1.02
$\theta_z = 65°$												
τ_{Ray} 2%	1.63	0.51	0.03	-0.04	1.54	0.30	0.01	-0.03	0.	0.	0.	0.
τ_{Mie} 10%	1.39	0.02	-0.56	-0.65	2.24	-0.03	-0.57	-0.63	9.81	-0.06	-0.35	-0.36
τ_{oz} 10%	-0.23	-0.23	-0.24	-0.24	-0.90	-0.93	-0.94	-0.94	N/A	N/A	N/A	N/A
τ_{H_2O} 30%	N/A	N/A	N/A	N/A	N/A	N/A	N/A	N/A	-1.10	-2.48	-2.56	-2.59
1.52-0.003i	2.61	2.76	3.04	3.26	2.83	2.62	2.74	2.87	5.17	1.36	1.28	1.31

Percentage change = $100(L_{new} - L_{model})/L_{model}$

given set of input parameters from the E_{Dif} and L_{Path} outputs of the Herman code. For example, for model conditions $\lambda = 0.571$ µm and $\rho = 0.5$ we find $A = 0.5$ and $B = 0.1$.

By differentiating Eq. (6.8) with respect to τ_i, where τ_i is either τ_{Ray} or τ_{Mie}, the change in computed radiance for a given change in τ_i is determined:

$$\frac{\delta L_T}{\delta \tau_i} = \left[\frac{\delta}{\delta \tau_i}(E_{Dir} + E_{Dif})\right] \frac{\rho}{\pi} \exp(-\tau_{ext}) + (E_{Dir} + E_{Dif}) \frac{\rho}{\pi} \left[\frac{\delta}{\delta \tau_i} \exp(-\tau_{ext})\right] + \frac{\delta L_{Path}}{\delta \tau_i} . \tag{6.9}$$

The following terms are substituted:

$$\frac{\delta E_{Dir}}{\delta \tau_i} = -\exp(-\tau_{ext}/\mu_0)$$

$$\frac{\delta E_{Dif}}{\delta \tau_i} = \frac{A}{\mu_0} \exp(-\tau_s/\mu_0) \tag{6.10}$$

$$\frac{\delta L_{Path}}{\delta \tau_i} = \frac{B}{\mu_0} \exp(-\tau_s/\mu_0)$$

It is apparent that the change in radiance δL_T for a given $\delta \tau_i$ will be highly dependent on the specific values of the parameters A, B, μ_0, τ_{ext}, τ_s, and ρ. For example, it is interesting to inspect Eq. (6.9) as a function of surface reflectance ρ. As τ_i is increased, the direct component E_{dir} is reduced as light is scattered out of the direct solar beam. This effect is more or less offset by an increase in E_{Dif}. The change in the upwelling direct radiance, given by the second term of Eq. (6.9), is also reduced as τ_i is increased. For moderate values of ρ, however, this effect is balanced by an increase in path radiance. Only as ρ approaches zero does a 10% change in τ_i cause δL_T to become significant (>0.5% of L_T).

Ozone Optical Depth

In King and Byrne (1976) an error analysis of the determination of ozone concludes that the uncertainty is on the order of 20 matm-cm. This is 8% of the mean ozone value. Our own analysis suggests that differences in τ_{oz} of 15% can occur due to an uncertainty in the Junge ν parameter used to characterize the aerosol radial size distribution.

Ozone absorption is present in bands 1 through 4. It is significant, however, only in band 2 where the ozone absorption coefficient is large. For this reason band 2 is used to estimate the uncertainty in radiance due to an uncertainty in τ_{oz}. Table 6.4 summarizes the variation in computed radiance for a 10% and 30% change in τ_{oz}. For band 2 the resulting changes in radiance were -0.7% and -2.0%, respectively. Only a slight dependence on ground reflectance is observed. At larger solar zenith angles there is an increase in the uncertainty in computed radiance. From Table 6.5 the uncertainty is found to increase to -0.9% at $\theta_z = 65°$ for a 10% deviation in τ_{oz}. The change in radiances from an ozone number density of 337 matm-cm is also studied. The percentage changes in radiance were -0.9% and

-2.6% for deviations of 10% and 30%. This ozone amount is far in excess of that expected at the test site. The expected deviation is 212 to 298 matm-cm, the model White Sands value being 255 matm-cm. This range is within 30% of the mean. Because of this, the uncertainty in radiance that results from using a model value for τ_{OZ} is no greater than 3%, and the uncertainty in radiance when using measured data is estimated to be 0.7%.

Water Vapor Optical Depth

Water vapor absorption affects TM bands 4, 5, and 7. The percentage change in radiance is expected to be greatest for band 5. This band, therefore, is used to model the uncertainty in computed radiance. For mean White Sands conditions ($NH_2O = 0.1$ g cm^{-2} km^{-1}), the percentage changes in radiances are -0.6% and -1.9% respectively for changes in τ_{H_2O} of 10% and 30% ($\rho = 0.50$). As the amount of water vapor is increased, the uncertainty in computed radiance increases for a given percent uncertainty in τ_{H_2O}. For example, at $NH_2O = 1.0$ g cm^{-2} km^{-1}, the changes in radiance corresponding to these same changes in τ_{H_2O} are -3.9% and -11.3%.

It is difficult to assess what our uncertainty in τ_{H_2O} is at present. This uncertainty is a function of how accurate the LOWTRAN spectral transmittance data are, and how well we can infer the columnar number density of water vapor from temperature and ground measured relative humidity. It is doubtful that this technique has an uncertainty less than 30%.

Currently, the spectropolarimeters are being equipped with a filter set matched to TM bands 5 and 7. When functional they will allow us to measure the in-band optical depth and give a representative value of τ_{H_2O} for each TM band. (Narrowband filters will still be used to measure the spectral dependence of τ_{Mie}.) With these data the uncertainty in determining τ_{H_2O} can be reduced, and the uncertainty in its value can be better assessed.

Aerosol Phase Function Parameters

The greatest source of error in the calibration methodology seems to be due to the input parameters used in computing the aerosol scattering phase function. The radial size distribution, size distribution limits, and complex refractive index are all used to determine this function and the single-scatter albedo.

The greatest variation in output radiance seems to result from our uncertainty in the imaginary component of refractive index. Table 4.3 suggests that this parameter may be known only to within an order of magnitude. We chose a model value of 0.01i for all our calculations. This value most closely matches the measured refractive index of the smaller particles. A more appropriate model value for the larger particle mode is 0.003i at a wavelength of 0.55 µm, or 0.001i at 1.06 µm. To assess the impact of this uncertainty on computed radiance, we ran the Herman code for the model parameters and compared the output with that using an imaginary refractive index of 0.001i. For a reflectance of 0.50, the largest change in radiance occurred at the shorter wavelengths. At 0.486 µm (TM band 1) the percentage change in radiance, going from 0.01i to 0.001i, was 3.4%. This decreased to 1.3% for 1.68 μm (TM band 5). A change of -10% was noted when the index used was increased from 0.01i to 0.1i (TM band 1). A variance of this degree is unlikely, however. As the wavelength decreased, the difference in percentage changes for different surface reflectances grew. At 0.486 μm, the percentage changes in radiance were comparable for $\rho = 0$, 0.50, and 0.75. At 1.68 μm, however, the percentage changes for these same ground reflectances were 15%, 1.3%, and 1.4% (using the 0.001i data). At this wavelength, actual radiances for the model case were less than 0.001 $\mathrm{mW\ cm^{-2}\ \mu m^{-1}\ sr^{-1}}$ for $\rho = 0$, but greater than 0.03 $\mathrm{mW\ cm^{-2}\ \mu m^{-1}\ sr^{-1}}$ for all other ρ.

The effect of the real index component was less significant. Real values of 1.50, 1.52, and 1.60 were used while the imaginary component remained at 0.01i. For all reflectances except $\rho = 0$, the percentage changes in radiances were less than 0.5%. As a worst case, consider $n = 1.60-0.01i$. For a wavelength of 0.486 μm, percentage differences were 1.5%, 0.4%, 0.1%, and 0.1% for reflectances of 0, 0.15, 0.50, and 0.75. At a wavelength of 1.68 μm, these differences were 12%, 0.2%, 0%, and 0%. The change in radiance was also studied for the case $n = 1.52-0.003i$. Here both the real and imaginary components are varied simultaneously to a degree that is representative of their expected deviation. The changes in radiance were 2.4%, 2.2%, and 1.0% for the three bands at $\rho = 0.50$.

To study the effect of radial size distribution, we varied the Junge ν parameter from 2.5. In most cases, the percentage changes in radiance were less than 0.5% for $\delta\nu < |0.5|$. The exceptions were for a reflectance of 0, and for TM band 5. For example, at 0.486 µm and $\nu = 3.0$ the percentage changes for reflectances of 0, 0.50, and 0.75 were 4.3%, 0.5%, and 0.5%, while at 1.68 µm the changes were 15.0%, -0.3%, and -0.3%. When ν was set equal to 4.0, the percentage change in radiances, at $\rho = 0.50$, ranged from -1.7% to -5.6% through the wavelength range 0.486 µm to 1.68 µm. Although this would imply a large uncertainty in computed radiance, such an uncertainty in ν is unlikely.

Vertical Distributions

To study the impact on computed upwelling radiance (exoatmospheric), we varied the aerosol, pressure, ozone, and water vapor vertical profiles one at a time. Three types of deviations were modeled: "random," "linear," and "accentuated." In the random study, the number density for a particular layer was modified by a multiplicative factor, Gaussian distributed about the actual number density, and having a standard deviation of 0.25. For the linear study, the total optical depth at a given layer was decreased by a factor that increased by 1% per layer, moving up the atmosphere. In the accentuated study, the profiles were nonlinearly decreased or increased, depending on whether the layer number was smaller or larger than the mean.

Results, as given in Table 6.4, were inconclusive. When only the ozone or water profile was varied, neither deviation model affected the computed radiances. However, large deviations (approximately 6% for band 5) were noted for the aerosol study in which the random model was used. Here, however, layer number densities varied, on the average, by 25%. Also, large deviations (on the order of 3%) were noted in the pressure profiles for band 1, for both the random and accentuated studies. To estimate the uncertainty that results from our choice of model profiles, more information is needed as to the expected profile deviations.

The surface elevation is input into the Herman code by the parameter IHGT. For IHGT = 23, corresponding to the White Sands elevation of 1.193 km, all layers less than layer number 23 are assigned an optical depth of zero. The input τ parameters are then assigned to layer number 23. Above this the optical depth decreases in proportion to the vertical distribution profiles. When IHGT = 1 the percentage differences in radiance are quite small. That is, the radiances differed by less than ±0.1% for the three bands studied. Therefore, as long as this parameter is input into the code, any uncertainty in actual elevation will result in a negligible error.

Non-Lambertian Surfaces

To model the transfer of radiant flux within the atmosphere, the surface bidirectional reflectance factor (BRDF) must be accurately measured. This property must be determined for a number of discrete angular pairs. (The BRDF is the ratio of the radiance reflected in the direction ($\theta';\phi'$) to the total irradiance on the surface from the direction ($\theta;\phi$).) A complete BRDF analysis is both time-consuming and difficult to measure. The equipment required is relatively complex, and it is often difficult to measure the incident irradiance. For these reasons, alternative methods of characterizing the surface reflectance are often sought. These simplifications must not introduce significant errors when used in conjunction with the radiative transfer code.

We chose to characterize the gypsum sand by measuring the reflectance factor. The reflectance factor is the ratio of the flux reflected by a sample surface (the field site) to the flux that would be reflected into the same beam geometry by an identically irradiated Lambertian surface of unity reflectance. The reference panels used at White Sands are of Halon or $BaSO_4$ and have been calibrated in the laboratory to characterize their departure from Lambertian behavior.

Only the $R(\theta_z;0°)$ component of the gypsum sand is measured in the field. For all TM calibrations done to date, we have assumed that this is the only component that needs to be determined accurately. This is based on the premise that the radiance that is directly reflected toward the Landsat sensors will be dominated by the $(\theta_z;0°)$ beam, and that the test site at White Sands is nearly Lambertian. If the surface were truly Lambertian, the reflected portion of the incident irradiance would be distributed uniformly in all directions. Once the reflectance factor is measured for one geometry, it is known for all others. Thus, $R(\theta_z;0°)$ is all that is required. If the surface is not strictly Lambertian, then the error incurred will be dependent on its degree of departure.

Even if the surface were not diffuse, the transfer of radiant flux could be made, using only $R(\theta_z;0°)$, provided there was no multiple scattering within the atmosphere. In reality, radiant flux is scattered out of the solar beam and is incident on the surface in all directions. After reflection, diffuse radiation is scattered into the upward hemisphere. Of the reflected energy that is not initially directed toward the Landsat sensors, some eventually enters the entrance aperture of the TM sensor, but only after it has been scattered by the atmosphere.

In assuming Lambertian surface characteristics and clear atmospheric conditions for White Sands, some uncertainty is introduced into the radiance computed for the TM. To assess this error a study has been made using a modified version of the Herman radiative transfer code. Surfaces that deviated by 5%, 10%, and 20% from Lambertian at a reflected angle of 90° were used for the study. Reflectance values for other angles were computed assuming a linear deviation between $R(\theta_z;0°)$ and $R(\theta_z;90°)$.

Figure 2.5 (page 24) was a plot of the reflectance of gypsum sand, as measured in our laboratory, as a function of angle. For this study sands were collected at several sites throughout the White Sands Missile Range. To simulate a variety of moisture conditions some samples of the sand were moistened and some baked. The data for $\lambda = 0.55$ μm indicate that reflectance increased by about 7% over the 40° range studied. Other groups have measured the Lambertian properties of the gypsum at White Sands, in situ. Eaton and Dirmhirm (1979) report that the anisotropy of reflection seems to be a function of solar zenith angle. For low values no anisotropy was noted. At larger zenith angles they speculate that specular reflection is more predominate. At $\theta_z = 22°$, the sands seemed to deviate by less than 5% from being Lambertian; for $\theta_z > 55°$, the deviation was on the order of 20% for all but the backscatter direction. Here there was a 60% deviation from that measured at R(θ_z;0°).

In Table 6.4 the Herman code output is given for 5%, 10%, and 20% departures from Lambertian behavior. Differences in radiances of 0.7%, 1.4%, and 2.8% were noted at band 1, $\rho = 0.5$. A large uncertainty in the TM calibration can therefore result if the non-Lambertian characteristics of the gypsum are not accounted for. Currently equipment is being built to measure R(θ_z;θ) in the field at other angles of reflection.

Multiple Scattering

It is of interest to determine the importance of using a radiative transfer code that accounts for multiple, not just single, scattering. The Herman code starts by assuming there is no diffuse illumination within the atmosphere. That is, the only source of light is that due to direct solar illumination. At each layer of the atmosphere, a single scatter out of the solar beam occurs. Each of these new scattered rays is traced, and any scattering from them is noted. A single pass is completed when these rays are traced from the top of the atmosphere, reflected from the surface, and returned back up through the atmosphere. For each additional pass another order of multiple scattering is accounted for. Thus, the difference in the final exiting radiance to that which is computed for the first pass is representative of the effects of multiple scattering. For the model reflectance of 0.5, the deviation in radiance between the first and last passes is on the order of −32% for band 1 and −14% for band 5.

Reflectance Factor Uncertainty

The uncertainty in measured reflectance is limited by our ability to calibrate the field reference standards. This uncertainty is 1.5% in the laboratory and approximately 2% in the field. From the July data, the test site uniformity was about 1.5% (the RMS pixel-to-pixel variation in reflectance). We believe that, by use of helicopter photography, extended areas can be characterized to within 2%. Any uncertainty in surface reflectance produces approximately the same uncertainty in computed radiance.

Intermediate Altitude Results

Table 6.6 gives the results of the intermediate altitude studies. The radiative transfer code was used to compute the radiances incident on a sensor at 1.37 km, 1.83 km, 3.05 km, 11.22 km, and 21.22 km. The first three altitudes are used to model what the helicopter-mounted spectropolarimeter would see at 500 ft, 2000 ft, and 6000 ft above the ground. The last two are used to model the effects viewed from a high-altitude aircraft.

In (a) the percentage changes between the radiances above the atmosphere and those computed at the intermediate altitudes are studied. At $\rho = 0.50$, the differences in radiances decreased as the sensor moved up the atmosphere. For example, in band 1 the differences as the sensor ascended were -4.0%, -3.8%, -3.3%, -0.5%, and 0.3%. Band 2 predicted that the radiance differences would increase with increasing altitude. Still, the percentage differences were small ($\lesssim 2\%$).

Table 6.6 Percentage Change in Radiance at Intermediate Altitudes

Change in parameter	Band 1				Band 2				Band 5			
	$\rho=0$	$\rho=0.15$	$\rho=0.50$	$\rho=0.75$	$\rho=0$	$\rho=0.15$	$\rho=0.50$	$\rho=0.75$	$\rho=0$	$\rho=0.15$	$\rho=0.50$	$\rho=0.75$
(a) Change from exoatmospheric radiance at given altitude above sea level (ASL) Ground level is at 1.22 km and IHGT = 23												
1.37 km ASL	-96.01	-27.20	**-3.98**	0.67	-94.50	-14.11	**0.87**	3.47	-91.44	0.72	**2.65**	2.94
1.83 km ASL	-91.48	-25.89	**-3.84**	0.59	-90.79	-13.40	**0.89**	3.37	-79.96	0.50	**2.19**	2.43
3.05 km ASL	-77.53	-21.96	**-3.26**	0.50	-75.43	-10.93	**1.08**	3.16	-58.28	-0.01	**1.22**	1.40
11.22 km ASL	-25.29	-6.70	**-0.48**	0.77	-24.36	-1.92	**2.22**	2.94	-25.11	-0.42	**0.12**	0.19
21.22 km ASL	-5.64	-1.2	0.30	0.60	-4.27	1.09	**2.08**	2.25	-13.35	-0.20	**0.07**	0.10
(b) Change in radiance at a given altitude for a change in input parameter												
1.37 km ASL (4500 ft ASL, or 500 ft above White Sands surface)												
τ_{Ray} 2%	1.72	-0.13	-0.10	-0.04	2.33	-0.07	-0.05	-0.03	0.	0.	0.	0.
τ_{Mie} 10%	-6.90	-0.50	-0.38	-0.31	-4.65	-0.46	-0.42	-0.25	12.5	-0.19	-0.14	-0.09
τ_{oz} 10%	0.	-0.10	-0.11	-0.10	2.33	-0.40	-0.40	-0.40	N/A	N/A	N/A	N/A
τ_{H_2O} 30%	N/A	N/A	N/A	N/A	N/A	N/A	N/A	N/A	0.	-1.19	-1.19	-1.22
1.52-0.0031	3.45	1.47	1.67	1.86	4.65	1.29	1.45	1.59	12.50	0.56	0.63	0.67
Aerosol												
Random	1.72	-0.90	-0.12	0.55	-32.56	-0.76	0.11	0.54	-12.50	-3.29	-3.58	-3.81
Linear	-8.62	-0.20	-0.13	-0.14	-4.65	-0.10	-0.08	-0.08	12.50	0.06	0.07	0.07
Accentuated	-13.79	-0.47	-0.02	0.22	-9.30	-0.92	-0.27	0.15	12.50	-1.54	-1.67	-1.78
Pressure												
Random	129.31	3.80	1.03	-0.01	183.72	3.07	1.01	0.56	-12.50	-0.09	-0.07	-0.06
Linear	39.66	0.77	0.23	0.19	41.86	0.53	0.16	0.13	0.	0.	0.01	0.01
Accentuated	127.59	3.90	1.07	-0.02	183.72	3.07	1.01	0.54	-12.50	-0.13	-0.07	-0.07
Ozone												
Random	0.	0.	0.	0.	0.	0.	0.	0.	N/A	N/A	N/A	N/A
Linear	-1.72	-0.13	-0.18	-0.22	-4.65	-0.40	-0.53	-0.66	N/A	N/A	N/A	N/A
Accentuated	0.	0.	0.01	0.02	2.33	0.03	0.04	0.06	N/A	N/A	N/A	N/A

Table 6.6--Continued

Change in parameter	Band 1				Band 2				Band 5			
	$\rho=0$	$\rho=0.15$	$\rho=0.50$	$\rho=0.75$	$\rho=0$	$\rho=0.15$	$\rho=0.50$	$\rho=0.75$	$\rho=0$	$\rho=0.15$	$\rho=0.50$	$\rho=0.75$
Water vapor												
Random	N/A	N/A	N/A	N/A	N/A	N/A	N/A	N/A	0.	0.	0.02	0.02
Linear	N/A	N/A	N/A	N/A	N/A	N/A	N/A	N/A	0.	-0.06	-0.06	-0.06
Accentuated	N/A	N/A	N/A	N/A	N/A	N/A	N/A	N/A	-12.50	-0.13	-0.10	-0.11
IHGT = 1	370.69	5.50	0.30	-0.48	290.70	2.97	-0.03	-0.48	475.00	-0.22	-1.01	-1.12
1.83 km ASL (6000 ft ASL, or 2000 ft above White Sands surface)												
τ_{Ray} 2%	0.81	-0.10	-0.09	-0.04	1.39	-0.07	-0.04	-0.02	0.	0.	0.	0.
τ_{Mie} 10%	4.03	-0.33	-0.37	-0.34	6.94	-0.33	-0.32	-0.27	10.53	-0.16	-0.15	-0.11
τ_{oz} 10%	0.	-0.10	-0.10	-0.11	0.	-0.39	-0.40	-0.40	N/A	N/A	N/A	N/A
τ_{H_2O} 30%	N/A	N/A	N/A	N/A	N/A	N/A	N/A	N/A	0.	-1.55	-1.57	-1.60
1.52-0.003i	3.23	1.60	1.79	1.97	4.17	1.41	1.54	1.67	10.53	0.66	0.69	0.72
Aerosol												
Random	553.23	18.00	2.88	1.16	938.89	18.01	2.98	1.09	68.42	-6.34	-6.95	-7.21
Linear	8.06	0.13	-0.13	-0.19	16.67	0.13	-0.09	-0.14	31.58	0.13	0.01	0.
Accentuated	349.19	11.29	1.48	0.19	581.94	10.18	1.09	0.08	94.74	-4.24	-4.80	-4.95
Pressure												
Random	202.42	7.33	0.45	-1.19	363.89	7.40	1.22	0.17	-26.32	-0.09	0.01	0.02
Linear	72.58	2.65	0.53	0.24	66.67	1.34	0.28	0.13	5.26	0.03	0.	0.
Accentuated	200.00	7.33	0.46	-1.22	361.11	7.37	1.21	0.15	-26.32	-0.09	0.01	0.02
Ozone												
Random	0.	0.	0.	0.	0.	0.	0.01	0.01	N/A	N/A	N/A	N/A
Linear	0.	-0.13	-0.20	-0.26	1.39	-0.46	-0.64	-0.78	N/A	N/A	N/A	N/A
Accentuated	0.	0.	0.02	0.02	0.	0.03	0.06	0.06	N/A	N/A	N/A	N/A
Water vapor												
Random	N/A	N/A	N/A	N/A	N/A	N/A	N/A	N/A	5.26	0.03	0.02	0.02
Linear	N/A	N/A	N/A	N/A	N/A	N/A	N/A	N/A	5.26	-0.16	-0.16	-0.17
Accentuated	N/A	N/A	N/A	N/A	N/A	N/A	N/A	N/A	5.26	-0.25	-0.27	-0.28

Table 6.6--Continued

Change in parameter	Band 1				Band 2				Band 5			
	ρ=0	ρ=0.15	ρ=0.50	ρ=0.75	ρ=0	ρ=0.15	ρ=0.50	ρ=0.75	ρ=0	ρ=0.15	ρ=0.50	ρ=0.75
IHGT = 1	180.65	5.56	0.37	-0.43	197.22	3.18	0.	-0.47	178.95	-0.13	-0.86	-0.95
3.05 km ASL (10000 ft ASL, or 6000 ft above White Sands surface)												
τ_{Ray} 2%	1.53	-0.03	-0.07	-0.04	1.04	0.	-0.04	-0.01	0.	0.	0.	0.
τ_{Mie} 10%	0.92	-0.28	-0.37	-0.35	1.56	-0.25	-0.33	-0.29	10.26	-0.13	-0.15	-0.12
τ_{oz} 10%	0.	-0.12	-0.10	-0.11	0.	-0.38	-0.41	-0.40	N/A	N/A	N/A	N/A
τ_{H_2O} 30%	N/A	N/A	N/A	N/A	N/A	N/A	N/A	N/A	0.	-1.55	-1.57	-1.60
1.52-0.003i	3.06	1.86	2.00	2.18	3.65	1.66	1.73	1.86	7.69	0.76	0.78	0.82
Aerosol												
Random	131.50	10.35	1.69	0.86	240.63	11.91	2.02	0.84	-5.13	-6.34	-6.68	-6.91
Linear	5.81	0.31	-0.17	-0.27	8.33	0.32	-0.14	-0.21	28.21	0.19	-0.02	-0.04
Accentuated	112.23	9.26	1.46	0.40	207.81	9.71	1.23	0.27	30.77	-3.38	-3.82	-3.96
Pressure												
Random	44.95	4.01	-0.13	-1.40	54.69	3.12	0.55	0.01	12.82	0.09	0.	-0.01
Linear	69.72	6.12	1.15	0.39	58.33	3.12	0.56	0.20	5.13	0.03	0.01	0.
Accentuated	40.06	3.67	-0.02	-1.47	50.00	2.90	0.49	-0.02	10.26	0.09	0.	-0.01
Ozone												
Random	0.	0.	0.	0.	0.	0.03	0.	0.01	N/A	N/A	N/A	N/A
Linear	-0.61	-0.25	-0.31	-0.35	-2.08	-0.83	-1.02	-1.15	N/A	N/A	N/A	N/A
Accentuated	0.	0.	0.02	0.02	0.	0.06	0.07	0.08	N/A	N/A	N/A	N/A
Water vapor												
Random	N/A	N/A	N/A	N/A	N/A	N/A	N/A	N/A	0.	0.	0.02	0.02
Linear	N/A	N/A	N/A	N/A	N/A	N/A	N/A	N/A	0.	-0.22	-0.23	-0.23
Accentuated	N/A	N/A	N/A	N/A	N/A	N/A	N/A	N/A	0.	-0.25	-0.27	-0.28
IHGT = 1	55.35	4.41	0.33	-0.33	57.29	2.55	0.03	-0.36	61.54	0.06	-0.43	-0.49

Percentage change = $100(L_{new} - L_{model})/L_{model}$

Next, in (b), the differences in measured radiance at a given altitude were studied for a change in the model input parameters. For example, consider the highest helicopter altitude of 3.05 km ASL. In band 1, a 2% change in τ_{Ray} corresponded to a -0.1% change in radiance, a 10% change in τ_{Mie} resulted in a -0.4% change in radiance, a 10% change in τ_{oz} yields -0.1% in radiance, and a refractive index of 1.52-0.003i gives a 2.0% change. Results for the other bands are similar, with a 30% change in τ_{H_2O} yielding a -1.2% change in radiance.

To study the effects on variations in the vertical profiles, we made three modifications to each profile. These were the random, linear, and accentuated models defined earlier. In general, changes were less than 2% ($\rho = 0.50$). As there are notable exceptions, particularly in band 5, the vertical distribution model used will indeed affect the accuracy to which the Herman code can predict radiances at helicopter altitudes.

Uncertainty Analysis Summary

Table 6.7 summarizes the uncertainties anticipated for our calibration, assuming average atmospheric conditions for White Sands. The accuracy of this technique seems dependent on the accuracy with which the surface reflectance can be measured, and the validity of the assumptions made on the aerosol parameters. The resulting uncertainties in computed radiance are approximately 4% due to the uncertainty in the imaginary component of refractive index, and 1% to 2% due to uncertainties in the radial size distribution, ground reflectance, the Lambertian assumption, and our uncertainty in published solar irradiance data. Smaller errors result from errors in the optical depth components and air mass computations. An overall root-sum-square (rss) uncertainty of 6% can therefore be expected.

Table 6.7 Summary of Uncertainties in Calibration

Level of uncertainty	
4%	Aerosol imaginary refractive index
1%-2%	Aerosol radial size distribution Ground reflectance Lambertian assumption Exoatmospheric irradiance
<1%	Optical depth components Solar zenith angle
Negligible	Surface elevation

CHAPTER 7

PROGRESS TO DATE AND RECOMMENDATIONS FOR FUTURE WORK

Since the July 8, 1984, calibration an additional set of calibration data has been evaluated, further techniques to increase the accuracy of calibration have been proposed, and plans to collaborate with other groups have been made. These items are discussed below.

Progress

(1) October 28, 1984, calibration. The optical depth components were determined from the same Reagan radiometer ("older" model, SN002) as was used in July. As we now have access to a building on the site, and therefore have electrical power available, the radiometer heater was used. Thus it is felt that the extinction optical depth was determined to sufficient accuracy to obtain a good calibration. Despite this, the calibration values of October 28 differed significantly from those determined in July. The helicopter-mounted Castle spectropolarimeter collected data on October 28, and an extensive analysis was made to compare the radiance predicted at the helicopter altitudes to the radiances measured by this instrument. Agreement was found only for TM band 3. Diffuse-to-direct solar measurements were also made on October 28; this ratio agreed well with that predicted by the Herman code for bands 2 and 3 but not for bands 1 and 4.

(2) The Chuck site has been extended to a 4 X 16 pixel area. This will allow all 16 detectors within each TM band to be individually calibrated.

Future Plans

(1) Helicopter-based calibration. Plans currently call for the Castle spectropolarimeter to be equipped with spectral filters that are matched to the Thematic Mapper. Data collected with this instrument will then be used to verify the Herman code, and also to provide an independent TM calibration. The latter is feasible because the radiance at the helicopter altitude of 3.05 km ASL (6000 feet above the ground at White Sands) differs by only a few percent from that incident at the TM sensor.

(2) Helicopter photography. Plans call for continued use of vertical aerial photography taken from a helicopter. The image of the ground site can be later digitized and used to map reflectance variations over the site.

(3) Secondary test site. A farm area at Maricopa (just south of Phoenix) will be used as a secondary site. The area is a square mile in size, flat, and uniform in reflectance except for five dirt roads.

(4) Diffuse/direct ratio. These data are routinely collected in the field as part of the calibration data set. They will continue to be used to verify the radiative transfer code and its input assumptions. Particular attention will be given to validating the imaginary

component of refractive index used in the radiative transfer calculation, as has been suggested in Herman and Browning (1975).

(5) Inversion technique. Plans call for investigating the use of inversion techniques to help improve the characterization of the aerosol radial size distribution.

(6) Collaboration with the National Oceanic and Atmospheric Administration (NOAA). An independent calibration, made by NOAA personnel from high altitude aircraft, will predict the radiance at the TM. These data will be compared to radiances computed from our ground-based measurements.

(7) SPOT (Système Probatoire d'Observation de la Terre). A contract has recently been received to calibrate this French remote sensing system. Launch is expected in the fall of 1985. Use will be made of this sensor's pointing capabilities, which will allow roughly two calibrations to be made in a week.

REFERENCES

American Ephemeris and Nautical Almanac (published yearly). U.S. Government Printing Office, Washington, D.C.

Ångström, Anders (1929). "On the atmospheric transmission of sun radiation and on dust in the air." Geogr. Ann. (Stockholm) 11, 156-166.

Barker, J. L. (1985). "Relative radiometric calibration of Landsat TM reflective bands." Landsat-4 Science Characterization Early Results, NASA Conference Publication 2355, Vol. III, 1-220.

Barker, J. L., R. B. Abrams, D. L. Ball, and K. C. Leung (1985a). "Radiometric calibration and processing procedure for reflective bands on Landsat-4 protoflight Thematic Mapper." Landsat-4 Science Characterization Early Results, NASA Conference Publication 2355, Vol. II, 47-86.

Barker, J. L., D. L. Ball, K. C. Leung, and J. A. Walker (1985b). "Prelaunch absolute radiometric calibration of the reflective bands on the Landsat-4 protoflight Thematic Mapper." Landsat-4 Science Characterization Early Results, NASA Conference Publication 2355, Vol. II, 277-372.

Barker, J. L., and B. L. Markham (1985). "Spectral characterization of the Landsat Thematic Mapper sensors." Landsat-4 Science Characterization Early Results, NASA Conference Publication 2355, Vol. II, 235-276.

Bemporad, A. (1907). "Versuch einer neuen empirischen Formel zur Darstellung der Anderung der Intensität der Sonnens Strahlung mit der Zenitdistanz." Meteorol. Z. 24, 306-313.

Capron, Barbara (1985). Private communication. Optical Sciences Center, University of Arizona.

Castle, K. R. (1985). The Absolute Radiometric Calibration of a Spectropolarimeter. Ph.D. Dissertation, University of Arizona.

Castle, K. R., R. G. Holm, C. J. Kastner, J. M. Palmer, P. N. Slater, Magdeleine Dinguirard, C. E. Ezra, R. D. Jackson, and R. K. Savage (1984). "In-flight absolute radiometric calibration of the Thematic Mapper." IEEE Trans. Geosci. Remote Sensing GE-22, 251-255.

Chandrasekhar, S. (1950). Radiative Transfer. Oxford University Press, New York. Also Dover Publications, New York (1960), 393 pp.

Curcio, J. S., G. L. Knestrick, and T. H. Cosden (1961). Atmospheric Scattering in the Visible and Infrared. NRL Report 5567, U.S. Naval Research Laboratory, Washington, D.C.

Dave, J. V. (1969). "Scattering of electromagnetic radiation by a large, absorbing sphere." IBM J. Res. Dev., May, 302-313.

Deirmendjian, D. (1963). "Scattering and polarization properties of polydispersed suspensions with partial absorption." In M. Kerker, ed., Electromagnetic Scattering, Macmillan, New York.

Deirmendjian, D. (1969). Electromagnetic Scattering on Spherical Polydispersions. American Elsevier, New York.

Dinguirard, Magdeleine (1983). Private communication through P. N. Slater, Optical Sciences Center, University of Arizona.

Eaton, F. D., and Inge Dirmhirn (1979). "Reflected irradiance indicatrices of natural surfaces and their effect on albedo." Appl. Opt. 18, 994-1008.

Edlen, B. (1953). "The dispersion of standard air." J. Opt. Soc. Am. 43, 339-344.

Elterman, Louis (1966). "Aerosol measurements in the troposphere and stratosphere." Appl. Opt. 5, 1769-1776.

Elterman, Louis (1968). UV, Visible, and IR Attenuation for Altitudes to 50 km. Report AFCRL-68-0153, Air Force Cambridge Research Laboratories, Bedford, Mass., 49 pp.

Elterman, Louis (1970). Vertical-Attenuation Model with Eight Surface Meteorological Ranges 2 to 13 Kilometers. Report AFRCL-70-0200, Air Force Cambridge Research Laboratories, Bedford, Mass., 55 pp.

Engel, J. L., and O. Weinstein (1983). "Thematic mapper—an overview." IEEE Trans. Geosci. Remote Sensing GE-21(3), 258-265.

Freden, S. C., and Frederick Gordon, Jr. (1983). "Landsat satellites." In R. N. Colwell, Manual of Remote Sensing, Ed. 2. American Society of Photogrammetry, Falls Church, Va. (Sheridan Press), 517-570.

Frohlich, C. (1983). "Solar radiometry: total irradiance measurements." Adv. Space Res. 2, 191-198.

Gordon, H. R., J. W. Brown, O. B. Brown, R. H. Evans, and D. K. Clark (1983). "Nimbus 7 CZCS: reduction of its radiometric sensitivity with time." Appl. Opt. 22, 3929-3931.

Grams, G. W., and J. M. Rosen (1978). "Instrumentation for in-situ measurements of the optical properties of stratospheric aerosol particles." Atmos. Tech. Spring(9), 35-54.

Gucker, F. T., and S. Basu (1953). Right-Angle Molecular Light Scattering from Gases. University of Indiana, Bloomington, Ind., Scientific Report No. 1, Contract AF 10(122)-400.

Herman, B. M. (1963). A Numerical Solution to the Equation of Radiative Transfer for Particles in the Mie Region. Ph.D. dissertation, University of Arizona, 130 pp.

Herman, B. M., M. A. Box, J. A. Reagan, and C. M. Evans (1981). "Alternate approach to the analysis of solar photometer data." Appl. Opt. 20, 2925-2928.

Herman, B. M., and S. R. Browning (1965). "A numerical solution to the equation of radiative transfer." J. Atmos. Sci. 22, 59-566.

Herman, B. M., and S. R. Browning (1975). "Determination of the effective imaginary term of the complex refractive index of atmospheric dust by remote sensing: the diffuse-direct radiation method." J. Atmos. Sci. 32, 918-925.

Herman, B. M., S. R. Browning, and R. J. Curran (1971). "The effect of atmospheric aerosols on scattered sunlight." J. Atmos. Sci. 28, 419-428.

Horan, J. J., D. S. Schwartz, and J. D. Love (1974). "Partial performance degradation of a remote sensor in a space environment, and some probable causes." Appl. Opt. 13, 1230-1237.

Hovis, W. A. (1985). "Landsat-4 Thematic Mapper calibration and atmospheric correction." Landsat-4 Science Characterization Early Results, NASA Conference Publication 2355, Vol. III, 411-420.

Hovis, W. A., J. S. Knoll, and G. R. Smith (1985). "Aircraft measurements for calibration of an orbiting spacecraft sensor." Appl. Opt. 24, 407-410.

Iqbal, Muhammad (1983). An Introduction to Solar Radiation. Academic Press, New York.

Jennings, S. G., R. G. Pinnick, and H. J. Auvermann (1978). "Effects of particulate complex refractive index and particle size distribution variations on atmospheric extinction and absorption for visible through middle ir wavelengths." Appl. Opt. 17, 3922-3929.

Junge, C. E. (1963). Air Chemistry and Radioactivity. Academic Press, New York.

Kasten, F. (1964). A New Table and Approximation Formula for the Relative Optical Air Mass. U.S. Army, Cold Regions Research and Engineering, Hanover, New Hampshire, Report 136.

Kastner, C. J. (1985). Herman code outputs used in sensitivity analysis. Available through Dr. Philip Slater, Optical Sciences Center, University of Arizona.

Kastner, C. J., and P. N. Slater (1982). "In-flight radiometric calibration of advanced remote sensing systems." Symposium on Field Measurement and Calibration Using Electro-Optical Equipment: Issues and Requirements, Proc. SPIE 356, 158-165.

Kent, G. S., G. K. Yue, and Adarsh Deepak (1983). "Modeling atmospheric aerosol backscatter at CO_2 laser wavelengths. 1: Aerosol properties, modeling techniques, and associated problems." Appl. Opt. 22, 1655-1665.

Kiang, Richard (1983). Sigma Data Corporation, New York. Private communication with P. N. Slater, Optical Sciences Center, University of Arizona.

Kieffer, H. H., E. M. Eliason, and P. S. Chavez, Jr. (1985). "Intraband radiometric performance of the Landsat-4 Thematic Mapper." Landsat-4 Science Characterization Early Results, NASA Conference Publication 2355, Vol. III, 497-512.

King, M. D., and D. M. Byrne (1976). "A method for inferring total ozone content from the spectral variation of total optical depth obtained with a solar radiometer." J. Atmos. Sci. 33, 2242-2251.

King, M. D., D. M. Byrne, B. M. Herman, and J. A. Reagan (1978). "Aerosol size distributions obtained by inversion of spectral optical depth measurements." J. Atmos. Sci. 35, 2153-2167.

Kneizys, F. X., E. P. Shettle, W. O. Gallery, J. H. Chetwynd, Jr., L. W. Abreu, J. E. A. Selby, R. W. Fenn, and R. A. McClatchey (1980). "Atmospheric transmittance/radiance: computer code LOWTRAN 5." AFGL-TR-80-0067, Feb.

Kneizys, F. X., E. P. Shettle, W. O. Gallery, J. H. Chetwynd, Jr., L. W. Abreu, J. E. A. Selby, S. A. Clough, and R. W. Fenn (1983). Atmospheric Transmittance/Radiance: Computer Code LOWTRAN 6. Report AFGL-TR-83-0187, AFRCL, Bedford, Mass., Aug., 200 pp.

Koepke, Peter (1982). "Vicarious satellite calibration in the solar spectral range by means of calculated radiances and its application to Meteosat." Appl. Opt. 21, 2845-2854.

Landsat Data Users Notes (published quarterly). NOAA Landsat Customer Services, Sioux Falls, South Dakota.

Langley, S. P. (1881). "The bolometer and radiant energy." Proc. Am. Acad. Arts Sci. 16, 342-358.

Lansing, J. C., Jr., and R. W. Cline (1975). "The four- and five-band multispectral scanners for Landsat." Opt. Eng. 14, 312.

Lindberg, J. D., and J. B. Gillespie (1977). "Relationship between particle size and imaginary refractive index in atmospheric dust." Appl. Opt. 16, 2628-2630.

Liou, Kuo-Nan (1980). An Introduction to Atmospheric Radiation. Academic Press, New York, 392 pp.

London, J. (1962). "The distribution of total ozone over the northern hemisphere." Sun Work 7, 11-12.

Mateer, C. L., J. J. DeLuisi, and Carolyn C. Porco (1980). The Short Umkehr Method, Part I: Standard Ozone Profiles for Use in the Estimation of Ozone Profiles by the Inversion of Short Umkehr Observations. NOAA Technical Memorandum ERL ARL-86, July.

McCartney, E. J. (1976). Optics of the Atmosphere. John Wiley & Sons, New York, 408 pp.

McClatchey, R. A., R. W. Fenn, J. E. A. Selby, F. E. Volz, and J. S. Garing (1972). "Optical Properties of the Atmosphere (Third Edition)." Report AFCRL-72-0497, Environmental Reasearch Papers No. 411, Air Force Cambridge Research Laboratories, Bedford, Mass. Also in W. G. Driscoll, ed., Handbook of Optics, McGraw-Hill, New York, Ch. 14.

Mie, G. (1908). "A contribution to the optics of turbid media, especially colloidal metallic suspensions." Ann. Phys. 25(4), 377-445. In German.

Minzner, R. A., K. S. Champion, and H. L. Pond (1959). The ARDC Model Atmosphere, 1959. Air Force Cambridge Research Center, Air Force Surveys in Geophysics, No. 115.

Neckel, Heinz, and Dietrich Labs (1981). "Improved data of solar spectral irradiance from 0.33 to 1.25 μm." Sol. Phys. 74, 231.

Neckel, Heinz, and Dietrich Labs (1984). "The solar radiation between 3300 and 12500 A." Sol. Phys. 90, 205-258.

Nianzeng, Che (1984). Private communication through Dr. P. N. Slater, Optical Sciences Center, University of Arizona.

Norwood, V. T., L. R. Fermelia, and G. A. Tadler (1972). Multispectral Scanner System for ERTS, Hughes Aircraft Co. Final report for NASA contract NAS 5-11255.

Norwood, V. T., and J. C. Lansing, Jr. (1983). "Electro-optical imaging sensors." In R. N. Colwell, Manual of Remote Sensing, Ed. 2, American Society of Photogrammetry, Falls Church, Va., Ch. 8.

Palmer, J. M. (1982). "The effects of errors in the geometrical determination of optical air mass on the accuracy of extraterrestrial solar spectral irradiance as obtained using the Langley method." Private communication, Optical Sciences Center, University of Arizona.

Palmer, J. M. (1984). "Effective bandwidths for LANDSAT-4 and LANDSAT-D' multispectral scanner and Thematic Mapper subsystems." IEEE Trans. Geosci. Remote Sensing GE-22(3), 336-338.

Palmer, J. M., and M. G. Tomasko (1980). "Broadband radiometry with spectrally selective detectors." Opt. Lett. 5, 208-210.

Penndorf, R. (1954). The Vertical Distribution of Mie Particles in the Troposphere. Report AFCRC-54-5, Air Force Cambridge Research Laboratories, Bedford, Mass.

Reagan, J. A. (1983). Private communication. Department of Electrical Engineering, University of Arizona.

Reagan, J. A., I. C. Scott-Fleming, B. M. Herman, and R. M. Schotland (1984). Proc. of IGARSS '84 Symposium, Strasbourg, 27-30 August.

Rozenberg, G. V. (1966). Twilight: A Study in Atmospheric Optics. Plenum Press, New York. (Translated from Russian.)

Russell, P. B., T. J. Swissler, M. P. McCormick, W. P. Chu, J. M. Livingston, and T. J. Pepin (1981). "Satellite and correlative measurements of the stratospheric aerosol. I: An optical model for data conversions." J. Atmos. Sci. 38, 1279-1294.

Sekera, Z. (1955). Scattering Matrix for Spherical Particles and Its Transformation in Investigation of Skylight Polarization, Appendix D. Final Report, Contract AF 19(122)-239, Dept. of Meteorology, University of California, Los Angeles, 68 pp.

Shaw, G. E. (1976). "Error analysis of multi-wavelength sun photometry." Pageoph. 114, 1-14.

Shaw, G. E., J. A. Reagan, and B. M. Herman (1973). "Investigations of atmospheric extinction using direct solar radiation measurements made with a multiple wavelength radiometer." J. Appl. Meteorol. 12, 374-380.

Sissenwine, N., D. D. Grantham, and H. A. Salmela (1968). Humidity Up to the Mesopause. Report AFRCL-68-0550, Air Force Surveys in Geophysics No. 206. Air Force Cambridge Research Laboratories, Bedford, Mass.

Slater, P. N. (1979). "A re-examination of the Landsat MSS." Photogramm. Eng. Remote Sensing 45, 1479-1485.

Slater, P. N. (1980). Remote Sensing Optics and Optical Systems. Addison-Wesley, Reading, Massachusetts. 575 pp.

Slater, P. N. (1985). "The importance and attainment of accurate absolute radiometric calibration." Proc. SPIE 475, 34-40.

Slater, P. N., and R. D. Jackson (1982). "Atmospheric effects on radiation reflected from soil and vegetation as measured by orbital sensors using various scanning directions." Appl. Opt. 21, 3923-3931.

Slater, P. N., J. M. Palmer, P. A. Franken, and A. R. Kassander, Jr. (1982). Proposal for Spectroradiometric Calibration of the Thematic Mapper and Multispectral Scanner System. Optical Sciences Center, University of Arizona, January 14.

Spencer, J. W. (1971). "Fourier series representation of the position of the sun." Search 2(5), 172.

Stratton, J. A. (1941). Electromagnetic Theory. McGraw-Hill, New York.

Thekaekara, M. P., R. Kruger, and C. H. Duncan (1969). "Solar measurements from a research aircraft." Appl. Opt. 8, 1713-1732.

United States Geological Survey (1979). Landsat Data Users Handbook, revised ed., United States Department of the Interior.

USSA (1962). U.S. Standard Atmosphere, 1962. Cat. No. NAS 1.2:At6/962. GPO, Washington, D.C.

USSAS (1966). U.S. Standard Atmosphere Supplements, 1966. Cat. No. NAS 1.2:At6/966/supp. GPO, Washington, D.C.

Valley, S. L., ed. (1965). Handbook of Geophysics and Space Environments. McGraw-Hill, New York.

van de Hulst, H. C. (1957). Light Scattering by Small Particles. John Wiley & Sons, New York, 470 pp.

Vigroux, E. (1953). "Contributions a l'etude experimentale de l'absorption de l'ozone." Ann. Phys. (Paris) 8, 709.

Winker, D. (1980). Private communication. Optical Sciences Center, University of Arizona.

Young, A. T. (1974). "Observational technique and data reduction." Ch. 3 (pp. 123-179) in Nathaniel Carelton, ed., Astrophysics, vol. 12 of Methods of Experimental Physics. Academic Press, New York.

Yue, G. K., and Adarsh Deepak (1983). "Retrieval of stratospheric aerosol size distribution from atmospheric extinction of solar radiation at two wavelengths." Appl. Opt. 22, 1639-1645.